INTRODUCING ORGANIC MOLECULAR CRYSTALS INTO ULTRAFAST ELECTRON DIFFRACTION

ANDREA BERENIKE ROHWER (née VON FLOTOW)

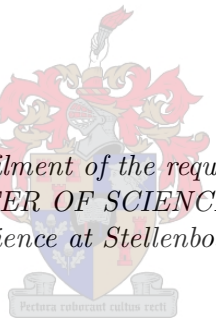

Thesis presented in partial fulfilment of the requirements for the degree of
MASTER OF SCIENCE
in the Faculty of Science at Stellenbosch University.

Supervisor : Professor H. P. H. Schwoerer

Co-supervisor : Professor E. G. Rohwer

December 2014

DECLARATION

By submitting this thesis electronically, I declare that the entirety of the work contained therein is my own, original work, that I am the sole author thereof (save to the extent explicitly otherwise stated), that reproduction and publication thereof by Stellenbosch University will not infringe any third party rights and that I have not previously in its entirety or in part submitted it for obtaining any qualification.

December 2014

Abstract

Organic molecular salts have a wide range of physical properties which can be chemically tailored by minor variations of their substituents. These characteristics include high degrees of anisotropy, electrical conductivity ranging from superconducting to insulating, and structural changes in the crystal lattice during first order phase transitions brought about by minimal changes in temperature, effective pressure, and in some cases even light. Hence, these materials are particularly interesting for the development of molecular electronics and also as study materials in solid state physics. The family of copper-dimethyl-dicyanoquinone-diimine ($Cu(DMe\text{-}DCNQI)_2$) salts forms part of the radical anion salt subclass of organic molecular crystals and is of particular interest due to its extraordinarily high conductivity compared to other quasi one-dimensional organic conductors. Its metal-to-insulator phase transition is characterised by conductivity jumps across several orders of magnitude within a few kelvin. Over the past three decades the metallic and insulating phases, as well as the transition behaviour have been investigated extensively utilising a broad spectrum of methods amongst others electrical conductivity, electron spin resonance, and reflectivity measurements, x-ray photoelectron and infrared spectroscopy, x-ray diffraction, and dilatometry. Fast light-switching between phases has been observed in partially deuterated forms of $Cu(DCNQI)_2$ on sub-100-ps time scales. Furthermore, the phase transition is believed to be induced by a deformation of the crystalline lattice and a charge density wave formation which are detectable in diffraction images. Therefore we want to investigate this metal-to-insulator phase transition structurally and temporally via ultrafast electron diffraction. The technique of ultrafast electron diffraction employs the fundamentals of pump-probe spectroscopy: One of the two femtosecond pulsed laser beams excites the thin, crystalline sample, while the other – after being converted into a pulsed electron beam via the photoelectric effect – forms a diffraction image of the sample's lattice structure. The arrival time of the two pulses at the sample can be varied by a few femtoseconds with respect to each other enabling the resolution of ultrafast structural dynamics of the crystal's atomic lattice via electron diffraction. During the work presented in this thesis the sample preparation and characterisation leading to a successful introduction of $Cu(DCNQI)_2$ into our ultrafast electron diffraction setup is presented. A diffraction pattern of comparable quality to that of a commercially available transmission electron microscope was recorded of the metallic state of partially deuterated d_6 $Cu(DCNQI)_2$. Subsequent analysis of the obtained diffraction data and further studies of the low

temperature state – including simulations as well as experiments – have narrowed down the factors still making the detection of the insulating phase's charge density wave signature diffraction pattern evasive. Possible solutions to experimental challenges are proposed to make the documentation of structural ultrafast dynamics in these organic molecular salts an attainable goal in the future.

Opsomming

Organiese molekulêre soute het ‘n wye verskeidenheid van fisiese eienskappe wat chemies verander kan word deur geringe variasie in die samestelling van die sout. Hierdie eienskappe sluit in ‘n hoë graad van anisotropie, elektriese geleidingsvermoë wat strek van supergeleiding tot elektriese isolasie, en strukturele veranderinge in die kristalstruktuur tydens eerste orde fase-oorgange wat veroorsaak word deur geringe veranderinge in temperature, effektiewe druk en in sommige gevalle selfs lig. Gevolglik is hierdie material besonder interessant vir die ontwikkeling van molekulêre elektronika en ook as studiemateriaal in vastetoestandfisika. Die familie van koperdimetieldisianokinoondiimien ($Cu(DMe\text{-}DCNQI)_2$) soute vorm ‘n deel van die radikaal-anioon-sout subklas van organiese molekulêre kristalle en is van besondere belang as gevolg van hulle buitengewone hoë elektriese geleidingsvermoë in vergelyking met ander kwasi-eendimensionele organiese geleiers. Die metaal-na-isolator fase-oorgang van hierdie kristal word gekenmerk deur die verandering van die geleidingsvermoë met verskeie ordegroottes binne ‘n paar kelvin. Gedurende die laaste drie dekades is die metaal en isolator fases, asook die oorgangsgedrag deeglik ondersoek met behulp van ‘n wye verskeidenheid van metodes wat onder andere elektriese geleidingsvermoë, elektron-spin resonans en refleksiemetings, x-straal fotoelektron en infrarooi spektroskopie, x-straal diffraksie en dilatometrie insluit. Vinnige skakeling tussen fases is waargeneem in gedeeltelik gedeuteerde vorms van $Cu(DCNQI)_2$ op ‘n sub-100-ps tydskaal. Daar word verder geglo dat die fase-oorgang geïnduseer word deur ‘n deformasie van die kristalstruktuur en die vorming van ‘n ladingsdigtheidgolf wat meetbaar is in elektrondiffraksiebeelde. Om hierdie rede wil ons die metaal-na-isolator fase-oorgang se struktuur- en tydafhanklikheid ondersoek deur gebruik te maak van ultra-vinnige elektron diffraksie. Die tegniek van ultra-vinnige elektron diffraksie maak gebruik van die beginsels van pomp-toets spektroskopie: Een van die twee femtosekonde laserpulse wek die dun kristallyne monster op, terwyl die ander na omskakeling in ‘n elektronpuls via die foto-elektriese effek ‘n diffraksiebeeld van die monster se kristalstruktuur vorm. Die aankomtyd van die twee pulse by die monster kan met ‘n paar femtosekondes ten opsigte van mekaar verander word om die tydresolusie van die ultra-vinnige strukturele dinamika van die kristal se atoomstruktuur deur elektrondiffraksie moontlik te maak. In hierdie tesis word die monstervoorbereiding en karakterisering wat gelei het tot suksesvolle eksperimente op $Cu(DCNQI)_2$ in ons ultra-vinnige elektron diffraksie opstelling behandel. ‘n Diffraksie patroon waarvan die kwaliteit vergelykbaar is met die van ‘n kommersiëel beskikbare transmissie

elektron mikroskoop is gemeet vir die metaalfase van gedeeltelik gedeuteerde d_6 Cu(DCNQI)$_2$. Daaropvolgende analiese van die gemete diffraksiedata en verdere studies van die lae temperatuur toestand wat simulasies sowel as eksperimente insluit het 'n klein aantal faktore uitgewys wat steeds die deteksie van die isolatorfase se ladingsdigtheidgolf se kenmerkende diffraksiepatroon verhoed. Moontlike oplossings tot eksperimentele uitdagings word voorgestel om die dokumentering van strukturele ultra-vinnige dinamika in hierdie organiese molekulêre soute 'n haalbare toekomstige doelwit te maak.

Acknowledgements

For the great privilege and inspirational learning experience of working under the supervision and guidance of Prof. Heinrich Schwoerer I am immensely grateful. The interest and support of my co-supervisor Prof. Erich Rohwer were also invaluable. The senior UED members, Kerstin Haupt and Nicolas Erasmus, patiently guided my learning and getting acquainted with their experimental setup and helped me with my work. Olufemi Olaoye did all the simulations presented in this thesis and was always willing to explain and discuss theoretical aspects of my project with me. Aminad Suleiman and Bart Smit who joined the team later helped with many measurements and it was fun to work with them. Molecular crystals were synthesised and partly characterised by Florian Hüwe at the University of Würzburg in Germany. During his visit at the LRI, further sample preparation and characterisation were done in our team. His resourcefulness in the laboratory and in finding relevant literature were remarkable. The scientific creativity and curiosity of all my colleagues was tremendously motivating. Mohamed Jaffer at the TEM unit and ultramicrotome at the UCT taught and assisted us in sample preparation and characterisation. Lize Engelbrecht was always willing to help with ultramicrotoming at the CAF at SU. To the team of technical staff at the physics department I would like to express my gratitude and recognition. They were always approachable and their creative way of helping us with anything from maintaining our high voltage source to building a delicately small sample stage amazed me repeatedly. A warm thanks also goes to the administrative staff of the physics department, who were always friendly and made things run smoothly. The entire physics department has been an academic home to me. I have great respect for the lecturers who have guided me through my undergraduate and post-graduate studies and I am truly grateful for all their time and effort. Getting to know many of the post-graduates better through our joint interest in the outreach projects has been a wonderful privilege.

My Masters studies were partly funded by the NRF through the SARChI grant of my supervisor. The Wilhelm Frank Trust also supported me generously during this project – even for an extended time during which more results could be obtained. I am extremely grateful for the trust and support of these agencies without which my Masters studies would not have been possible.

Finally, I would like to thank all the people outside my academic environment who supported, sustained, and encouraged my growing and learning experiences - my family and friends. Especially to my husband, for the loving and persistent backing – thank you!

CONTENTS

LIST OF FIGURES

LIST OF TABLES

CHAPTER 1
INTRODUCTION

Organic molecular solids have properties that make them particularly interesting as study materials for solid state physicists. These materials have also become increasingly important in the development of molecular electronics, where molecules are utilised in data-storage and so-called logic elements. Particularly the variability of the physical properties of organic solids – achievable by minor chemical changes – makes them attractive to researchers and developers.

What then are the chemical properties underlying these physical characteristics of organic molecular crystals?

- Organic solids are made up of molecules or ions which are mainly constituted of carbon and hydrogen atoms, but often also contain nitrogen, oxygen, sulphur, and selenium atoms. In molecular crystals the molecules making up the solid remain in tact. Therefore the properties of the crystal are directly determined by the constituent molecules. The strong covalent intramolecular forces acting between the atoms of the molecules are much stronger than the intermolecular van der Waals and ionic bonds holding the molecules together to form the crystal. The characteristic conjugated π electron system in the structure of organic molecular solids governs these interactions. Due to the short range of these interactions, it is relatively easy to produce high quality surfaces and interfaces with these materials.

- Due to the delocalised nature of the π electrons, the electronic excitation energies are in the regime of a few electron Volts. For this reason organic solids generally absorb or luminesce in the near infrared, visible, or near ultraviolet region of the electromagnetic spectrum. This property allows switching between phases, e.g. from metallic to insulating, using light pulses in this spectral range.

- In polar organic salts, such as organic radical ion crystals or charge transfer crystals which form a sub class of the organic molecular materials, the π electron systems are ionised. In these materials the molecules are held together by ionic bonds in addition to the van der Waals forces. The crystalline structure of such solids is thus often determined by the ionic interactions between the constituent molecules.

- In molecular crystals which are electronically conducting, such as $Cu(DCNQI)_2$, metallic bonding contributes additionally to the cohesion inside the crystal.

Due to this wide range of intermolecular interactions that are responsible for the cohesion between the molecules making up the organic solid, these materials exhibit a broad spectrum of physical characteristics. In particular, the electronic and magnetic properties of these materials vary dramatically:

- Their ability to transport charge ranges from superconducting all the way to insulating.
- Strong electron-electron and/or electron-phonon coupling seems to occur in some systems resulting in Mott and/or Peierls instabilities, respectively [9, 13, 16–27]. These correlations result in metal-insulator phase transitions with jumps in conductivity over several orders of magnitude, although the external or "internal" (chemical) changes to the crystal are minimal, e.g. in DCNQI salts.
- High anisotropy with respect to conductivity has been observed, e.g. highly one-dimensional conductivity along the molecular stacking axis exhibited by radical ion salts.
- Excitonic states can be observed in organic molecular salts.

Molecular solids are therefore good materials to study numerous solid state science phenomena including weak intermolecular forces, various electrical, magnetic, and optical effects, anisotropicity exhibited by these properties, as well as phase transitions of different orders.

In the scope of this project we focused on the class of radical ion salts. Most of the experiments were conducted on crystals of the quasi one-dimensional, highly conductive organic radical anion salts containing dicyanoquinone-diimine (DCNQI), specifically with copper as counterion, forming $Cu(DCNQI)_2$. They belong to the material class where van der Waals, ionic, and metallic bonding play a role in the intermolecular cohesion.

Crystals of this particular material have been studied since the late 1980's [28] employing various methods in order to investigate different properties: Changes in conductivity, magnetic susceptibility, and crystalline structure across the metal-insulator transition have been considered. This phase transition was brought about by varying numerous external and "internal" (chemical) factors, namely: temperature, pressure, stress, illumination (light), degree of deuteration and different

alloys of these, doping with different metal ions including Cu, Li, Ag, as well as different substituent groups on the DCNQI ion. The effect of these parameters on the electrical conductivity was measured. Dilatometry [9] was used to measure macroscopic structural changes of the bulk crystal. In addition, changes in the crystalline structure have been investigated by x-ray diffraction [2, 4, 6, 13, 15, 17–19, 22, 28–31], x-ray photoelectron spectroscopy (XPS) [4, 13, 28–30, 32, 33], and electron spin resonance (ESR) [2, 4, 6, 7, 13, 20, 30, 34–40], amongst other methods.

Sudden dramatic changes in the conductivity along the crystal axis – by eight orders of magnitude over a temperature range of a few kelvin – have been observed in this material during phase transition. Structural changes, e.g. observed via x-ray diffraction, have been associated with these electronic transitions. The crystal lattice undergoes a trimerisation in the same direction as the drop in conductivity upon cooling. It has been demonstrated that changes in conductivity can be optically induced on a very short time scale and are short-lived under certain conditions. While these experiments focused on studying the phase transitions via conductivity measurements, our aim is to investigate the structural changes employing ultrafast electron diffraction (UED).

This project was aimed at gaining an understanding of the sample – $Cu(DCNQI)_2$ – and introducing it into our ultrafast electron diffraction system. Sample preparation and experimental techniques of the existing setup were advanced. Initial characterisation was done with conventional methods in order to compare the outcome to known results. First electron diffraction images were successfully recorded in the UED setup. These initial steps towards time resolved ultrafast electron diffraction experiments on this organic molecular salt are presented in the chapters that follow.

In this thesis the sample's chemical and physical properties are first introduced. Thereafter the basic theory underlying the electron diffraction process and its results are outlined. The ultrafast electron diffraction experiment and its relevance in the study of the structural changes fundamental to its phase transition behaviour are discussed. Subsequently sample synthesis and preparation techniques in order to meet the UED requirements are explained. Thereafter follows an outline of the initial characterisation via conductivity, absorption spectroscopy, and transmission electron microscopy measurements. Finally, results, discussion, and analysis of initial electron diffraction experiments performed in our setup are presented. The thesis concludes with possible improvements to overcome current experimental challenges, as well as suggestions for related future experiments.

CHAPTER 2
BACKGROUND OF SAMPLE AND EXPERIMENT

2.1 Sample: chemical and physical properties

The radical salts of dicyanoquinonediimine, M(R_1,R_2-DCNQI)$_2$, with various side-group substituents (e.g. R_1, R_2 = Me, MeO, Cl, Br, I, see, for instance, [2, 28, 37]) and counterions (e.g. M = Cu, Li, Ag, Ba, see, for instance, [1, 2, 7, 22, 40]) have been investigated for almost three decades. The general structure of the organic DCNQI molecule is shown in Figure 2.1(a) - a six-membered aromatic carbon ring, with two cyano groups, two hydrogen atoms, and two other side groups (R_1 and R_2) attached. The delocalised π electrons in this organic molecule (above and below the six-membered carbon ring) play an important role in the chemical and physical properties of its salts.

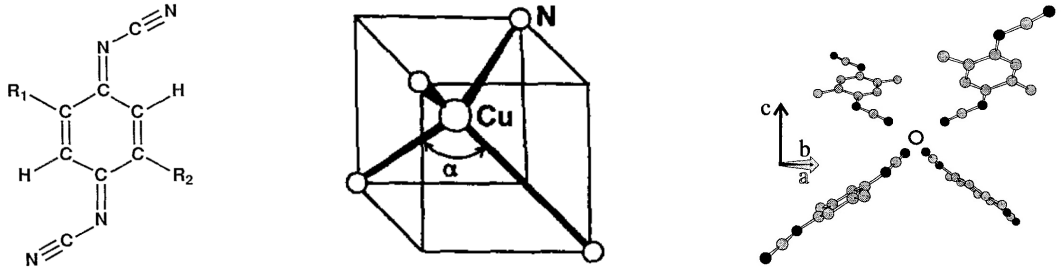

(a) **(b)** **(c)**

Figure 2.1: **(a)** Molecular structure of an (R_1,R_2-DCNQI) molecule [1]. **(b)** Tetrahedral coordination around a copper ion in Cu(DCNQI)$_2$ [2]. **(c)** The tetrahedral coordination around the central metal ion (open circle) with the full DCNQI molecules sketched. Black filled circles represent nitrogen atoms, and grey filled circles are carbon atoms [3].

Generally a central metal ion (M) is tetrahedrally coordinated to four DCNQI molecules surrounding it. The Cu ion is in the centre of the tetrahedron, with four corners occupied by the DCNQI's cyano-group nitrogen atoms (making this a body centred crystal structure). This structure is depicted in Figure 2.1(b) with (M = Cu). The coordination angle α is indicated between N-Cu-N coordination lines and is an indicator for the degree of distortion of the tetrahedron away from the ideal 109.6°. In Table 2.1 typical values of α for some Cu(DCNQI)$_2$ salts at 300 K and 20 K are summarised from [15]. Figure 2.1(c) shows the tetrahedral coordination with the full DCNQI molecules surrounding the central metal ion. In this schematic the crystallographic c-axis lies vertical in the plane of the page. The a-axis points at a 45° angle out of the page, and the b-axis at the same angle into the page [3].

The $Cu(DCNQI)_2$ salts, i.e. $Cu(R_1,R_2\text{-}DCNQI)_2$, are isostructural with a body-centred tetragonal space group $I4_1/a$ at room temperature [28]. In the salt the DCNQI molecules and copper ions form separate segragated stacks thus forming quasi one-dimensional (needle-like) crystals [7] (see Figure 2.3). The stacking axis is named the crystallographic c-axis. A view along the c-axis is shown in Figure 2.2. The tetragonal coordination linking the DCNQI molecules to the central copper ions is an important feature influencing the electronic characteristics of this system and are discussed in more detail later in this section.

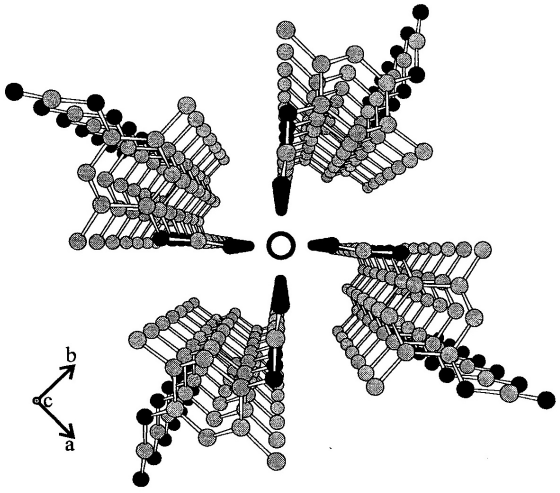

Figure 2.2: View along the c-axis of the $Cu(DCNQI)_2$ salt. Black filled circles represent nitrogen atoms, grey filled circles are carbon atoms, and the central open circle is the copper ion forming the "bridge" between the DCNQI molecules. Hydrogen atoms have been omitted in this diagran as well as double bonds. The side groups R_1, R_2 are methyl here. The crystalligraphic c-axis is perpendicular to the plane of the page, while the a- and b-axes lie orthogonal to each other in the plane of the page [3].

Macroscopically the crystals formed between these organic molecules and their counterions appear needle-like. The needles are a few centimetres long and tens of micrometers thick. Freshly grown crystals appear black and shiny (indicating their metallic state at room temperature). Their basal face is square, which matches the crystal structure depicted in the c-axis projection in Figure 2.2 [13]. (Figure 2.3 shows photographs of the dimensions and appearance of $Cu(DCNQI)_2$ crystals.)

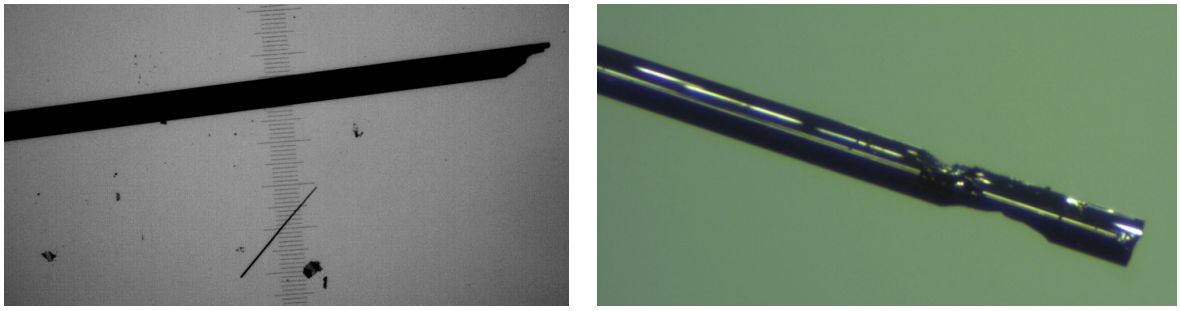

(a) **(b)**

Figure 2.3: **(a)** An image of a $Cu(DCNQI)_2$ needle under a light microscope. The smallest divisions indicated on the microscope slide are 0.01 mm apart. This particular needle was about 70 μm thick. In this image the sample was illuminated from the bottom only. **(b)** A top illuminated needle of $Cu(DCNQI)_2$. The black needle's shiny and faceted surface is clearly visible.

The copper salts of DCNQI are of special interest due to their extraordinary electrical conductivity properties. Extremely high conductivities have been reported $\sim 10^3$ S cm^{-1} at room temperature and ambient pressure [28].

Via electrical resistivity measurements, e.g. [28], the copper salts have been observed to be either in a metallic conducting state or in an insulating state. What follows is a summary of the internal molecular properties and electronic structure underlying these two physical states.

Metal conduction occurs due to electrons that are situated in partially filled energy bands [41]. In the conducting state of $Cu(DCNQI)_2$ the DCNQI molecules are uniformly arranged in a one-dimensional column. The overlap of DCNQI molecules within the stack is of the "double bond over ring" type forming a band of delocalised π electrons generally found in radical anion salts [4]. The columns of the organic molecules are interconnected by the tetrahedral coordination with the Cu ions (see Figure 2.1(**a**), (**b**)). This coordination has a distorted tetrahedral character with D_{2d} symmetry [8]. The coordination angle α indicates the degree of distortion away from ideal tetrahedral T_d symmetry for which $\alpha_{T_d} = 109.6°$ [4] (see Table 2.1 for values relevant to our sample). This distorted tetrahedral coordination around the Cu ions causes splitting of the $3d$ copper orbital into a higher lying d_{xy} orbital and two lower d_{yz} and d_{zx} orbitals. This is depicted in Figure 2.4 [4]. The lifted d_{xy} Cu orbital is located near the Fermi level of the one-dimensional $p\pi$ band of the DCNQI stacks and therefore a hybridisation takes place. In the metallic state of the system this $p\pi$ band

of the DCNQI molecular orbital is one third filled, i.e. the Fermi energy level, E_F, is at one third of the maximum energy of the band. Copper ions are found in a mixed valence state of $Cu^{+4/3}$ [28]. Due to the extended orbital overlap between the DCNQI stacks bridged by the copper ions, this $p\pi - d$ mixing of the molecular orbitals causes the usual quasi one-dimensional conductivity along the DCNQI columns to become quasi three dimensional [4, 32] resulting in the extraordinary conductivity of $Cu(DCNQI)_2$. When the splitting of the $3d$ copper orbital is only small, i.e. α is minimally distorted (see room temperature values of α in Table 2.1), all three d_{xy}, d_{yz}, and d_{zx} orbitals contribute to the $p\pi - d$ interaction. The system then displays multi-Fermi surface character and stays metallic to lowest temperatures [15], e.g. h_8 $Cu(DCNQI)_2$. The DCNQI molecules are evenly spaced along c-axis in the metallic state. This state is schematically summarized in Figure 2.5 using the example of a conductor with a half filled band and a horizontal lattice spacing a.

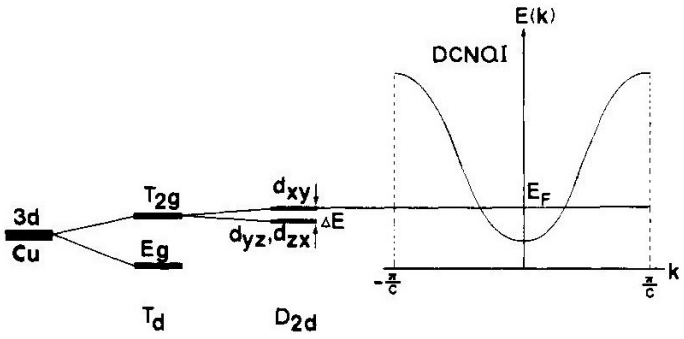

Figure 2.4: Hybridisation of the $3d$ copper orbitals and the $p\pi$ band of DCNQI [4].

Insulators, on the other hand, are characterised by all their energy bands being either completely filled or completely empty. In this state no electrons can move in an electric field. There is also a significant energy gap between the top of the highest filled band (valence band) and the bottom of lowest empty band (conducting band) [41]. The energy level of the highest filled band is called the Fermi energy, E_F. How and why then, does the $Cu(DCNQI)_2$ system change from a metallic to an insulating phase at low temperatures, i.e. $T < T_{MI}$? When the splitting of the $3d$ copper orbital depicted in Figure 2.4 is large, i.e. the d_{xy} orbital lies substantially higher than the d_{yz} and d_{zx} orbitals – which occurs when the tetragonal distortion is large (see low temperature values for α in Table 2.1), leading to the characteristic contraction along the c-axis (see Figure 2.6) – the $p\pi - d$ interaction occurs mainly between the d_{xy} orbital and DCNQI $p\pi$ band. In this case two pairs of Fermi surfaces occur which can be nested into each other and an energy gap is created across the

entire Fermi surface [15]. This energy gap forms at the Fermi level and is situated at the related Fermi wave vectors in momentum space $k = \pm k_F$ (see Figure 2.5 [3]). This gap formation at the Fermi level causes a transition into the insulating phase – with completely filled energy bands below the Fermi level and completely empty bands above. This scenario is depicted in Figure 2.5 [3] for a metal with a half filled conducting band (see figure caption for further detail). Due to the formation of the band gap during the metal to insulator phase transition at low temperatures the energies of the occupied states below E_F are lowered, reducing the total electronic energy of the system, thus making this state favourable at low temperatures, where electrons cannot be thermally excited across the energy gap [24]. In quasi one-dimensional systems at low temperature this gap formation is realised by a modulation of the conduction electron density of the metal and a modulation of the underlying lattice atom positions – also known as CDW formation. This is shown in the bottom left quadrant of Figure 2.5: the atomic positions have shifted to form a superstructure with a $2a$ periodicity. This is possible because the elastic energy cost to modulate atomic positions is smaller than the gain in conduction electron energy [24]. (At high temperatures the electronic energy gain is smaller, because thermal excitation of electrons across the band gap stabilises the metallic state [24].) The insulating phase of $Cu(DCNQI)_2$ salts has a three-fold superstructure along the c-axis, with a periodicity of $3c$. Additionally to the CDW formation along the DCNQI column, a charge ordering in the copper ion stacks occurs, forming (...,Cu^+, Cu^+, Cu^{+2},...). The three-fold CDW superstructure along the DCNQI columns and the charge ordering of the copper stacks coincide. [18]. The space group crystal lattice in the insulating phase was also found to not be body centred anymore, but rather $P\bar{4}$. In summary the insulating phase of the $Cu(DCNQI)_2$ salts is characterised by a CDW formation along the DCNQI stacks which opens a band gap at the Fermi surface thus lowering the electronic energy of the system. This mechanism is enabled by the distortion of the coordination tetrahedron around the Cu ions and is additionally paired with a charge ordering of the copper ions.

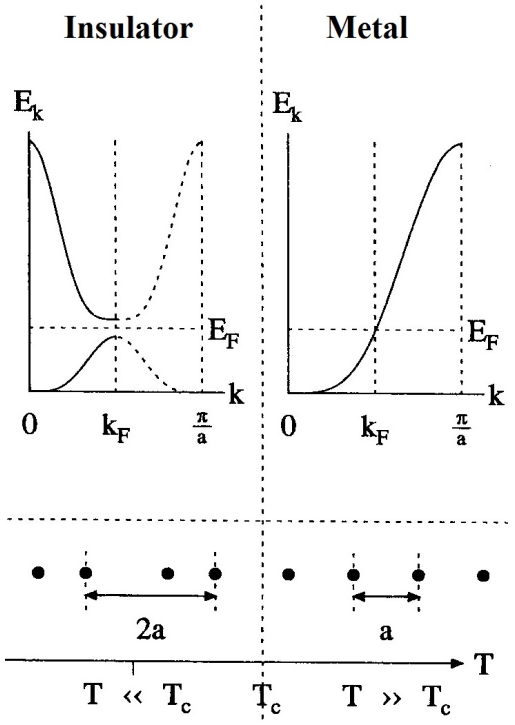

Figure 2.5: Band gap and charge density formation explained using the example of a quasi one-dimensional conductor with a half-filled conduction band. In the top half the electron energy, E_k, is plotted as a function of the electron wave vector k in momentum space for the metallic phase (right) and the insulting phase (left). The associated atomic lattice spacing of each phase is displayed in the two quadrants below the graphs. (Figure adapted from [3].)

The metal-insulator phase transition of $Cu(DCNQI)_2$ was, amongst other parameters, investigated as a function of temperature. Interferometric measurements determining the temperature dependence of the length of a d_6 $Cu(DCNQI)_2$ crystal during cooling and heating, performed by Schmitt *et al.* [5] are shown in Figure 2.6 in comparison to resistivity measurements in the same temperature range. In contrast to the resistivity phase transition behaviour, the crystal length changes more gradually (the needle contracts/expands by about 0.08 % over almost 10 K, while the conductivity jumps over six orders of magnitude within 1 K. Similar results were obtained by Karutz *et al.* [9] during dilatometry experiments determining the crystal's length and conductivity measurements. The difference in the macroscopic conductivity (abrupt) and contraction (more gradual) behaviour across the metal-insulator phase transition was attributed to the formation of microdomains, e.g. [5, 7, 39]. Approaching the phase transition temperature during cooling, insulating microdomains

start forming throughout the crystal. Note that the phase transition of the individual microdomains is believed to occur in a step-like manner [5]. The macroscopic needle length, however, decreases over a few kelvin as the number of insulating microdomains increases. As long as there are enough still metallic microdomains which remain connected, the conductivity shows metallic behaviour. At some stage the connection between the metallic microdomains is no longer in tact throughout the crystal. Just one interruption of connectivity suffices to break the circuit and cause a sudden, dramatic decrease in conductivity. This model was referred to as "connectivity limited conductivity" by Schmitt *et al.* [5]. The contraction along the c-axis continues gradually regardless of the connectivity between the metallic microdomains. During heating of the sample the same process occurs in reverse: At some stage the circuit of already metallic microdomains is closed, causing a sudden jump in conductivity. The model of microdomain formation could therefore explain the different temperature ranges across which the macroscopic electric and expansion phase transitions occur in the Cu-DNCQI salts.

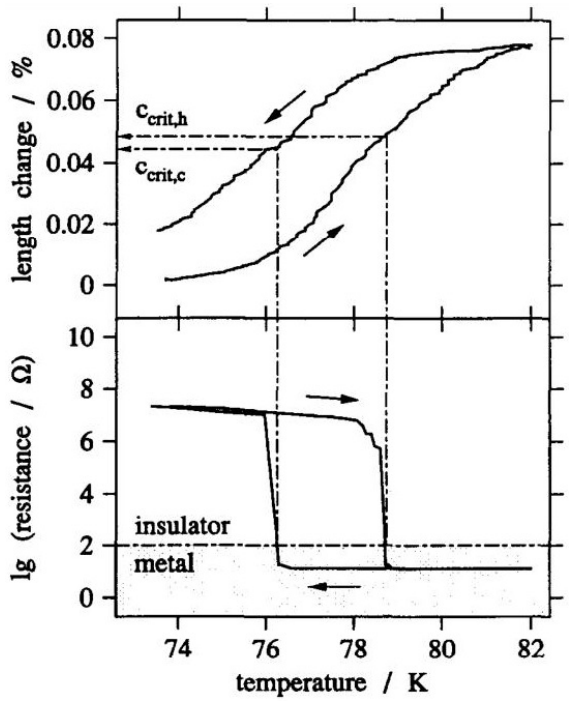

Figure 2.6: Interferometric measurements of the temperature dependence of the length of a d_6 Cu(DCNQI)$_2$ crystal compared to the resistivity behaviour in the same temperature range during heating and cooling [5].

Another striking feature of the temperature versus conductivity curve of all DCNQI salts (Figures 2.6, 2.10) and their expansion/contraction curves (Figure 2.6) is the prominent hysteresis effect between cooling and heating cycles. Shifts in the phase transition temperature of 10 K – 20 K have been recorded [5, 9]). Bauer *et al.* [7] proposed that the formation of domains causes mutual stresses between the crystalline sites which triggers the charge ordering of the copper ions and the CDW development along the DCNQI stacks at different temperatures during cooling and heating. The importance of this effect for our experiments will be explained later in this Section.

Another way to gain structural information of the different phases of the $Cu(DCNQI)_2$ crystals, besides the dilatometric measurements performed by Karutz *et al.* [9], are x-ray diffraction experiments [6]. Figure 2.7 is an image of the x-ray diffraction experiments performed by H. Kobayashi *et al.* in 1993 [6]. In the 300 K metallic phase only Bragg spots occur in the x-ray diffraction pattern with a c^* periodicity. At 20 K, in the insulating phase two lines of satellite CDW spots appear with $\frac{c^*}{3}$ periodicity between the lines of Bragg peaks – indicated by the smaller arrows (see Section 2.2 for a definition of c^*). These measurements were taken for a DMe/DBr alloyed $Cu(DCNQI)_2$ crystal. Similar CDW spots (with the same periodicity) are expected to occur for the d_6 $Cu(DCNQI)_2$ salt reported on in this study (see Chapters 3, 4).

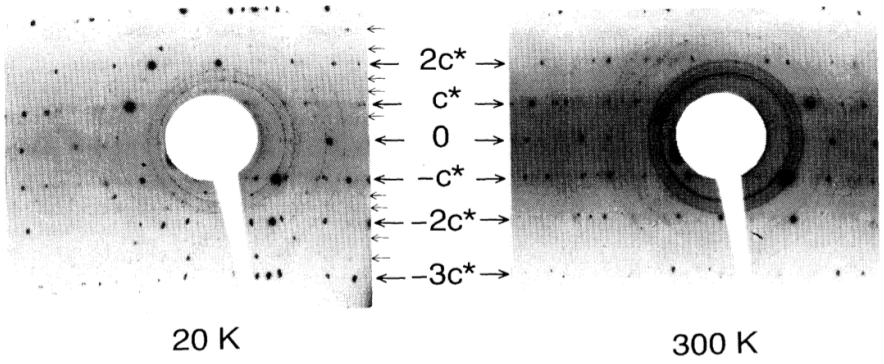

Figure 2.7: X-ray diffraction images at 300 K and 20 K of the alloy $Cu(DMe_{0.9}DBr_{0.1}\text{-}DCNQI)_2$ as reported by H. Kobayashi *et al.* in 1993. The larger arrows indicate the lines of Bragg spots, while the small arrows show the position of the three-fold superlattice spots [6].

As mentioned before, during the phase transition from the metallic to the insulating phase huge jumps in conductivity have been observed in several members of the $Cu(DCNQI)_2$ salt family, e.g.

[7, 9]. The curves in Figure 2.8 show a distinct difference between different copper salts' conductivity behaviour during cooling. $Cu(DNCQI)_2$ salts can be divided into three different groups with respect to their metal-insulator phase transition behaviour:

- Group I materials remain metallic down to very low temperatures (<1 K), e.g. fully protonated h_8 $Cu((CH_3)_2\text{-}DCNQI)_2$ [28] and $Cu((CH_3O)_2\text{-}DCNQI)_2$ [2].
- Group II crystals show one metal to insulator phase transition during cooling (at T_{MI_1} ~60 K – 80 K), e.g. partially deuterated d_6, $Cu(2,5\text{-}(CD_3)_2\text{-}DCNQI)_2$ [15].
- Group III salts first undergo a metal to insulator phase transition (at T_{MI_1} ~50 K – 60 K) and then a reentry into the metallic phase at very low temperatures (at T_{MI_2} ~25 K – 35 K). In other words they display M–I–M behaviour, e.g. alloys of deuterated and undeuterated $Cu(DCNQI)_2$ (h_8/d_6 = 70%:30% [7]).

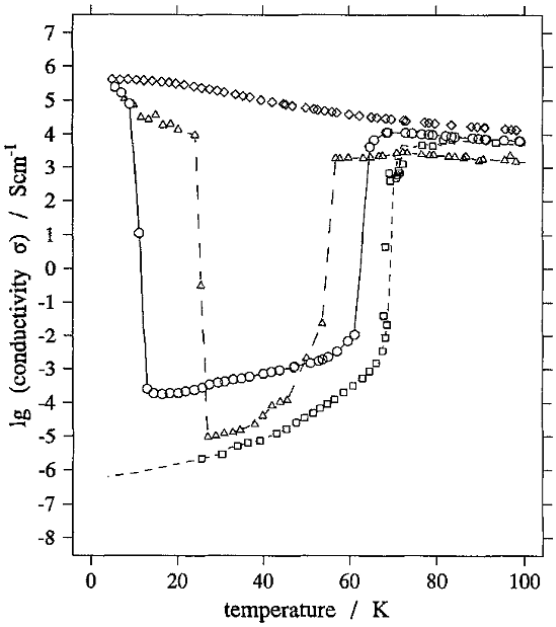

Figure 2.8: Temperature dependences of DC conductivity in four different single crystals of $Cu(R_1,R_2\text{-}DCNQI)_2$ during cooling [7]. Open diamonds: h_8 $Cu(2,5\text{-}(CH_3)_2\text{-}DCNQI)_2$. Open squares: d_6 $Cu(2,5\text{-}(CD_3)_2\text{-}DCNQI)_2$. Open triangles: alloy h_8/d_6 70%:30%. Open circles: alloy h_8/d_6 50%:50%.

Figure 2.8 shows the temperature dependence of the DC conductivity of four different $Cu(R_1,R_2\text{-}DCNQI)_2$ molecules – differing in their R_1, R_2 group substituents – falling into these three groups

[7]. The low temperature metallic phase, displays the same conductivity behaviour as the high temperature metallic phase and is thus believed to have the same chemical properties [34].

A transition from group I to group II or III (or vice versa) can be induced by changing the external or internal (so called effective) pressure (e.g. via deuteration or substituting side-groups (which are more or less bulky)) (see also Figure 2.9). As shown in Figure 2.8 varying the side groups, R_1, R_2, in the Cu(DCNQI)$_2$ crystals, dramatically affects the phase transition behaviour. The effective pressure influences the tetrahedral coordination geometry around the metal counter ion, in other words, changing the angle, α, between the Cu ion and any two N-atoms of the DCNQI ion (see Figure 2.1(b)). As described before, the distortion of the tetrahedron around the copper atom away from its ideal, destabilises the metallic phase, forcing the sample to undergo a phase transition to the insulating state. For example, in Table 2.1 the change in coordination angle (α) upon cooling, is recorded for undeuterated (h_8) and deuterated (d_6) methyl side groups of the DCNQI molecule in the copper salt. The change in α seems to be cumulatively affected by the pronounced contraction along the c-axis ($\Delta c_{h_8} \sim 2.3$ %; $\Delta c_{d_6} \sim 2.5$ %), while the a-axis undergoes a slight contraction ($\Delta a_{h_8} \sim 0.23$ %; $\Delta a_{d_6} \sim 0.34$ %). This anomaly was also reported by A. Kobayashi *et al.* in 1987 [28]. The increase in α is more pronounced in the d_6- than in the h_8-salt($\Delta\alpha_{h_8} \sim 1.2$ %; $\Delta\alpha_{d_6} \sim 3.0$ %). As seen in Figure 2.8 the h_8-salt is a group I material with a stable metallic phase down to sub-kelvin temperatures, while d_6 Cu(DCNQI)$_2$ displays group II behaviour with one metal to insulator transition. This small change in bulkiness (exchanging H-atoms with D-atoms) of the methyl side group causes enough distortion of the coordination tetrahedron to induce a different phase transition behaviour with regards to the conductivity.

The influence of different mechanisms inducing effective pressure on the conductivity behaviour have been mapped out in phase diagrams, e.g. [17, 42]. Figure 2.9 shows a schematic of the phase behaviour of the temperature versus effective pressure – induced by bulky R_1,R_2 groups, deuteration, substitution of heavy isotopes of carbon and nitrogen, and doping with lithium ions and zinc ions. The metallic and insulating phases are indicated as well as the three groups of phase transition behaviour. From this schematic one can also see that changing the temperature can only induce phase transitions within the scope of the group's behaviour of the particular salt, i.e. a temperature change does not induce a transition to another group. Increasing the effective pressure on the other hand, induces a transition from a group I to a group II or III material. The reentry behaviour

into a metallic state – at low temperatures and intermediate effective pressures – of these organic molecular salts is not yet fully understood.

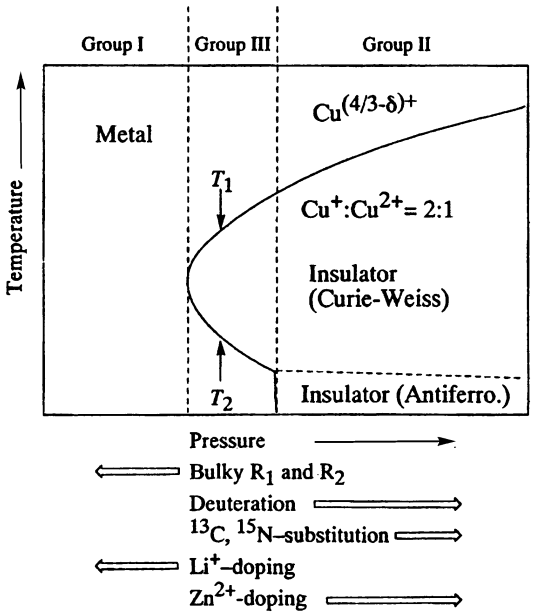

Figure 2.9: Schematic phase diagram for Cu(R_1,R_2-DCNQI)$_2$ salts: temperature versus effective pressure [8].

In our experiments we focused on the di-methyl copper salt of DCNQI: Cu(DMe-DCNQI)$_2$. As depicted in Figure 2.8 in its undeuterated (fully protonated) form (h_8, i.e. Cu((CH$_3$)$_2$-DCNQI)$_2$), dimethyl copper DCNQI falls into group I. Its partially deuterated form (d_6, i.e. Cu(2,5-(CD$_3$)$_2$-DCNQI)$_2$) with the six methyl hydrogens replaced by deuterium atoms displays group II behaviour. Forming an alloy of these two salts producing h_8/d_6 (either in a 70%:30% or 50%:50% ratio) transforms the crystal into a group III material [7]. (From here on all dimethyl copper-DCNQI salts will be referred to as Cu(DCNQI)$_2$. Where ambiguities might arise the specific deuteration state or alloy (i.e. h_8, d_6, or h_8/d_6) will be specified.) Tables 2.1 and 2.2 summarise the relevant lattice constants, coordination angles, and phase transition temperatures which have been referred to before and will be relevant for data analysis later.

Table 2.1: Lattice constants and geometric crystal data of h_8 and d_6 Cu(DCNQI)$_2$ at different temperatures as reported in [15].

Salt (temp.)	h_8 (300 K)	h_8 (20 K)	d_6 (300 K)	d_6 (20 K)
a, Å	21.606	21.655	21.619	21.693
c, Å	3.881	3.792	3.874	3.776
V, Å^3	1811.7	1778.1	1810.8	1776.8
α, (N-Cu-N), degrees	124.8	126.3	124.8	128.5

Table 2.2: Phase transition temperatures as reported by Bauer *et al.* [7]. T_{MI_1} refers to the higher temperature phase transition for the h_8/d_6 alloy (group III salt) and to the only phase transition for the partially deuterated d_6 salt (group II). T_{MI_2} is the lower (reentry) phase transition temperature of the alloy.

Cu(DCNQI)$_2$ salt	d_6	h_8/d_6 (70:30)
T_{MI_1} (K) (cooling)	70	55
T_{MI_2} (K) (cooling)		26
T_{MI_2} (K) (heating)		34
T_{MI_1} (K) (heating)	73	62

Now we consider the hysteresis effect observed in the conductivity versus temperature behaviour, as well as in the length changes (see Figures 2.6, 2.10) once more. This large hysteresis effect makes it possible to switch from one phase to another using light pulses [38]. Considering Figures 2.10 and 2.11 this phenomenon can be explained. In Figure 2.10 the three "operation points" (op1, op2, op3) are indicated which were chosen by Karutz *et al.* [9] to perform their light-switching experiments on the h_8/d_6-(70%/30%)-Cu(DCNQI)$_2$ alloy with group III conductivity behaviour (see also Figure 2.8 [7]).

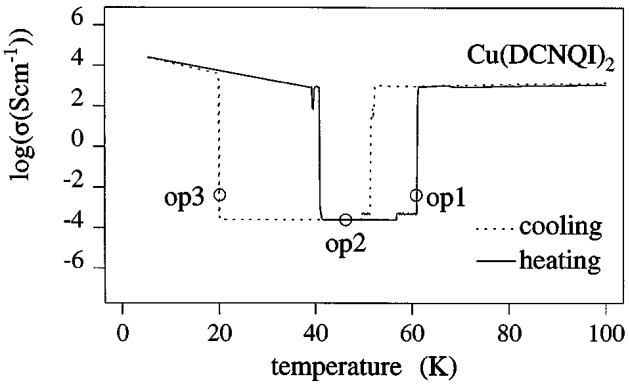

Figure 2.10: Conductivity versus temperature curve as reported by Karutz *et al.* displaying a strong hysteresis effect between the cooling and heating cycles [9].

Operation point one (op1) lies on the insulating side of the edge of the insulator to metal phase transition of the heating curve. This implies that providing a small amount of energy to the system (e.g. in the form of light) induces the phase transition. Since this transition occurs at a higher temperature than on the cooling curve, one expects the induced phase transition to be long lasting (the crystal has to cool down at least $\sim$ 10 K from the conducting state on the heating curve to reach the metal to insulator phase transition temperature on the cooling curve, before it can enter its insulating state again). A similar scenario is expected at the reentry transitions at op3. Here the sample is still an insulator but lying on the edge of the insulator to metal transition upon cooling. Adding the right amount of energy to the system at this point "kicks" the sample into the metallic phase on the heating curve. Again the phase transition temperature on the cooling curve is much lower ($\sim$ 20 K). Therefore it should take long for the sample to "fall back" into the insulating state. Indeed, Figure 2.11 (a) and (c) confirm these expectations for op1 and op3. The steep initial rise of these two curves indicates a fast switch from the insulating to the metallic phase, while the slower decaying tail indicates that the reversal of that transition takes more time. Operation point two, op2, is quite different from the other two. The sample is in the insulating phase, at a point where the cooling and heating curves coincide. Figure 2.11(b) shows that the sample seems to resist the phase transition into the metallic state. This is evident from the lower maximum transient current reached during excitation with the light pulse. The maximum current measured for op2 is an order of magnitude lower than for op1 and op3. Also, the decay of the signal is in the order of fractions of a nanosecond at op2. This is a lot faster than the hundreds or even thousands of nanoseconds it took for the sample to decay back to the insulating state at op1 and op3 respectively.

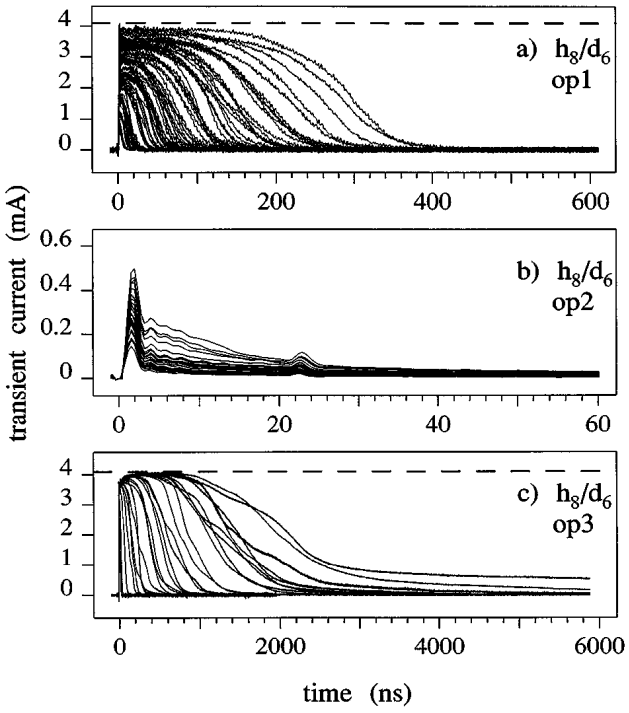

Figure 2.11: Conductivity behaviour during light switching between the metal and insulator phases of h_8/d_6-(70%/30%)-Cu(DCNQI)$_2$ reported by Karutz *et al.*. Transient current measurements as a function of time were conducted on single crystals of the alloy. The light pulses in these measurements were 30 ps long and at a wavelength of 533 nm. The temporal resolution of these measurements was in the order of 50 ps [9].

These experiments demonstrate that switching between the metallic and insulating phases of partially deuterated salts of Cu(DCNQI)$_2$ is possible. The switching occurs on time scales faster than 100 ps and, depending on the initial temperature of the sample, i.e. at which operation point it is, the decay back to the original state occurs on sub-nanosecond to microsecond time scales.

In this section the chemical and physical properties of Cu(DCNQI)$_2$ salts that give them their extraordinary conductivity behaviour in their metallic state have been summarised. Also the metal-insulator phase transitions governed by the unique crystal geometry which influences the electronic state of the constituents and therefore of the entire organic molecular salt were outlined. Structural analysis using x-ray diffraction has proven to provide valuable information about the crystal lattice in different metallic states and CDW formation has been observed in the form of satellite peaks.

It has also been shown that phase transitions can be induced by light pulses due to the hysteresis effect. The light induced phase switching showed fast dynamics in the conductivity experiments performed so far.

2.2 Diffraction Theory

In this section the theoretical background of using diffraction (and in particular electron diffraction) as a means to gain structural information about materials relevant to our experiments is outlined.

Diffraction of electromagnetic waves, e.g. visible light (400 nm – 700 nm) and x-rays (∼0.01 nm – 10 nm), as well as of particles (using the wave nature of particles), e.g. neutrons (∼0.1 nm) and electrons (∼2 pm – 10 pm), can be used as a means to gain structural information about matter. Radiation of shorter wavelengths can resolve smaller structures. Electrons can be accelerated through high potential fields to obtain energy corresponding to a wavelength of a few picometres, while visible light has wavelengths which are four to five orders of magnitude larger. Therefore electrons instead of visible light are used when atomic structures – which are in the order of a few tens to hundreds of picometres – are to be investigated. The following discussion on the aspects of electron diffraction theory which are most relevant for the experiments presented here, is a broad summary from [12].

As mentioned above, electrons can be thought of as waves. The de Broglie wavelength of electrons with a certain energy (i.e. travelling at a certain speed) can be calculated in the following manner:

$$\lambda = \frac{h}{p} = \frac{h}{m_e v} = \frac{h}{\sqrt{2 m_e e U}}, \tag{2.1}$$

where λ is the de Broglie wavelength, $h = 6.626 \times 10^{-34}$ m^2 kg s^{-1} (Planck's constant), p is the momentum of the accelerated electrons, $m_e = 9.109 \times 10^{-31}$ kg (the resting mass of an electron), $v = \sqrt{\frac{2eU}{m_e}}$ (the velocity of an electron), $e = 1.602 \times 10^{-19}$ C (the elementary charge), $U = 30$ kV (the potential energy difference through which the electrons are accelerated from cathode to anode in our setup, see Section 2.3). When relativistic effects have to be taken into consideration, i.e. $E^2 = p^2c^2 + m_e^2c^4$ (where $c = 2.998 \times 10^8$ m s^{-1}, the speed of light in vacuum), the de Broglie equation becomes

$$\lambda = \frac{h}{\sqrt{2 m_e e U}} \frac{1}{\sqrt{1 + \frac{eU}{2 m_e c^2}}}. \tag{2.2}$$

Calculating the de Broglie wavelength from Equations 2.1 and 2.2 yields 7.08×10^{-12} m and 6.98×10^{-12} m, respectively. These values only differ by ∼1 %. We can therefore assume the

relativistic effects to be insignificant in our measurements and the wavelength of our electron beam is taken as 7 pm for further discussions.

Due to the wave nature of the electron beam, conventional diffraction theory can be applied, i.e. the electrons behave like waves scattered off the material and interfering constructively or destructively to form a diffraction pattern. Figure 2.12 depicts the geometrical considerations for reflection off two parallel crystal planes. The incident beam is described by the wave vector $\mathbf{k}_0$ and the reflected beam by $\mathbf{k}$ (indicated in red in Figure 2.12). Elastic scattering off a specific set of parallel lattice planes is considered during this interaction and therefore the angle of incidence and reflection are equal in magnitude to each other, i.e. $\theta_{incident} = \theta_{reflected} = \theta$. Additionally considering the inter-planar distance (d) and the wavelength of the incident beam (λ), the geometry in Figure 2.12 can be used to calculate the Bragg condition for constructive interference. After one beam has been reflected off the top plane and the other off the lower plane the travelled path difference between the beams is $2d\sin\theta$. In order the beams to interfere constructively after reflection, their path difference needs to equal an integer number of wavelengths. Thus Bragg's law for constructive interference (i.e. formation of a diffraction peak) after reflection off parallel crystal planes is derived as stated in Equation 2.3.

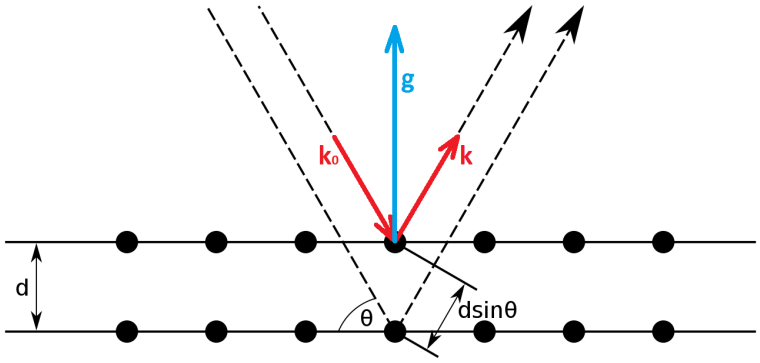

Figure 2.12: Geometry of reflection off crystal planes leading to the Bragg condition [10]. One plane wave is incident (at an angle θ between the crystal planes and the incident beam) on two parallel planes of a crystal (separated by inter-plane-spacing d). The reciprocal wave vector $\mathbf{g}$ is indicated in blue in the figure. It lies perpendicular to the scattering planes. It is defined as $\mathbf{g} = \mathbf{k} - \mathbf{k}_0$.

Bragg's law of reflection off parallel (crystal) planes is given by the following equation:

$$2d \sin\theta = n\lambda, \tag{2.3}$$

where d refers to the spacing between the crystal planes off which diffraction occurs, the angle between the incident electron beam and the scattering crystal planes is given by θ, n is the diffraction order of the peak being considered, and λ is the wavelength of the incident beam being diffracted (in our case the de Broglie wavelength of the electrons).

In order to get a clearer understanding of how the crystal lattice and the final diffraction pattern are related, diffraction theory is formulated in terms of vector analysis. A crystal consists of a regular array of particles (e.g. atoms, molecules, ions). The simplest, repeating unit this crystal structure can be divided into is called the unit cell of the lattice. This unit cell is described by three non-coplanar fundamental vectors: $\mathbf{a}, \mathbf{b}, \mathbf{c}$. In order to reconstruct the entire crystal lattice this unit cell is translated by integer multiples of the fundamental vectors. The crystal lattice can be described by the magnitudes of the lattice vectors (also known as the lattice constants) $|\mathbf{a}| = a, |\mathbf{b}| = b, |\mathbf{c}| = c$ and the angles between the fundamental lattice vectors: α', β', γ', where α' lies between $\mathbf{a}$ and $\mathbf{b}$, β' lies between $\mathbf{b}$ and $\mathbf{c}$, and γ' lies between $\mathbf{c}$ and $\mathbf{a}$. (Note that α' is not the same as the coordination angle α in the $Cu(DCNQI)_2$ crystal shown in Figure 2.1(b).) For following discussions only orthogonal lattice vectors, i.e. $\alpha' = \beta' = \gamma' = 90°$, are considered, because $Cu(DCNQI)_2$ crystals have a tetragonal lattice.

Instead of viewing the crystal as a set of lattice points it can be described in terms of parallel, equidistant lattice planes formed by the regular array of lattice points. A set of lattice planes is characterised by their Miller indices (h, k, l) (since the plane closest to the origin intercepts the fundamental vectors at points $\frac{\mathbf{a}}{h}, \frac{\mathbf{b}}{k}, \frac{\mathbf{c}}{l}$, with h, k, l being integers) and they are separated by a distance d_{hkl}. For each crystal lattice there are many different sets of parallel, equidistant lattice planes, lying in different orientations, with different separating distances d_{hkl}. Diffraction is understood in terms of beams (or rather wave vectors) being reflected off these lattice planes. The diffraction pattern is part of the so called reciprocal space. The reciprocal lattice can be constructed from the lattice planes of the crystal. A set of lattice planes in real space with Miller indices (hkl) is represented by a point in reciprocal space with the same Miller indices. To geometrically construct these points making up the reciprocal lattice the following is done for each set of real lattice planes:

From the origin of the reciprocal lattice a vector normal to the lattice planes (hkl) with a length $\frac{1}{d_{hkl}}$ is plotted (this vector is called the reciprocal lattice vector $\mathbf{g}$). If this is done for each possible set of parallel lattice planes of the crystal the entire corresponding reciprocal lattice is formed. The points in this reciprocal lattice can be described by the reciprocal vectors $\mathbf{a}^*, \mathbf{b}^*, \mathbf{c}^*$. These reciprocal lattice vectors can also be calculated by vector analysis using the formula $\mathbf{a}^* = \frac{\mathbf{b}\times\mathbf{c}}{\mathbf{a}\cdot(\mathbf{b}\times\mathbf{c})}$. The other two reciprocal lattice vectors, $\mathbf{b}^*$ and $\mathbf{c}^*$, can be obtained by cyclic exchange of the real space lattice vectors, $\mathbf{a}, \mathbf{b}, \mathbf{c}$, in this formula. Note that $|\mathbf{a}^*| = \frac{1}{a}$, $|\mathbf{b}^*| = \frac{1}{b}$, and $|\mathbf{c}^*| = \frac{1}{c}$. The reciprocal lattice vector can be written as $\mathbf{g} = h\mathbf{a}^* + k\mathbf{b}^* + l\mathbf{c}^*$. It can be shown that the length of the reciprocal lattice vector is equal to the reciprocal of the lattice interplanar distance, i.e. $|\mathbf{g}| = \frac{1}{d_{hkl}}$. Consequently diffraction spots that are close to each other in reciprocal space, correspond to lattice planes which are far apart in the crystal lattice and vice versa.

With these mathematical tools and geometrical concepts, it is possible to calculate real lattice plane spacings (d_{hkl}) from the diffraction pattern consisting of points in reciprocal space. For example, for a simple cubic lattice, where $a = b = c$ and $\alpha' = \beta' = \gamma' = 90°$, where $|\mathbf{a}^*| = |\mathbf{b}^*| = |\mathbf{c}^*| = \frac{1}{a}$, it can be shown that $d_{hkl} = \frac{a}{\sqrt{h^2+k^2+l^2}}$. This, however, presupposes that the Miller indices of the relevant diffraction spots are known, which may be difficult for more complex crystals consisting of different atoms and forming more complicated lattice structures.

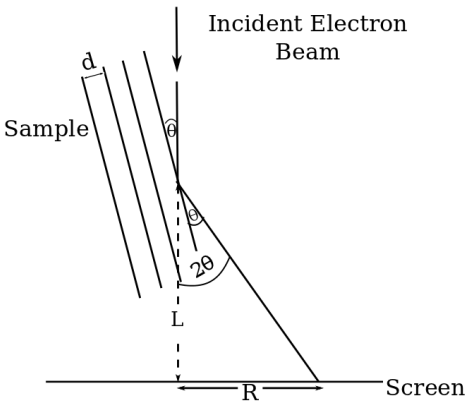

Figure 2.13: Diffraction camera geometry. The incident electron beam is reflected off a set of parallel lattice planes separated by a distance d. The angle between incident beam and lattice planes is θ and equal to the reflected beam's angle with the planes (the same angle as in the Bragg equation 2.3). (Figure adapted from [11].)

An alternative way of finding the d-spacing (for simpler notation $d = d_{hkl}$) of the lattice planes from the diffraction pattern is derived by considering the geometry of the diffraction setup (also referred to as the diffraction camera). A schematic is shown in Figure 2.13. From this setup geometry one can see that

$$\tan(2\theta) = \frac{R}{L}, \tag{2.4}$$

where R refers to the distance between two diffraction spots on the detector screen. L is the distance between the sample and the detector screen (35 cm in our setup). The angle (2θ) is formed between the undiffracted beam and the diffracted beam.

In transmission electron diffraction the angles θ, through which electrons are diffracted, are very small (1° – 2°) [43]. Therefore $\tan(2\theta) \approx 2\sin\theta$ holds. From this it follows that

$$d = \frac{\lambda L}{R}. \tag{2.5}$$

Therefore, when the wavelength and sample-detector distances are known, R can be obtained from measurement on the diffraction image, and d can thus be calculated. This can be done without knowing the Miller indices of the diffraction spots.

Note, however, that the diffraction pattern does not include the entire reciprocal lattice which can be constructed from the parallel lattice planes of the crystal. To find the reciprocal lattice points which can be observed in a diffraction pattern one makes use of the Ewald sphere. The Ewald sphere is constructed in reciprocal space as follows: The incident wave vector ($\mathbf{k}_0$) is drawn with its arrow head at the origin of the reciprocal lattice with a length $|\mathbf{k}_0| = \frac{1}{\lambda}$ (where λ is the wavelength of the incident radiation). The 'tail' of $\mathbf{k}_0$ is then taken as the centre of a sphere of radius $\frac{1}{\lambda}$. Since for elastic scattering $|\mathbf{k}_0| = |\mathbf{k}| = \frac{1}{\lambda}$ must hold – momentum is conserved – $\mathbf{k}$ lies in the Ewald sphere as well. At an angle 2θ with respect to $\mathbf{k}_0$, the reflected wave vector ($\mathbf{k}$) is drawn tail to tail with the incident wave vector. The vector connecting the tips of $\mathbf{k}_0$ and $\mathbf{k}$ is the reciprocal vector $\mathbf{g}$. These are the same vectors indicated in Figure 2.12, but just shifted around. From this vector diagram in Figure 2.14 it becomes clear that $\mathbf{k} - \mathbf{k}_0 = \mathbf{g}$. This can be shown to be the Bragg condition in vector form. Therefore, only reciprocal lattice points intersecting the Ewald sphere satisfy the Bragg condition for constructive interference and will thus occur in the diffraction pattern.

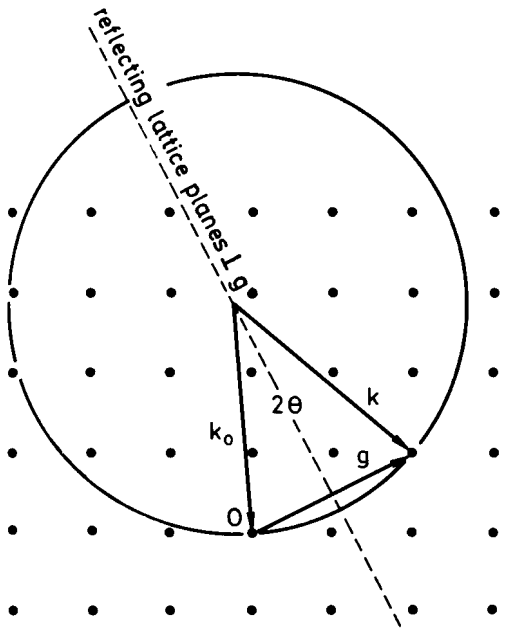

Figure 2.14: Ewald sphere construction in reciprocal space. The incident wave vector ($\mathbf{k}_0$), reflected wave vector ($\mathbf{k}$), and the reciprocal lattice vector ($\mathbf{g}$) are indicated. (Figure adapted from [12].)

The intensity of the diffraction peaks resulting from the scattered waves' interference depends on the structure of the lattice (the so called structure amplitude) as well as on the shape of the crystal (the lattice amplitude). The structure amplitude depends on the positions of the atoms in the unit cell as well as on the scattering strength of each atom. Since the electrons interact with the scattering atoms via Coulomb interactions, the scattering strength of an atom depends on the strength of its Coulomb field (which scales with its atomic number). Larger or heavier atoms will therefore scatter the electrons more strongly than lighter atoms. The position of the atoms in the unit cell determine which set of parallel planes will allow for constructive interference, i.e. for which sets of lattice planes the Bragg condition holds producing diffraction peaks during an experiment. Together the position and types of atoms in the unit cell therefore influence the structure amplitude, which in turn influences which reciprocal points are allowed for the crystal and at which intensity they may be observed in the diffraction pattern. The lattice amplitude depends only on the external dimensions of the sample. The effect can be interpreted as a change in the shape of the reciprocal points. For example, a thin crystal foil, with the incident electron beam normal to its surface produces rod-like reciprocal points (elongated in the direction of the electron beam). This elongation of the reciprocal lattice points allows the Ewald sphere to intersect more of them, i.e. the Bragg condition is relaxed,

and more diffraction spots are visible. The shape of the crystal therefore influences the shape of the reciprocal points, which in turn affects which peaks occur in the experimental diffraction pattern.

The principles of diffraction which are relevant for our electron diffraction experiments have been discussed. They form the basis for the experimental setup and are necessary for the interpretation of the experimental data.

2.3 Ultrafast Electron Diffraction: experimental setup

Having presented the sample, $Cu(DCNQI)_2$, as well as fundamentals of diffraction theory, the ultrafast electron diffraction setup with which we wish to investigate the crystal can now be introduced. Figure 2.15 shows the fundamental elements of the ultrafast electron diffraction experiment.

Our experimental setup is based on the principles of the ultrafast pump probe technique [44]. A pulsed laser beam is split up into two paths: the so called pump beam excites the sample, while the probe beam measures the state of the sample at a certain time before or after excitation. The time at which the sample's excitation state is measured depends on the relative delay between the pump and probe pulses arriving at the sample. This delay is controlled by a delay stage included in one of the two beam paths. In this way the pump and probe beam's path length can be varied relative to each other. The idea is to capture diffraction images of the sample at increasing delay times after excitation. When these diffraction images are stringed together the gradual change as a function of time after excitation can be investigated – like a film of the changing diffraction pattern. The temporal resolution of these measurements does not depend on the detection speed, but on the duration of the pump and probe pulses and the step size of the delay stage. In our setup the temporal resolution is $\sim$500 fs. Therefore changes in the diffraction pattern on time scales of a few hundred femtoseconds are resolvable with this ultrafast pump-probe technique.

For ultrafast electron diffraction the pulsed probe beam in the pump-probe setup is converted into short electron pulses. As described in Section 2.2 diffraction techniques are used to gain structural information of a sample. In order to resolve structures on atomic length scales ($\sim$10 Å) short wavelength radiation is needed. Therefore electron diffraction is chosen with which de Broglie wavelengths in the order of a few picometres can be achieved. Converting the laser probe beam to a

pulsed electron beam results in an ultrafast electron diffraction experimental setup. The fundamental elements of our UED setup in Figure 2.15 are first outlined now and are discussed in more detail thereafter.

A Clark-MXR CPA 2101 laser provides the fundamental laser beam. It emits short pulses (150 fs) at a central fundamental wavelength of 775 nm, a repetition rate of 1 kHz, and a pulse energy of roughly 800 μJ. This laser beam is split into two beam paths: the pump (bottom path) and the probe (top path). The **probe beam** is steered through a variable filter for beam attenuation and thus energy control, through a lens which focusses the beam onto a non-linear optical BBO crystal followed by a half wave plate and another BBO crystal. This series of optical elements frequency triples the fundamental laser light. The emitted third harmonic light is steered via a periscope to reach the height of the vacuum chamber's entry window, through a lens focussing it on a gold cathode inside the electron gun. Utilising the photoelectric effect the electron gun part of the vacuum chamber changes the pulsed third harmonic laser beam into a pulsed electron beam. These electron bunches are accelerated from the photocathode to the anode through a 30 kV potential. Thereafter the electrons travel through a magnetic lens which focusses the electron beam, and are then diffracted by a thin crystalline sample in transmission. The emerging electron beam's interference pattern is captured by a multi channel plate amplifying the electron signal, followed by a phosphorescent screen of 40 mm diameter. Outside the chamber, directly behind the detector screen a macro lens images the diffraction pattern onto a 16-bit CCD camera which records the data. The **pump beam** is steered to a delay stage which allows control of its path length relative to the probe beam's path length with micrometer accuracy. A periscope brings the light to the correct height for entry into the vacuum chamber. A variable density filter allows for beam attenuation and therefore control over the amount of energy deposited into the sample before the beam is steered through a quartz window into the vacuum chamber. Via two mirrors, one of which can be adjusted piezo electrically, the pump beam is guided onto the sample. The energy deposited into the sample by the pump beam causes structural changes which are observed via the electron probe beam's diffraction. A closed cycle helium cryostat allows for temperature control of the sample between 30 K – 400 K.

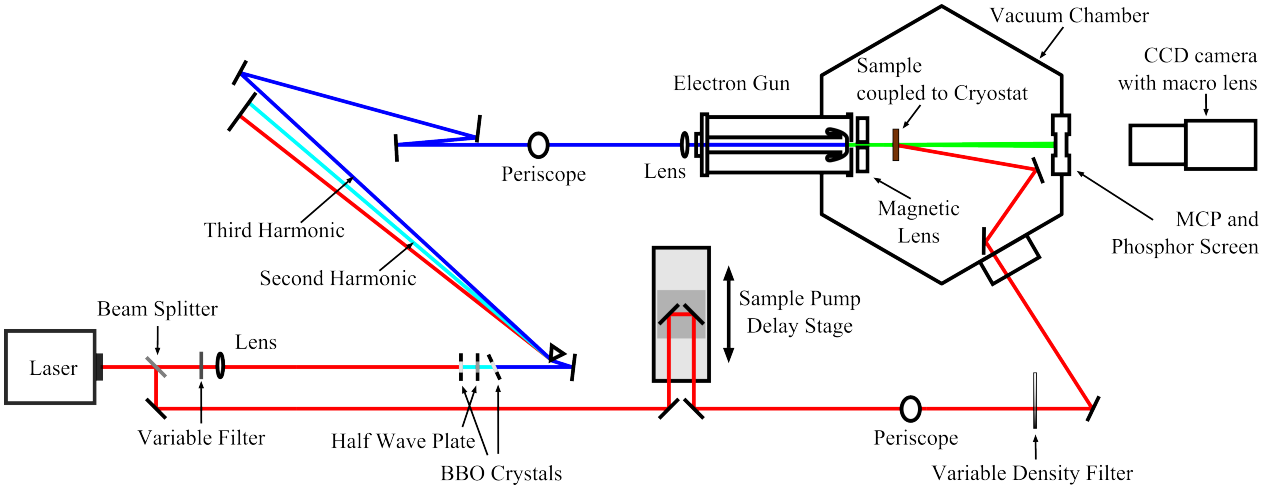

Figure 2.15: Schematic overview of the UED setup.

Frequency tripling of the fundamental laser beam

In order to create an electron probe beam from the fundamental laser beam, the photoelectric effect is utilised. To meet the requirements for this effect to be efficient at the gold photocathode in the electron gun, i.e. provide light with the correct energy needed for electron emission, the fundamental 775 nm laser light's frequency has to be tripled. The frequency tripling is a two step process: During the first step the second harmonic is generated in a BBO crystal (a non-linear optical element used to obtain higher harmonics of a fundamental laser beam source) resulting in a wavelength of 388 nm. Thereafter the light passes through a half-wave plate in order to align the fundamental and second harmonic's polarisation parallel to each other. In a second BBO crystal sum-frequency generation of the fundamental and second harmonic yields frequency tripled light at a wavelength of 258 nm [45, 46]. By turning the half-wave plate the efficiency of the sum-frequency generation process and thus the intensity of the UV light can be controlled. The 258 nm wavelength light is needed to ensure an efficient photoelectric effect at the gold photo cathode. After passing through the two BBO crystals the beam contains the fundamental, second and third harmonic frequencies. These are spatially separated by a prism. Since only the frequency tripled light ($\lambda = 258$ nm) is used to produce electron pulses, the lower two frequencies are simply stopped with a beam block.

Photoelectric effect at the photocathode

At the photocathode of the electron gun the UV laser beam obtained via frequency tripling is converted into a pulsed electron beam. A gold cathode is used (consisting of a quartz window coated

with ∼20 nm of gold on the surface inside the vacuum chamber) as the entrance window to the electron gun. Electrons are produced in transmission by the photoelectric effect. The work function of a ∼150 nm thick gold foil was experimentally determined to be 5.10 eV (8.17×10^{-19} J) [47]. The value of the work function may, however, vary by ±15 % depending on the thickness and crystalline orientation of the gold foil [46]. With this value of the work function the wavelength of light needed for emitting electrons from a foil of 150 nm thickness was calculated to be 241 nm ± 36 nm (using the formula $\lambda = \frac{hc}{E}$, where E is the work function, h is Planck's constant, c is the speed of light in vacuum, and λ is the wavelength)[46]. Therefore the generated 258 nm light is sufficient for electron emission in our electron gun from the ∼20 nm thin gold layer. Because of the pulsed nature of the laser light used to excite the free electrons from the photocathode, the resulting electron beam is also pulsed at the same frequency (1 kHz). The electron gun is explained in detail in Reference [46].

Electron propagation in vacuum

Since electrons do not propagate well in air (the stopping distance in nitrogen, the main constituent of air, at atmospheric pressure is about 2 cm for 30 keV electrons [48]), electron generation, acceleration, propagation, and diffraction need to be executed in a vacuum chamber. The vacuum chamber has a volume of about (50×50×50) cm^3 and a pressure in the order of 10^{-6} mbar can be achieved. After excitation the electron pulses are accelerated toward an anode at 30 kV. This means that the electrons reach an energy of 30 keV which corresponds to a de Broglie wavelength of about 7 pm (as calculated in Section 2.2 from Equations 2.1 and 2.2). After passing through a hole in the anode, the pulsed electron beam is then focused by a magnetic lens. Changing the current of the magnetic lens varies the focal strength of it, allowing for focus adjustment of the electron beam. The beam is focused on the detector in order to produce sharp diffraction images. Due to space-charge effects in the electron bunches, causing temporal broadening of the electron pulse as it propagates, the sample has to be positioned as close as possible to the cathode. An ASTRA code simulation [49] was done to model the space-charge effects on electron pulse length versus propagation distance. Simulation results showed that for pulses containing 10000 electrons a sample-to-cathode distance of 6 cm resulted in pulse durations of more than 1200 fs. For a short distance of 1 cm the pulse would be about 400 fs long for the same amount of electrons per pulse. Pulses containing 1000 electrons travelling 6 cm, resulted in 300 fs long pulses, and for 1 cm, less than 200 fs duration could be achieved [50]. In our current vacuum chamber a cathode-to-sample distance of 5 cm is realistically possible with one magnetic lens in place. For this 5 cm distance, pulse durations of about 300 fs are achievable for

1000 electrons per pulse. For 10000 electrons, the pulse duration would be in the order of 1 ps after 5 cm. These considerations are of importance for the time-resolved measurements we are aiming for.

Electron beam at the sample

At the sample the electron beam has a diameter of about 200 μm. In order to utilise as many electrons as possible to create bright diffraction patterns the sample area should be of a similar size as the electron beam. Samples are mounted on apertures of 100 μm diameter (see Section 3.1 for more details on the advantages of this method). An amount of 1000 electrons per pulse with a beam diameter of 200 μm corresponds to about 30 electrons per square micrometer per second irradiating the sample, which in turn corresponds to 5×10^{-18} C μm^{-2} s^{-1}. Drummy *et al.* reported destruction of crystallinity of the organic superconductor pentacene [23] – consisting of a chain of five aromatic rings – at a threshold of 3.5×10^{-10} C μm^{-2}, for 5 keV electron energy [51]. The electron radiation in our setup is eight orders of magnitude below this threshold. Therefore, even though our electrons have an energy six times higher than in the experiment of Drummy *et al.*, our sample (containing the organic DCNQI molecule) should not be damaged by the electron radiation. The electron beam is diffracted by the crystalline sample in transmission. Therefore the samples have to be thin enough to allow the electrons to pass through. For transmission electron microscopes operating at 200 keV the samples have to be in the order of 100 nm or thinner [12]. Since our setup operates at an order of magnitude less electron energy, the optimal sample thickness is expected to be thinner to allow electron transmission. Previous experiments on the transition metal dichalcogenides $TaSe_2$ and TaS_2 have shown good diffraction patterns at a sample thickness of about 30 nm [50, 52]. Since $Cu(DCNQI)_2$ is metallic at room temperature as well – similar to the samples investigated by Haupt in our UED setup [50, 52] – it was expected that a similar sample thickness would yield good diffraction patterns. The electron probe beam thus places certain constraints on the sample for these experiments, in terms of electron flux it can withstand and dimensions which are suitable.

Laser beam at the sample

The sample is also illuminated by the pump beam. Typically the fundamental beam emitted by the laser ($\lambda = 775$ nm) is used for experiments. If the need arises a wavelength tunable NOPA setup on the neighbouring optical table in our laboratory can be used to steer a beam of a different desired wavelength onto the sample for excitation. In our setup the excitation beam falls onto

the sample anti-parallel with respect to the electron probe beam (as can be seen an Figure 2.15). The laser beam diameter on the sample is in the order of 1 mm [50, 53]. This is larger than the electron beam diameter (200μm) and also the exposed sample's diameter (100 μm). Therefore the diffraction images obtained are ensured to result from a homogeneously excited sample. Karutz *et al.* reported an optical penetration depth on bulk Cu(DCNQI)$_2$ salts to be 100 nm at an excitation wavelength of 533 nm [9]. Absorption measurements performed in our laboratory (see Section 3.4) confirm these results. Therefore a sample thickness of less than 100 nm would also be suitable for homogeneous laser excitation of the sample.

Sample temperature control by the cryostat

In order to control the sample temperature (and therefore enable investigation of temperature dependent phase transitions) the sample is thermally coupled to a closed circuit helium cryostat – a closed cycle, low vibrational (optical) cryostat (Advanced Research Systems), driven by a water cooled helium compressor (model: ARS - 4HW), and controlled by a Model 335 Temperature Controller (LakeShore). The cryostat allows for temperature settings between 30 K and 400 K. (See Sections 3.1 and Appendix A for more detail).

Resolution of detected diffraction patterns

Detection and recording of the electron diffraction patterns is the final part of the experimental setup. The quality of a diffraction pattern depends, amongst other things, on the ability to spatially resolve the diffraction peaks. The spatial resolution of the recorded diffraction pattern is determined by the transverse coherence length ($L_\perp$) of the electron beam. In order to observe a crystalline structure, $L_\perp$ has to be substantially larger than the fundamental lattice constants of the sample crystal in order to produce a diffraction pattern from it. The lower limit of the coherence length can be estimated from the diffraction image itself (as is outlined in detail in Reference [53]). The ratio of the distance between two Bragg peaks (x) and the full width at half maximum (FWHM) of the Bragg peaks (Δx) gives an indication of the number of scattering planes contributing towards the diffraction pattern. This proportionality is also observed in a standard multi-slit diffraction experiment, where the diffracted peaks become narrower and their separation distance increases as the number of slits (N) increase. Multiplying this $\frac{x}{\Delta x}$ ratio by the corresponding crystal lattice constant (a, b, or c) gives the lower limit of the coherence length of the electron beam. For our setup, $L_\perp$ was determined to be in the order of 10 nm from previous experiments [53]. This is $\sim$30

times larger than the lattice constant along the c-axis, $c = 3.8$ Å, of the $Cu(DCNQI)_2$ crystal (see Table 2.1) [15] and thus enables well resolved, sharp diffraction peaks (e.g. Figure 4.1). The 10 nm coherence length is also about ten times larger than the CDW periodicity, $3c$, after trimerisation at low temperatures for $Cu(DCNQI)_2$. These structural changes should thus also be observable in our electron diffraction setup.

2.4 What makes UED a relevant technique to investigate organic molecular crystals such as $Cu(DCNQI)_2$?

In the previous sections the literature background of $Cu(DCNQI)_2$ salts was outlined as well as the theoretical and experimental background of ultrafast electron diffraction (UED). From this discussion it follows that UED investigations of this organic molecular salt promise to reveal more information about the structural phase transitions it undergoes. The following points summarise why $Cu(DCNQI)_2$ is an interesting sample for investigation in our UED setup:

- The crystal has room temperature lattice structure with a unit cell which is 30 times smaller than the coherence length of the UED setup. Therefore well resolved electron diffraction patterns can be obtained in order to analyse the metallic ground state's lattice structure.

- The phase transition involves structural changes in the crystal lattice in the form of a contraction along the c-axis [5, 9] as well as CDW formation (observed in similar samples in x-ray diffraction experiments [6]). With the UED setup's coherence length being ten times larger than the expected CDW periodicity we could also spatially resolve these low temperature (insulating phase) lattice modulations.

- Switching between phases can be induced by (laser) light of various wavelengths [5, 9]. In the UED setup we have access to a range of wavelength tunable laser light to illuminate the sample with. Light switching experiments of CDW samples have also been performed successfully in previous experiments in our setup [11, 50, 53].

- The fastest time scales involved in the conductivity behaviour of this phase switching have been demonstrated to be maximally 50 ps long, since this was the temporal resolution of the previous measurements by Karutz *et al.* [9]. Our temporal resolution of 500 fs of the current UED setup allows observation of even faster structural dynamics. Whether the structural changes of $Cu(DCNQI)_2$ occur on sub-picosecond time scales is to be investigated during our experiments.

Our goal is therefore to observe and temporally resolve the ultrafast structural changes occurring across different phase transitions of various $Cu(DCNQI)_2$ crystals using transient electron diffraction. The first steps towards that goal are described in this thesis: the preparation, introduction, and initial characterisation of $Cu(DCNQI)_2$ salts in the ultrafast electron diffraction experiment.

CHAPTER 3
SAMPLE PREPARATION AND INITIAL CHARACTERISATION

3.1 Sample Synthesis

Our samples were grown at the University of Würzburg by Florian Hüwe. The method used to grow the crystals is explained in detail in Reference [13]. Therefore only a short overview of the procedure will be given here. Figure 3.1 shows the electrolytic crystal growth setup used to synthesise the $Cu(DCNQI)_2$ crystals investigated in our experiments.

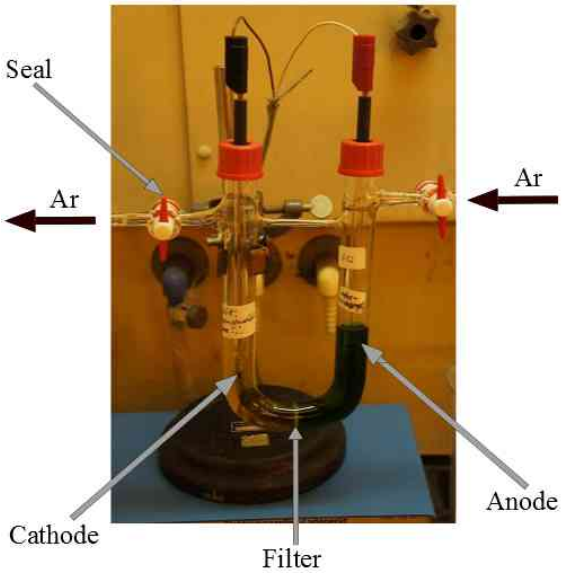

Figure 3.1: Electrolytic crystal growth apparatus as designed by Hüwe *et al.* (adapted from [13]).

The U-shaped glass pipe has a hollow glass bridge connecting the anode and cathode with each other at the top. Argon gas is flowed through this bridge (via a gas inlet and outlet connected to the tube with valves). This is done at several stages during the preparation and electrolysis processes to ensure inert conditions. At the bottom of the U-pipe a filter prevents diffusion of the anode products to the cathode. A potential difference is applied across the two plate-like platinum electrodes.

In preparation for the electrolysis procedure the cell and the electrodes are cleaned extensively, because the electrolytic crystal growth is extremely sensitive to impurities. The electrolyte filled into the cell contains DCNQI and copper(II)bromide dissolved in acetonitrile.

During electrolysis, crystal formation takes place at the cathode where DCNQI and Cu^{2+} are reduced to $DCNQI^{-}$ and Cu^{+}. The radical anion salt $(DCNQI^{-2/3})_2Cu^{+4/3}$ is formed from these constituents. The crystals preferably grow at the edges of the cathode where inhomogeneities may cause higher local electric fields. In Figure 3.1 a colour difference between the left and right hand side of the filter at the bottom of the U-shaped tube is noticeable. The Cu^{2+} ions in solution have a dark green colour (as seen on the anode side of the filter). DCNQI dissolved in acetonitrile has a yellow colour, while Cu^{+} ions are transparent. The reduction occurring at the cathode explains this colour distribution (and the fact that it coincides with the crystal growth front).

After the electrolysis is stopped the cathode is removed from the cell and the crystals are washed off the platinum plate and onto filter paper using acetonitrile. The crystals are then rinsed with diethylether and carefully separated (because they tend to break easily) using ultra-fine tweezers. Finally they are stored under inert conditions (e.g. in nitrogen gas) [13].

3.2 Conductivity measurement

Initial conductivity measurements were also performed on the crystals, by Florian Hüwe at the University of Würzburg (see Figure 3.2). This was done in order to verify whether the crystals do undergo the phase transition, whether they show the jump in conductivity, and to measure the exact phase transition temperature for these crystals.

Since $Cu(DCNQI)_2$ has a high conductivity ($\sim 10^3$ Scm^{-1} at room temperature and ambient pressure [28]), i.e. small resistivity, the influence of connecting wire resistance has to be minimised for more accurate conductivity measurements. A four-probe geometry circuit is therefore employed where separate pairs of current-carrying and voltage-sensing electrodes are connected to the sample. In this way the voltage sensing loop carries minuscule current resulting in an insignificant voltage drop due to the connecting wires' resistance. A more accurate resistance/conductance measurement is therefore possible using the four-probe geometry than with the conventional two-probe system,

where all current flows through the ammeter and voltmeter (or alternatively through the ohmmeter) [54]. Conductivity (σ) is calculated from the conductance (G): $\sigma = G\frac{l}{A}$, where l is the length of the Cu(DCNQI)$_2$ needle and A the cross-sectional area of the needle. The exact setup designed for the measurements done on our samples is outlined in detail in Reference [13]. Figure 3.2 shows the results of these measurements on a single d_6 Cu(DCNQI)$_2$ crystal.

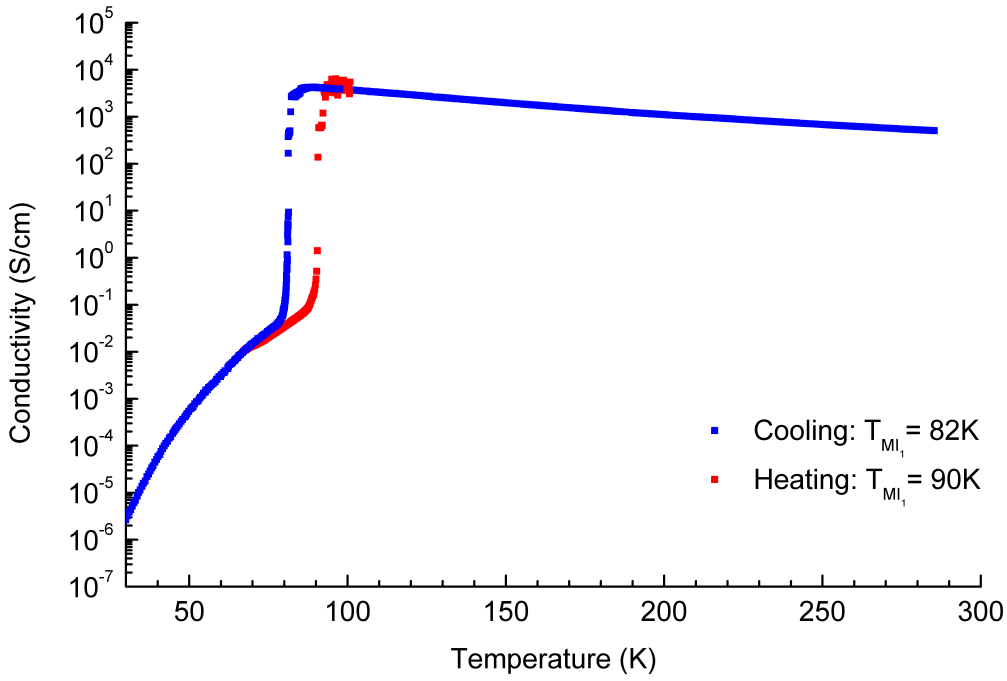

Figure 3.2: Conductivity measurement done on a d_6 Cu(DCNQI)$_2$ single crystal.

The conductivity jump over about six orders of magnitude is in the same order as reported by Bauer *et al.* [7] in Figure 2.8 for the d_6 salt. The phase transition temperatures indicated on this graph (82 K during cooling; 90 K during heating), however, differ quite significantly from those summarised in Table 2.2 [7] (by 17% for the cooling transition and by 23% during the heating transition). Hüwe's measurement shows a hysteresis shift by 8 K (where Bauer *et al.* [7] only report 3 K). As discussed in Section 2.1 the crystals' phase transition behaviour is sensitive to external and internal pressure effects (affecting at which temperature and in which range the transition occurs). It is therefore possible that during the conductivity measurement some pressure was exerted on the needle, which may have caused the transition temperature to shift up [5]. These measurements do, however, show that the phase transition does occur in these particular samples and that the order of magnitude of change in the conductivity is on par with previous reports for this type of DCNQI salt.

The synthesis of the crystals, confirmation of their phase transition and characterising the conductivity behaviour was performed in Würzburg. Thereafter the samples were ready for further preparation for ultrafast electron diffraction experiments at our laboratories at Stellenbosch University.

3.3 Sample cutting

In order to perform electron diffraction on crystalline samples in the UED setup described in Section 2.3 the samples need to be of a suitable size. The electron beam spot size at the optimal distance from the cathode (optimal in terms of pulse duration and space constraints in the vacuum chamber) is in the order of 100 μm – 200 μm. A transverse sample diameter of about 100 μm is therefore desirable. The thickness needs to be less than 100 nm for transmission electron microscope (TEM) measurements [12] where electron energies are in the order of a few hundred keV. In the UED setup electrons are accelerated through 30 kV, requiring samples that are <50 nm thick. Eichberger *et al.* [55] have investigated several sample preparation techniques to produce single crystalline, free-standing samples of these thin and large area dimensions which are suitable for ultrafast electron diffraction. Techniques using the focussed ion beam of a scanning electron microscope, ion milling with gallium ions, as well as reactive ion etching with SF_6 and CF_6 introduced significant levels of dopants (5 % – 15 %) which altered the sample significantly. These techniques were also tedious and time consuming (e.g. taking more than 10 hours for a single thin sample to prepare with ion milling). The method causing the least alterations of the sample and meeting the dimensional sample requirements controllably, repeatable, and efficiently was ultramicrotoming [55]. The samples produced during ultramicrotoming are homogeneously thick, no dopants are introduced, and several samples can be produced within an hour. Ultramicrotoming yielded good quality samples for previous experiments performed in our UED setup (e.g. $TaSe_2$ and TaS_2 investigated by Haupt [50]). This method was therefore also used for preparing thin slices of $Cu(DCNQI)_2$.

Ultramicrotoming

An ultramicrotome (Leica EM UC7) is used for cutting the sample into thin slices (about 30 nm thick). Photographs showing the entire instrument, and a zoomed in view of the cutting arm and the diamond knife are shown in Figures 3.3 (a) and (b) respectively.

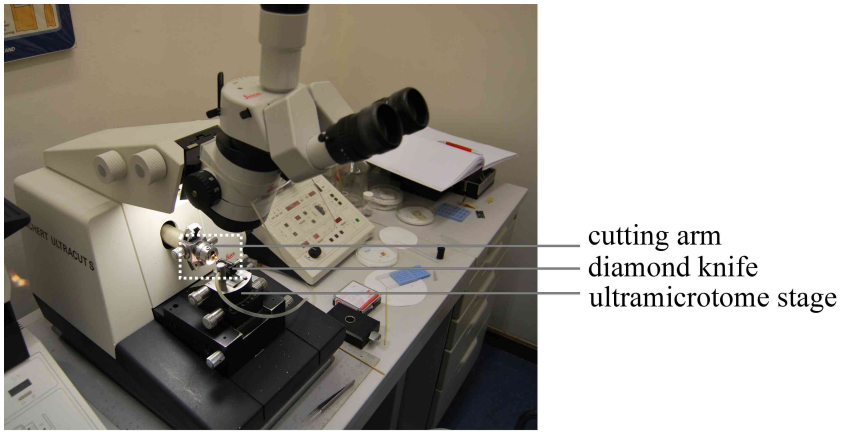

(a)

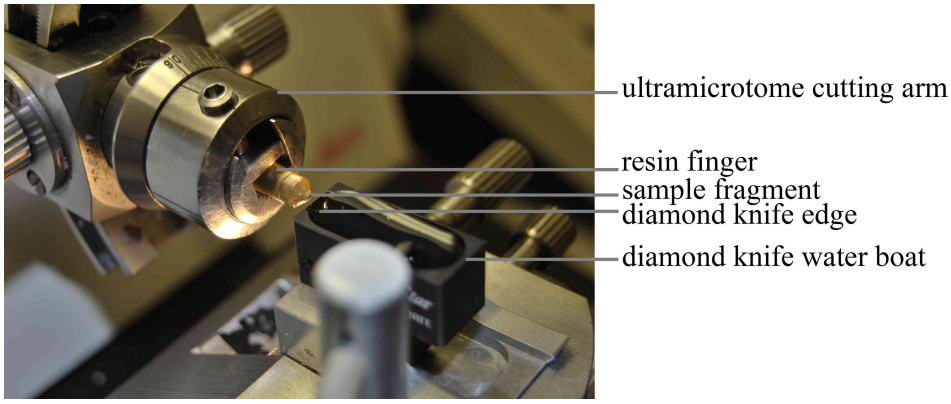

(b)

Figure 3.3: **(a)** The ultramicrotome used for cutting crystals into thin slices. The area framed by the white dashed box is enlarged at the bottom. **(b)** Zoom-in showing the cutting arm with the mounted sample on a resin finger as well as the diamond knife with its water filled boat.

As discussed in Chapter 2 we would like to investigate the structural changes during the metal-insulator phase transition of the $Cu(DCNQI)_2$ salt. These occur predominantly along the c-axis of the crystal. The needle-like crystals are therefore cut length-wise (parallel to the c-axis).

Initially the needles are placed under a microscope with top illumination in order to select a crystal with the least imperfections, i.e. a smooth, reflecting surface and well defined facets. A short piece of $\sim$2 mm is broken off (breaking it perpendicular to the crystal's c-axis) and placed onto filter paper. Since the crystals have a square basal face [13], a flat facet will be facing upwards when the needle piece is lying flat on the filter paper. This needle fragment will then be glued onto the

tip of an epoxy resin finger (produced from the SPURR Resin Embedding Kit manufactured by TAAB, catalogue S024/D). In preparation, the tip of the resin is first filed down to flatten the surface. A thin film of superglue (a commercially available cyanoacrylate adhesive) is put onto this flat resin tip which is subsequently pressed gently onto the crystal fragment lying flat on the filter paper. In this way one of the *a*-*c* facets is facing upward, away from the resin tip surface parallel to it (see Figure 3.4 (b)). An alternative to gluing the sample onto the resin finger is embedding it in the resin. We have, however, found that the quality of the cut samples is not improved by embedding. Photographs of a crystal piece glued onto a resin finger are shown in Figure 3.4. The needle fragment is about 2 mm long and about 80 μm thick and wide.

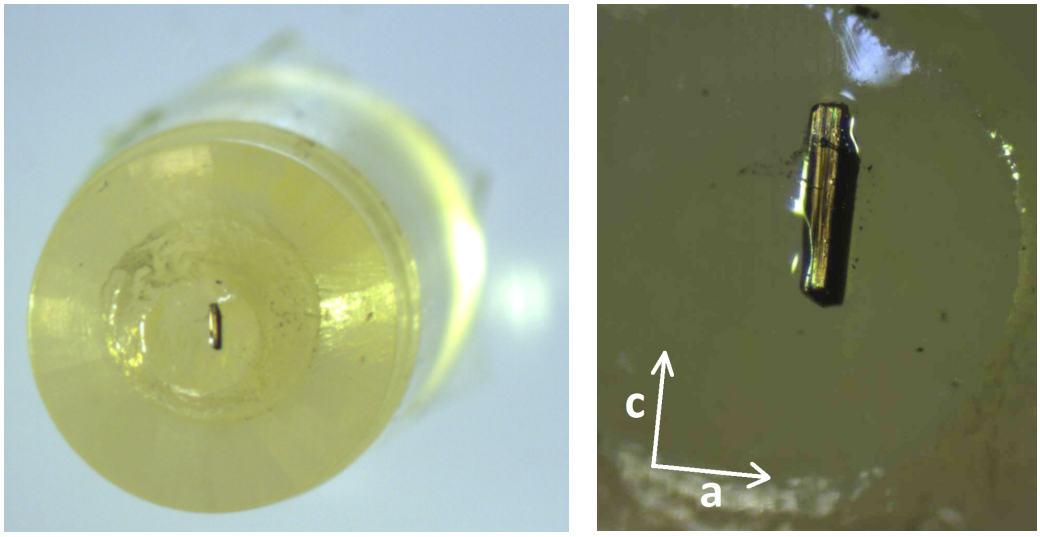

(a) **(b)**

Figure 3.4: **(a)** $Cu(DCNQI)_2$ crystal fragment (which is about 2 mm long and 80 μm thick) glued onto the tip of a resin finger. **(b)** Zoom-in of the crystal fragment showing the crystal facets (with one *a*-*c* facet facing upward). The white arrows indicate the directions of the lattice vectors **a** and **c**.

At the ultramicrotome the sample-resin unit is first mounted to be trimmed. The round area of the untrimmed resin tip is relatively large (about 5 mm in diameter) compared to the actual sample (about 2×0.08 mm^2). Also the round edge of the resin's tip provides a narrow point and thus exerts more pressure on the knife edge during cutting. The resin finger with the sample is mounted on the ultramicrotome stage (where the knife will later be mounted during cutting). Optimal light, view through the microscope, as well as good access for trimming are ensured in this position.

Trimming is done by hand with a razor blade. The resin is trimmed away such that the sample remains on a trapeze-shaped plateau of resin. This can be seen in Figure 3.5. The sample itself remains untouched during the trimming process.

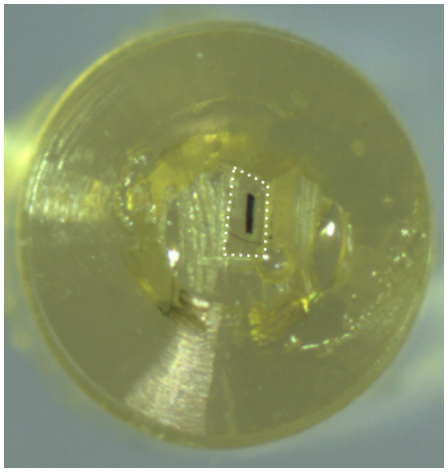

Figure 3.5: Sample on a trimmed resin finger. The white dashed trapezium indicates the resin plateau trimmed around the sample. The crystal fragment is about 2 mm long and 80 μm thick.

Now the sample-on-resin unit is ready to be mounted into the cutting arm of the ultramicrotome. Once the resin finger has been secured in this mount, a glass knife is mounted onto the stage. Initial cutting is usually done with a glass knife, since these are inexpensive and easily made. The glass knife's edge and the sample are ideally aligned in all three planes ensuring that the crystal facet is parallel with the knife edge. We have found that aligning the crystal length-wise with the knife-edge (i.e. the long crystal edge parallel to the knife-edge) yields the best cut samples. Adjusting the light and using reflections and shadows of the knife edge on the sample surface, this alignment is incrementally and iteratively optimised while moving the knife and the sample closer to each other. The crystal fragment is already glued onto the resin in such a way as to make the alignment in the ultramicrotome easier (as described above, care is taken to ensure a flat crystal facet facing upwards, as parallel as possible to the resin surface it is glued onto). Ideally the knife is aligned in such a way that it is parallel to the *a*-*c* facet facing it. This ensures that the crystal is "cleaved" in this plane, preparing the sample optimally for electron diffraction experiments (in which the sample-angle is not adjusted in the electron beam). As soon as the alignment is satisfactory the boat attached to the knife is filled with water until the water level has a slightly concave meniscus. Thereafter the cutting process can be started and automated.

During cutting the ultramicrotome's arm, into which the resin with the sample is mounted, moves in the following manner: On the down stroke the arm moves forward by a fixed distance (i.e. the desired thickness to be cut off the crystal) thus cutting off a slice of sample. During the upward motion the arm retracts, moving far enough away from the knife to ensure that it does not touch the knife again. Usually the downward/cutting motion is much slower than the retracting upward motion of the arm. This ensures controlled cleaving of the crystal and minimum impact on the narrow knife edge. The knife itself remains stationary during the cutting process. Only the sample is being moved. As a slice is being cut, it slides into the boat behind the knife's edge and floats on top of the water surface (due to the high surface tension). When the next sample slice is cut it gently pushes the previous slice further into the boat, along the water surface. In this manner a "train" of sample slices (with resin boundaries) is formed on top of the water. Once the surface of the crystal on the resin finger is smooth and uniform, the glass knife can be exchanged for the diamond knife. We use a MicroStar diamond knife with the following specifications for cutting: 35° or 45° included angle (between the facets forming the diamond edge – the smaller the included angle, the less morphological deformation of the sample, but the more fragile the edge); 4.0 mm edge length, 4° clearance angle (between the back diamond facet and the "block face", which is the sample-resin surface facing the knife. Larger clearance angles put more stress on the edge thus decreasing its lifetime, smaller angles cause the knife rubbing against the sample causing smearing or chatter of the slices.) The cutting process is continued in the same way as with the glass knife. Because the diamond knife is much harder, its edge remains sharper for longer than the glass knife's. Thinner sample slices can therefore be cut more accurately.

Several cutting parameters can be adjusted on the ultramicrotome in order to obtain optimal crystal slices: Cutting speed, retraction speed, cutting thickness, as well as sample angles relative to the knife edge. We have found that the slower the cutting speed the better the slices. A speed of 0.3 mm s^{-1} seems to be a good middle ground between time-efficiency and sample quality. We have also experimented with different floating solutes (replacing the water with ethanol, glycerine, as well as detergent solutions). Sample quality was not improved by any of these substitutes. On the contrary, several adverse effects were found: decreased ability of samples to float on the surface of the solute (as expected for fluids with a lower surface tension than water); also dissolving of the epoxy fixing the boat to the knife. Therefore, so far water remains the best liquid to be used for floating the samples.

Once enough slices float on the water surface they are transferred onto a standard TEM mesh (a thin round grid, of diameter 3.05 mm). There are two ways of doing so which we found to work very well:

The first method entails using fine tweezers to pick up a single TEM mesh. The mesh is carefully dipped onto the water surface (in the knife-boat) on both sides to wet it before submerging it vertically. Submerging it vertically (i.e. edge-wise) decreases the chance of bending the thin copper mesh due to the surface tension. One then slowly moves the mesh horizontally underneath the sample slices floating on the water. Moving the mesh slowly is essential as not to disturb the surface with the floating sample. Once the mesh is underneath a group of floating slices, it is carefully lifted up, keeping the mesh horizontal. Ideally a drop with the desired samples on its surface will stick to the TEM mesh once it is completely lifted out of the water. Carefully touching the edge of the mesh to filter paper removes the water droplet, leaving the sample slices stuck to the grid.

Alternatively one can make use of a "perfect loop" (Perfekt-Kescher (R), T5112, Plano) to pick up the sample from the water surface. The perfect loop consists of a thin (∼0.05 mm thick) metal ring, which has a slightly smaller diameter (inner diameter ∼2 mm, outer diameter ∼2.8 mm) than a standard TEM mesh (diameter 3.05 mm). This loop is mounted on a stick-like holder for easy manipulation. One approaches the floating sample slices with the loop held horizontally directly from above. Touching down with the ring on the water surface surrounding the slices to be picked up makes a water droplet with the sample on the surface attach to the loop. A TEM mesh lies ready on a piece of filter paper. The loop is pressed down with its ring aligned with the mesh's edges. Small holes in the frame of the loop (∼0.5 mm diameter) allow for the water to be absorbed into the filter paper. The sample stays behind on the TEM mesh.

Both methods leave equally good sample slices on the TEM mesh. After leaving the mesh with the sample to dry for a few minutes it can be stored in a standard mesh holder.

We have found standard copper 300 mesh grids (with a hole size of ∼63 μm) to generally work the best for initial sample preparation and characterisation. In case of bigger sample slices, 200 mesh grids (∼97 μm hole size) can be used without losing the sample due to water surface tension or samples falling through the grid holes. Carbon coated copper meshes (∼10 nm thick carbon film) were also used to collect samples.

Before mounting the meshes with the sample, each is observed under the light microscope. The samples are sorted according to quality. The more uniform and less brittle the thin crystal slices appear the more single crystalline they are and better resolved diffraction spots are expected. Photos are taken of the samples on the meshes to help identify and locate the best sample spots during mounting. An example of a uniform, single crystal slice on a copper TEM mesh is shown in Figure 3.6.

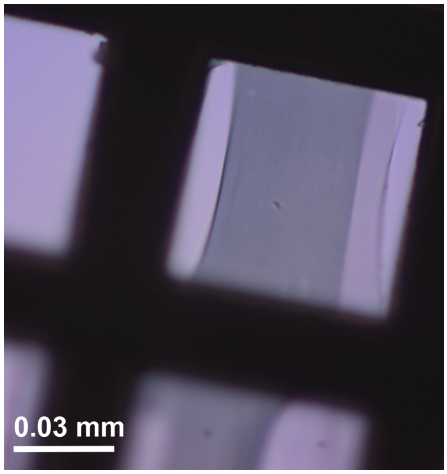

Figure 3.6: A homogeneuos, single crystalline sample slice of 25 nm thickness on a standard 300 copper TEM mesh as viewed under the light microscope. The mesh holes are ∼63 μm wide.

The final step is to glue the meshes with the thin samples onto a sample mount. The mount is typically a copper plate with a few holes which are slightly smaller than a mesh's diameter (i.e. 2 mm – 2.5 mm diameter). With vacuum compatible silver paint, $\sim$ 100 μm diameter apertures are glued over the mount holes such that an aperture is positioned centrally over one of the sample mount holes. Using the photos taken previously the best sample on a mesh is identified – covering one or more mesh holes uniformly. This spot is then aligned with the aperture and the grid is glued onto the edge of the aperture using silver paint leaving the sample untouched (see Figure 3.7). Figure 3.7 shows the sample and aperture glued onto the sample mount. With this technique only the uniform, single-crystalline sample will be exposed to the electron beam, which is about 200 μm in diameter (see Section 2.3) in the diffraction experiment. The aperture thus aids in decreasing the background signal in the diffraction images caused by other (less than optimal quality) samples and the remain-

ing grid. This decrease in background signal counter balances the compromise made on the number of electrons used for diffraction: Of the 200 μm diameter electron beam at the sample only a 100 μm diameter beam passes through to the detector. This decreases the brightness of the electron diffraction pattern. If, however, the background signal is decreased the diffraction spots are clearly visible.

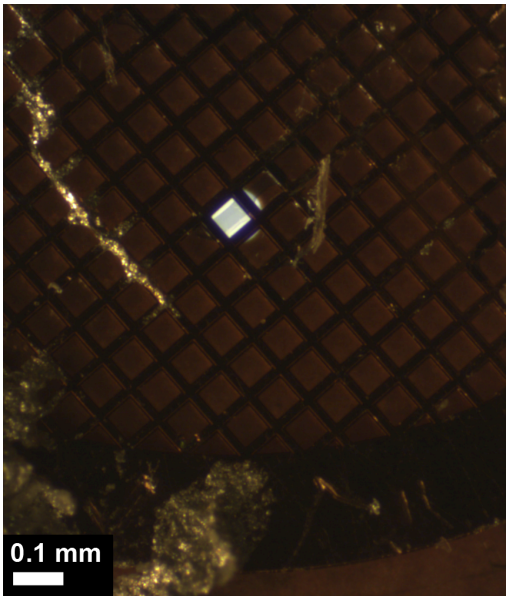

Figure 3.7: Aperture and sample-holding mesh glued onto the sample mount with silver paint.

Finding the desired sample spot on the mesh inside the vacuum chamber is also easier with the aperture in place. The sample mount is aligned in such a way that the electron beam passes through the aperture optimally.

The sample mount is thermally coupled to the cryostat via a copper braiding. The cryostat's second temperature sensor is connected to the sample mount in order to monitor the sample temperature as closely as possible. Using a Teflon rod the mount is fixed to a set of translation stages. It is thus thermally decoupled from the rest of the setup. The stages enable adjustment and optimisation of the sample position in the x, y, and z directions inside the chamber. Once the sample is optimally aligned in the electron beam inside the vacuum chamber, electron diffraction images can be recorded. Procedures of data collection and analysis as well as results are discussed in Chapter 4.

3.4 Absorption spectrum

Before the sample is investigated in the ultrafast electron diffraction setup, two other methods of initial characterisation of the $Cu(DCNQI)_2$ crystals were employed.

The first measurement was a white light absorption spectrum of a slice of the partially deuterated copper salt: A ground state room temperature white light transmission measurement was done on a 100 nm thick crystal of d_6 $Cu(DCNQI)_2$ in the ultrafast spectroscopy setup in our laboratory. The setup is described in detail in Reference [14]. White light created by non-linear effects in a sapphire crystal pumped by a femtosecond laser is passed through the sample slice on a TEM mesh. The transmitted intensity (I) was measured by a spectrometer. For the reference spectrum (I_0) the white light is passed through an empty TEM mesh. Three sets of reference and sample transmission spectra are collected and averaged to obtain the data from which the ground state absorption spectrum in Figure 3.8 was calculated.

Using the Beer-Lambert law, the transmission data is converted to absorbance values:

$$T = \frac{I}{I_0} = e^{-\alpha l} \tag{3.1}$$

where T is transmission, I is the transmitted intensity through the sample, I_0 is the reference intensity transmitted through the empty TEM mesh, α is the attenuation coefficient in units of inverse length, and l is the thickness of the sample which was 100 nm for this measurement. From this the absorbance (A) can be calculated as follows:

$$A = -\ln(\frac{I}{I_0}) = \alpha l. \tag{3.2}$$

For the graph in Figure 3.8 the absorbance per centimetre, i.e. the attenuation coefficient α in cm^{-1}, is plotted as a function of wavelength.

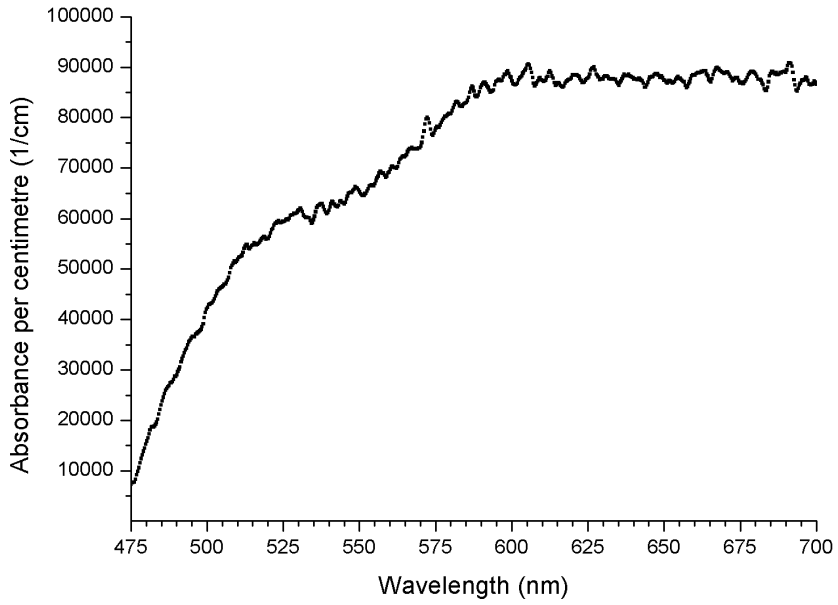

Figure 3.8: Absorption profile of a 100 nm thick slice of a single $Cu(DCNQI)_2$ crystal. This measurement was performed in the white light absorption setup described in Reference [14]. The wavelength window from 475 nm to 700 nm is a part of the white light continuum produced by non-linear effects in a femtosecond laser pumped sapphire crystal.

This measurement of the radical anion copper salt of DCNQI has a similar profile to the spectrum of the $DCNQI^-$ anion reported by Karutz *et al.* [9] as seen in Figure 3.9. The absorbance increases steadily from 475 nm to about 600 nm. Between 600 nm and 700 nm the absorbance curve plateaus in our measurement, while showing more oscillatory structure for the anion in solution. The similar absorption profiles of the $Cu(DCNQI)_2$ crystal and the organic anion in solution indicate that the absorption profile of the crystal is dominated by the organic anion rather than the copper cations.

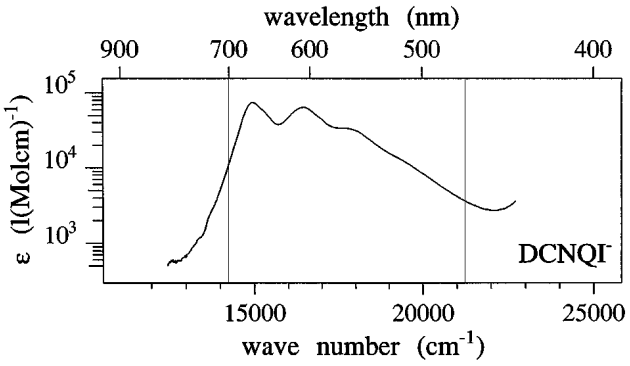

Figure 3.9: The molecular extinction, ε, as a function of incident light wavelength of the DCNQI$^-$ anion in CH_3CN solution at room temperature as reported in [9]. The vertical lines at 475 nm and 700 nm indicate the wavelength range plotted for the Cu(DCNQI)$_2$ crystal in Figure 3.8. Figure adapted from [9].

From our measured spectrum in Figure 3.8 the optical penetration depth, δ_p, at different wavelengths were determined. The penetration depth is taken as the length l of the sample (see Equations 3.1, 3.2) for which the transmitted light intensity drops to a value $\frac{1}{e}$, which corresponds to the inverse of the attenuation coefficient, i.e. $\delta_p = \frac{1}{\alpha}$. Between 600 nm and 700 nm the sample has an attenuation coefficient of $\alpha \sim 90\ 000\ \text{cm}^{-1}$ which corresponds to $\delta_p = 111$ nm $\pm$ 3 %. The error of 3 % was calculated from the data for this wavelength range. The absorption spectrum of the DCNQI anion in Figure 3.9 [9] shows a decrease in the molar extinction coefficient, i.e. a decrease in absorption, for wavelengths longer than 700 nm. As mentioned before, the spectra of the anion in solution and the copper salt have similar profiles and therefore Cu(DCNQI)$_2$'s absorption is believed to be dominated by the DCNQI molecule. With this assumption the absorption of the copper salt should also decrease at wavelengths above 700 nm, and thus the penetration depth is longer in that spectral range including our fundamental laser wavelength, 775 nm. Karutz *et al.* [9] calculated the optical penetration depth into a bulk sample to be 100 nm at a wavelength of 533 nm. From our measurement with a 100 nm thin crystal slice, the optical penetration depth at 533 nm was calculated to be 167 nm $\pm$ 2 % which confirms the order of magnitude of the 100 nm measured by Karutz *et al.* [9].

In order to determine whether the sample is homogeneously excited by the laser pump beam the absorption as well as the reflection and the interference between the absorbed and reflected light have to be taken into consideration. The total intensity of the light travelling through the crystal depends on all three factors. In the 600 nm – 700 nm range a 30 nm thick sample would

absorb 27 % ± 3 %, i.e. the intensity profile of the light inside the crystal would decrease by about 27 % from the front to the back of the 30 nm thick crystal. The reflection could not be measured, because the thin sample was too wavy, thus scattering the reflected light. However, as demonstrated by Haupt [50], the intensity profile of the light reflected off the back surface of the crystal and the interference intensity profile counterbalance the absorption intensity profile inside the crystal leading to a nearly homogeneous total light intensity profile inside the crystal [50]. A 30 nm thick sample is therefore homogeneously excited by the laser pump beam in our UED system.

The white light absorption measurement thus gave us an indication of the optical penetration depth of the laser light into our sample. With this information we are confident that a $Cu(DCNQI)_2$ crystal slice of 30 nm thickness will be uniformly excited by the laser light wavelength of 775 nm.

3.5 Preparation diagnostics and initial sample characterisation using a TEM

The sample was also investigated at the transmission electron microscope (TEM) at the University of Cape Town. The TEM had the following specifications: FEI Tecnai 20 transmission electron microscope, operating at 200 kV (Lab6 emitter), fitted with a Tridiem energy filter, Gatan CCD camera.

The electrons of the TEM have an energy of 200 keV which corresponds to a de Broglie wavelength of 2.5 pm. This is about a third of the UED setup's wavelength (7 pm) enabling observation of smaller objects providing real space images as well as diffraction patterns of the sample. With the TEM's resolution limit of about 2 Å, samples a few tens of nanometre in size can be investigated, in contrast to the sample diameter of ∼100 μm needed in the UED setup (see Section 2.3). This has the advantage that bright, well resolved images and diffraction patterns can be obtained in the TEM even of small samples. For this reason the TEM was used as an initial diagnostic tool to investigate sample micro-structure in real space images which could not be resolved by the light microscope. With this, the sample quality as well as the efficiency of the ultramicrotoming procedure could be gauged in terms of producing intact, single crystalline slices.

The TEM as diagnostic tool

The figures presented in this section outline the insight gained by high resolution real space TEM images about the sample slice quality and the efficiency of the sample preparation procedures during ultramicrotoming.

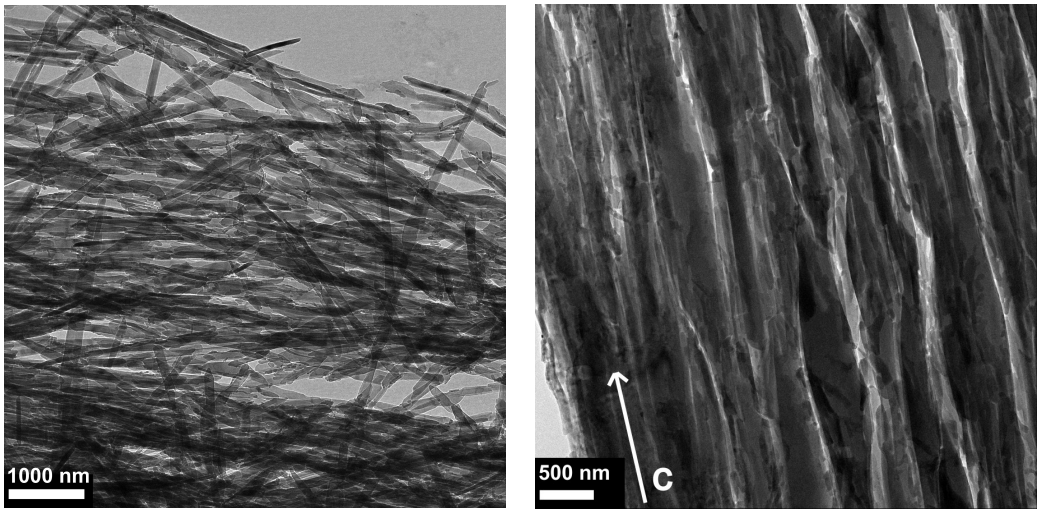

(a) **(b)**

Figure 3.10: (**a**) Polycrystalline sample slice. (**b**) Chatter in a sample. The white arrow indicates the orientation of the crystal's *c*-axis.

Figures 3.10a and 3.10b are an indication of the importance of knife alignment during ultramicrotoming. In Figure 3.10a small, randomly arranged crystals are visible. This sample would not yield a diffraction image with single, discernible diffraction spots, but rather an image resembling powder diffraction, with rings rather than spots. The needle-like crystal broke up into smaller crystals during cutting. Similar observations were made while preparing the sample for gluing onto the resin finger: the bulk needle split into finer needles while manipulating it with fine tweezers. For some sample batches this effect was more pronounced than for others, suggesting differences during sample synthesis between batches, e.g. growth speed or contaminants. Brittle crystal batches were avoided for future sample preparation. Knife edge alignment perpendicular to the needle's *c*-axis also yielded polycrystalline sample slices. Parallel alignment of knife edge and needle *c*-axis was therefore implemented yielding homogeneous slices like in Figure 3.12. In Figure 3.10b the cutting motion was perpendicular to the *c*-axis, i.e. the knife edge was aligned parallel to the *c*-axis. The sample has alternating smeared out (light grey) and compressed (dark grey) stripes parallel to the knife edge. This phenomenon is known as chatter. The microcrystals are more aligned in this image – all lying parallel to the *c*-axis – than in Figure (a). As mentioned in Section 3.3 chatter can result from the knife rubbing against the sample during cutting due to a too small clearance angle. Appropriate adjustments were subsequently made during ultramicrotoming to improve sample quality.

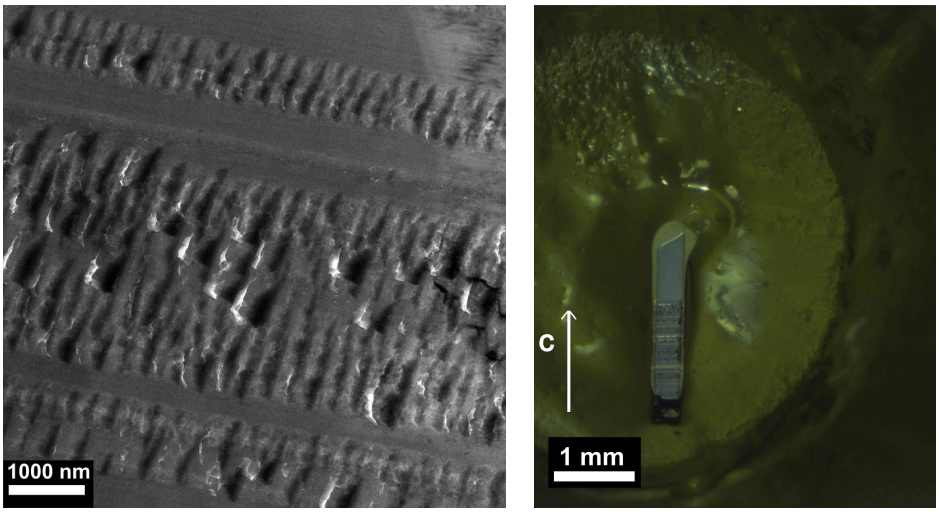

(a) **(b)**

Figure 3.11: (**a**) Resin slice cut with the diamond knife. (**b**) Photograph taken through a light microscope of a needle fragment on resin after ultramicrotoming. The crystal's *c*-axis orientation is indicated by the white arrow.

The importance of knife sharpness is demonstrated in the images on Figures 3.11a and 3.11b. In Figure 3.11a the cutting direction was horizontally across the page in this image. The horizontal traces are an indication of irregularities in the knife edge. Smooth horizontal traces may imply sharp parts of the knife edge, while the rough traces most probably correspond to blunt or chipped parts of the edge. The knife-edge quality could thus be monitored for indications when it should be sharpened. The vertical lines indicate chatter as described in Figure 3.10b. In Figure 3.11b the cutting direction was perpendicular to this *c*-axis. The top half of the needle surface is smooth while the bottom part displays similar traces as seen in Figure (a) on a larger scale, confirming the poor quality of the knife edge in this part. Knife edge maintenance proved to be of utmost importance, because homogeneous single crystalline samples as seen in Figure 3.12 are only produced by ultramicrotoming with a sharp, smooth diamond knife.

A micrograph of an ideal sample in shown in Figure 3.12. The *c*-axis orientation of the crystal is indicated by the white arrow. Microcrystals which are uniformly aligned parallel to the *c*-axis and about 500 nm long can be seen for the entire area imaged here. At the bottom left there are darker, less uniformly coloured patches of microcrystals. The darker areas are thicker, i.e. allowing fewer

electrons to penetrate. The top homogeneously coloured light grey part of the image is uniformly thick. The area indicated by the dashed rectangle is the area which was magnified for the real space image in Figure 3.13 and the electron diffraction image in Figure 3.14.

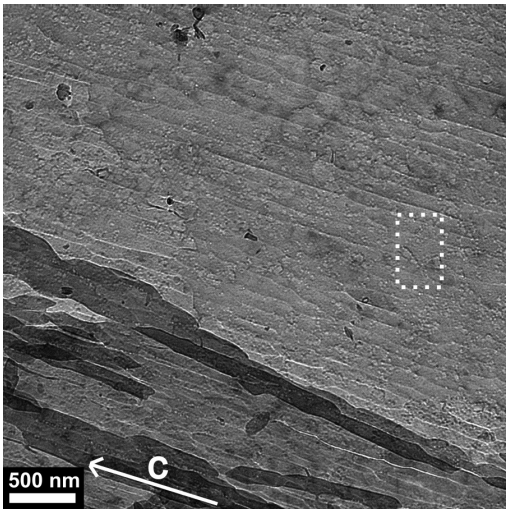

Figure 3.12: Homogeneous 25 nm thick d_6 Cu(DCNQI)$_2$ sample.

The TEM was a useful tool to check sample quality and improve on our ultramicrotoming technique. In this way homogeneous sample slices as in Figure 3.12 are now produced reliably from single crystalline crystal needles.

Initial sample characterisation in the TEM

The TEM can be operated in imaging as well as in diffraction mode and thus the following real space and diffraction images were taken of a single crystalline, homogeneously thick sample area as indicated in the dashed rectangle in Figure 3.12. These images could be used for initial characterisation of the Cu(DCNQI)$_2$ sample slices.

Firstly, a further magnified real space image was taken of the homogeneous, single crystalline sample. This is displayed in Figure 3.13. The horizontal alternating light and dark stripes in the micrograph in Figure 3.13(a) seem to be the DCNQI molecules stacked along the c-axis to make up the crystal (compare to Figure 2.2). The plot of these stripes – Figure 3.13(b) – allowed the measurement of the periodicity of the observed wave-like ripple structure. The distance between

the peaks was found to be ∼0.384 nm. This matches the lattice constant along the c-axis of d_6 Cu(DCNQI)$_2$ at room temperature, as summarised in Table 2.1[15], to within <2 %. This matching c lattice constant supports the idea that the horizontal lines in the real space micrograph on the left are indeed the DCNQI molecular stacks.

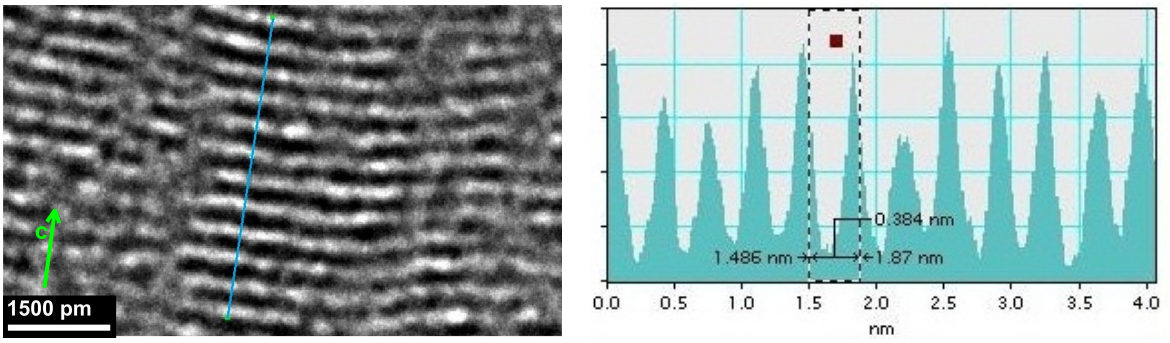

(a) **(b)**

Figure 3.13: **(a)** Real space image of the uniform light grey sample area inside the white dashed rectangle indicated in Figure 3.12. The orientation of the crystal's c-axis is indicated by the green arrow on the left hand side. **(b)** A plot of the transmitted electron intensity along the blue line indicated in the image on the left.

The TEM was operated in diffraction mode to obtain the well resolved electron diffraction image of the uniform crystal in Figure 3.14. The original diffraction image was rotated by 9.75° for the analysis described in Chapter 4. The undiffracted direct beam is blocked by a beam block in order to prevent image saturation by this peak. The horizontal red line marks the zero order line of Bragg peaks. The vertical red line shows the central line of symmetry of the diffraction image. The directions and relative magnitudes of the reciprocal lattice vectors $\mathbf{a}^*$ and $\mathbf{c}^*$ are indicated by the green arrows at the bottom left, where $|\mathbf{a}^*| = \frac{1}{a} = \frac{1}{2.1619\ \text{nm}}$ and $|\mathbf{c}^*| = \frac{1}{c} = \frac{1}{0.3874\ \text{nm}}$ [15]. The part of the first order line of diffraction peaks which was used for analysis in Chapter 4 is indicated by the green rectangle.

The electron diffraction image in Figure 3.14 displays a comparable peak distribution to the room temperature x-ray diffraction image of a similar copper salt in Figure 2.7 [6]: Lines of diffraction peaks are formed. The peaks are also well defined (and not smeared out), indicating that the image was formed with the electron beam perpendicular to the a-c plane of the crystal (as was prepared for during cutting (see Section 3.3)).

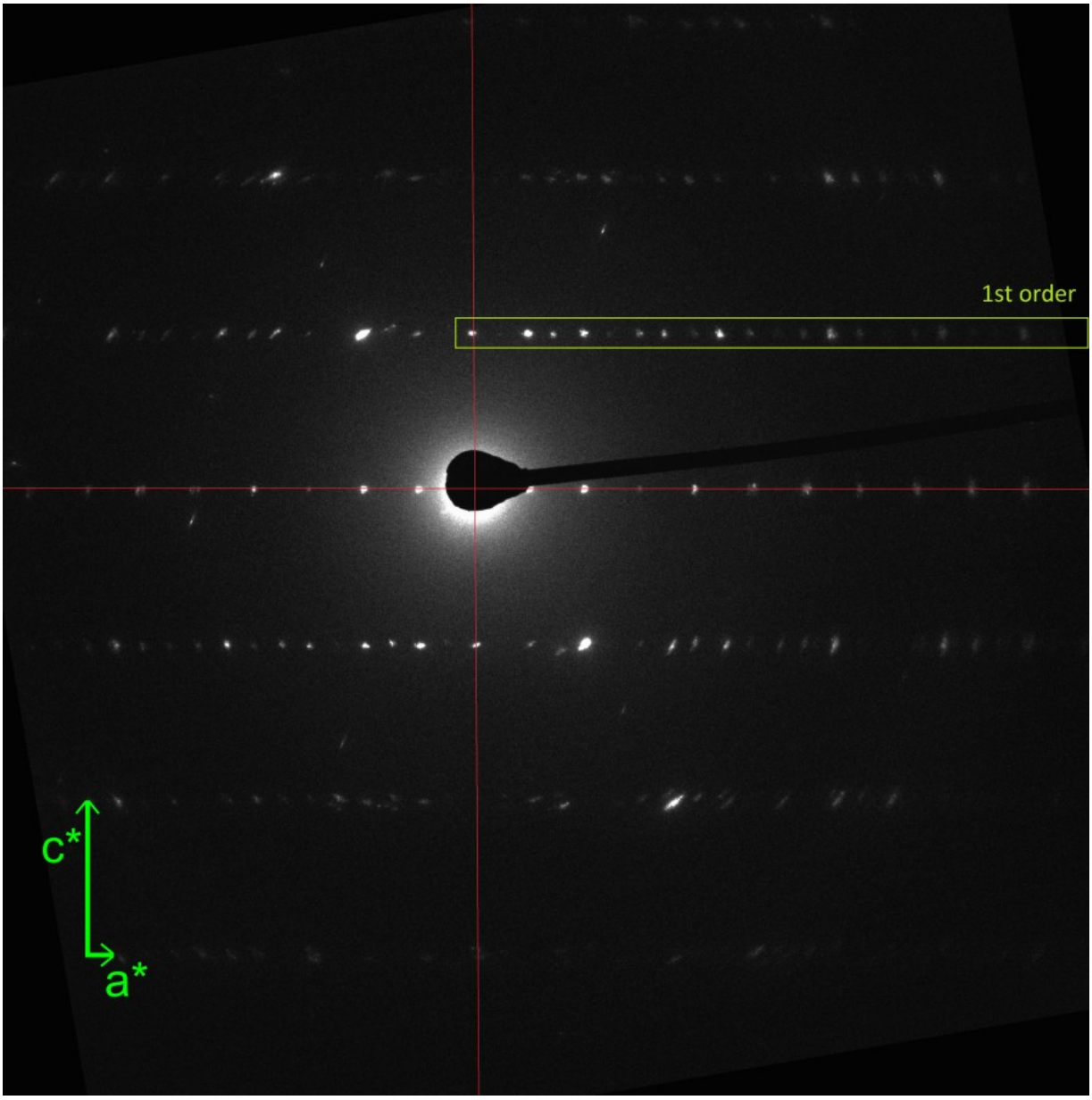

Figure 3.14: Room temperature TEM diffraction image of the 25 nm thick d_6 Cu(DCNQI)$_2$ crystal – the corresponding real space sample area is inside the white dashed rectangle indicated in Figure 3.12.

As outlined in Section 2.2 the diffraction pattern displays a part of the reciprocal lattice of the crystal. In reciprocal space $\frac{1}{c} = c^* > a^* = \frac{1}{a}$. The large distances between the lines of diffraction spots therefore correspond to the molecular stacking distance (c) in the crystal lattice. With the TEM software, c^* was measured on the diffraction pattern. Subsequently c was calculated to be 3.78 Å (which corresponds to the value recorded in Table 2.1 to within 2.4 %). The TEM diffraction measurement therefore confirmed that our sample's crystalline structure corresponds to the previous reports (as did the conductivity measurements described in Section 3.2 and the absorption measurements in Section 3.4).

Comparison between the TEM and the UED setup

The transverse coherence length ($L_\perp$) of the TEM setup was roughly determined from the diffraction image following the calculation outlined in Section 2.3. $L_\perp$ was calculated in both the $\mathbf{a}^*$- and the $\mathbf{c}^*$-axes. It was found to be in the order of 75 Å which is roughly in the same order as the UED setup's transverse coherence length (100 Å). This value could unfortunately not be validated and compared to a theoretical transverse coherence length of the TEM. Therefore, judging from the coherence length calculated from the diffraction patterns so far obtained with the two systems, diffraction images of similar resolution are achievable in both TEM and UED setup of the crystalline lattice of $Cu(DCNQI)_2$ (as explained in Section 2.3).

As mentioned before, due to the difference in electron energy in the two systems (TEM = 200 keV; UED = 30 keV), different de Broglie wavelengths are achieved (TEM = 2.5 pm; UED = 7 pm). The TEM therefore has the potential to resolve structures which are almost a third of the size resolvable with the UED electron beam. The molecular crystal lattice distances of $Cu(DCNQI)_2$ are in the order of a few tens of nanometres, i.e. about four orders of magnitude larger than the wavelength of either of the systems. For the investigation of this organic molecular salt both setups will thus provide a suitable resolution for analysable diffraction images.

The TEM has highly sophisticated electron optics which enable it to produce high resolution real space images in addition to diffraction images. In the UED setup well resolved diffraction images (see Chapter 4) can be produced, but without any electron optics for image formation, only poorly resolved real space shadow images can be formed on the detector screen. Therefore the TEM is a great diagnostic tool for evaluating samples and thus also indirectly cutting procedure quality in real space, which cannot be performed in the UED setup.

Sample dimensions with diameters down to 0.2 nm and up to 100 nm thickness can be investigated in the TEM. The UED setup requires sample diameters of about 100 μm and about 30 nm thickness. In order to obtain diffraction patterns of microcrystals, the TEM would be required. The Cu(DCNQI)$_2$ crystals can, however, be ultramicrotomed to meet the UED setup requirements. Concerning dimensions, the sample's diffraction images can therefore also be investigated with UED.

Fine angle adjustments of the sample relative to the electron beam of up to 70° are possible in TEM in two planes. The UED setup does not currently allow angular sample adjustment. DCNQI crystals have to be carefully prepared before and during ultramicrotoming in order to cleave them along the desired plane. Due to the square facets of the crystal needles this is achievable (see Section 3.3). The sample slice can then be investigated in the TEM in order to verify that the sample was cleaved parallel to the desired plane (i.e. the a - c plane (see Section 3.3)). Again the TEM can aid as a diagnostic tool to verify accurate (and improve on suboptimal) sample preparation. Once the sample preparation is performed precisely no further angle adjustment is required in the UED setup.

The TEM emits 100 – 2000 electrons per square nanometre (corresponding to 10^8 – 2×10^9 electrons per square micrometer), which is about eight orders of magnitude more than the UED's electron flux of 30 electrons per square micrometre. The large number of incident electrons per unit area allows for bright electron diffraction patterns for short exposure times. The TEM diffraction image in Figure 3.14 was taken with a few seconds exposure time. Images of similar brightness (see Figure 4.1) can be achieved in the UED setup by implementing longer exposure times in the order of a minute. The TEM's electron flux translates to 16×10^{-12} C μm^{-2} – 3.2×10^{-10} C μm^{-2}. This amount of charge per area is of the same order as the destruction of crystallinity threshold for pentacene (3.5×10^{-10} C μm^{-2} at 5 kV [51]) (see also Section 2.3). The DCNQI sample slices investigated in the TEM were damaged due to electron radiation during measurements. This process could be observed during high resolution imaging as well as during diffraction measurements. The diffraction spots disappeared after just a few seconds exposure to the high energy electrons, while crystalline structures in real space became blurry in the same amount of time. Regarding electron flux, UED is therefore more suitable for the organic molecular salts in terms of preventing sample damage, consequently allowing long exposure times to achieve bright diffraction images.

The TEM sample mount is cooled with liquid nitrogen, reaching temperatures of ~80 K. This implies that only the metallic state of the d_6 copper salt (T_{MI_1} ~70 K) can be observed. In the UED

setup, however, the cryostat allows temperature control spanning 30 K – 400 K (see Section 2.3) allowing temperature controlled investigation of the metal-insulator phase transition of the DCNQI-salt as well. Therefore the UED setup is favoured over the TEM we used, for temperature controlled investigation of the sample's diffraction pattern.

The TEM's electron beam is a continuous (cw) beam, while the UED utilises pulsed electron beams. The pulsed (1 kHz) electron beam, together with the possibility of exciting the sample with a pulsed laser beam and being able to delay the two pulses in a controlled manner (see Section 2.3) allows the temporal resolution of ultrafast dynamic transition processes in the UED setup. Because the TEM only has one cw beam, neither excitation of the sample, nor the temporal resolution of ultrafast processes are possible in this system. For investigation of ultrafast structural changes, the UED setup is therefore ideal.

In summary: The TEM is an ideal diagnostic tool to optimise sample preparation and therefore sample quality. After this initial characterisation the sample can be introduced into the UED setup in order to investigate its structure in stationary phases at different temperatures, as well as temporally resolving laser induced ultrafast phase transition behaviour.

In this Chapter the electrolytic synthesis of $Cu(DCNQI)_2$ crystals was outlined. Sample preparation in terms of ultramicrotoming and mounting the sample in order to optimally prepare it for the UED experiment were described. Initial characterisation of the sample was performed verifying the sample's conductivity behaviour with respect to temperature, its room temperature absorption spectrum, as well as confirming its crystalline structure in a TEM. All three techniques produced results corresponding well with findings reported previously by other groups. The sample was then introduced into the UED setup for further investigation.

CHAPTER 4
INTRODUCING THE ORGANIC MOLECULAR SALT INTO THE UED SETUP

In the UED setup electron diffraction images are recorded with the CCD camera (see Figure 2.15, Section 2.3). Taking an image with a 60 second exposure time adds diffraction information of 60 000 electron pulses in a single image – due to the 1 kHz repetition rate of the laser. This relatively long exposure time, compared to the few seconds long exposure time at the TEM, allows us to collect bright diffraction patterns while using only 1000 electrons per pulse. As discussed in Section 2.3 this low electron number minimises the effect of space-charge in our setup geometry thus ensuring short electron pulse durations in the order of 300 fs. The exposure time for one image should not exceed a few minutes in order to minimise possible disturbances in the experimental conditions, e.g. slow fluctuations in sample temperature, or laser intensity, during the recording of one image. When brighter images are required, several one minute exposure images with the same experimental conditions are added. Diffraction patterns with bright, unsaturated spots are recorded in this manner.

4.1 Room temperature electron diffraction

A thin slice of the $Cu(DCNQI)_2$ salt was successfully introduced into the vacuum chamber of the UED setup. Initial room temperature diffraction images of its metallic phase were recorded. Figure 4.1 shows a diffraction pattern of a 25 nm thick d_6 $Cu(DCNQI)_2$ sample recorded in the UED setup at room temperature.

For Figure 4.1 twenty-three images (of 60 s exposure each) were superimposed to create this figure. The original image was rotated by 62.5° to achieve horizontal alignment of diffraction peak lines (for analysis in the LabVIEW program (as described later in this section)). The direct undiffracted electron beam at the centre of the diffraction pattern is shielded by a beam block in order to prevent the diffraction image to be saturated by its intensity. The horizontal red line marks the zero order line of Bragg peaks. The vertical red line shows the central line of symmetry of the diffraction image. The directions and relative magnitudes of the reciprocal lattice vectors $\mathbf{a}^*$ and $\mathbf{c}^*$ are indicated by the green arrows at the bottom left, where $|\mathbf{a}^*| = \frac{1}{a} = \frac{1}{2.1619 \text{ nm}}$ and $|\mathbf{c}^*| = \frac{1}{c} = \frac{1}{0.3874 \text{ nm}}$ [15].

Rectangular boxes indicate the part of the first, second, and third order lines of diffraction peaks which are used for analysis. An uneven, slightly darker patch is noticeable directly above the beam block in this orientation of the image. This indicates a damaged area on the detector screen and is therefore not part of the diffraction pattern.

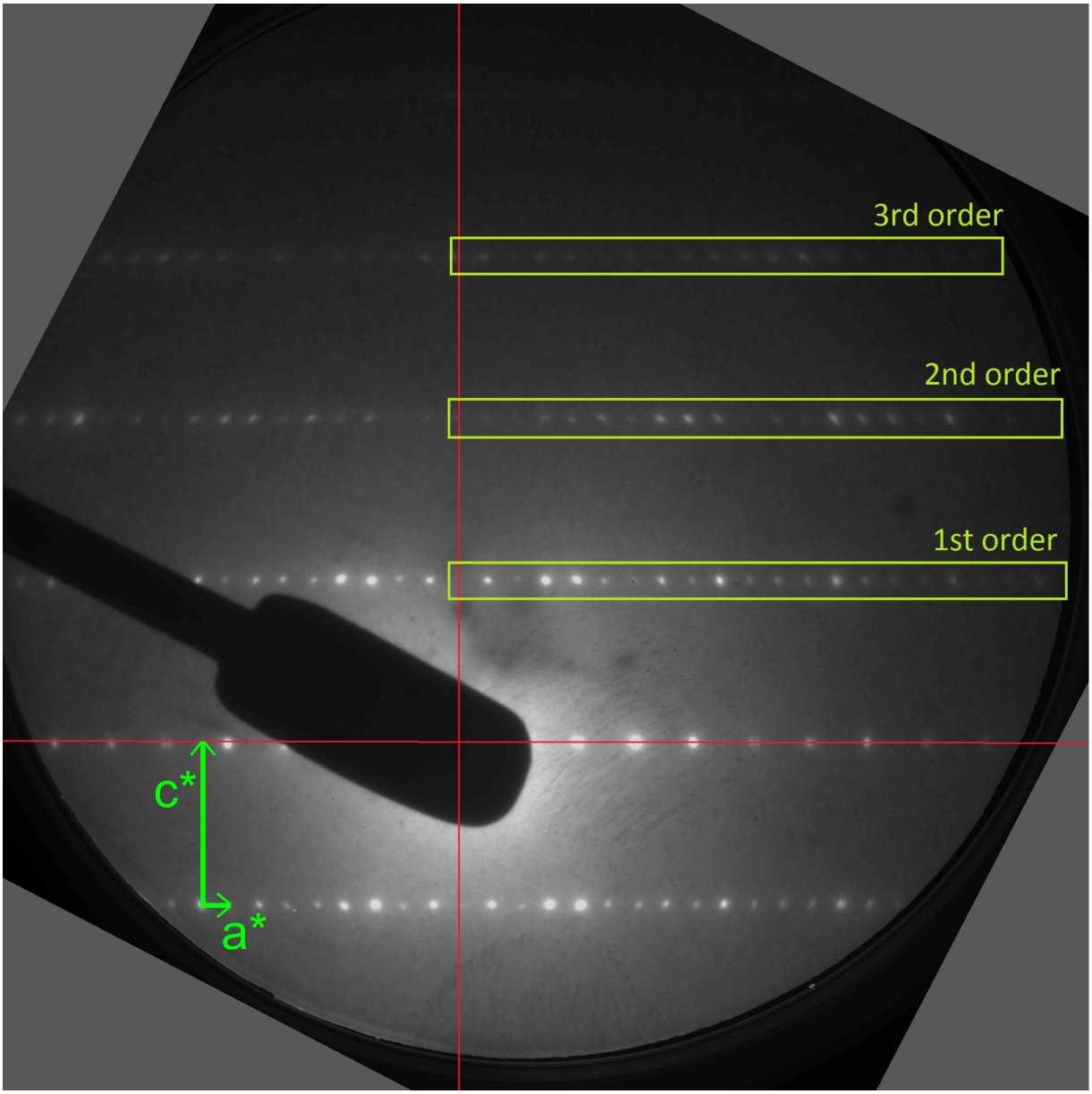

Figure 4.1: Room temperature electron diffraction image taken in the UED setup of a 25 nm thick crystal of d_6 Cu(DCNQI)$_2$.

Horizontal lines of diffraction spots can be seen in Figure 4.1 – as in the TEM diffraction image (Figure 3.14) and the x-ray diffraction image by H. Kobayashi *et al.* (1993) (Figure 2.7) [6]. The large vertical distances (c^*) between the lines of diffraction peaks in the part of the reciprocal lattice displayed in this image, are related to the molecular stacking distance, $c = \frac{1}{c^*}$, of the d_6 Cu(DCNQI)$_2$ needles, as described for the TEM diffraction image (Section 3.5). Similarly the short horizontal distance (a^*) between the diffraction peaks in one line corresponds to the distance between DCNQI stacks, $a = \frac{1}{a^*}$, in the crystal, as seen in the c-axis projection in Figure 2.2. Employing Equation 2.5 (from Section 2.2) the measured a^* and c^* reciprocal lattice distances in the UED diffraction image were used to calculate the corresponding crystal lattice spacings: $a = 22$ Å $\pm$ 2 Å, differing by <10 % from the literature value in Table 2.1, and $c = 4.0$ Å $\pm$ 0.4 Å, differing by ∼13 % from the value in Table 2.1 [15], which is in the same order of accuracy as the TEM result in Section 3.5.

The same complicated intensity distribution of the diffraction spots along the horizontal lines was obtained in all diffraction patterns of Cu(DCNQI)$_2$ samples cut in this orientation. For example, comparing the first order lines of diffraction peaks in the c^*-axis direction above and below the zero order line, marked by the horizontal red line: The peak intensity distribution, i.e. the position and brightness of the spots, is similar along both rows. It also is symmetric around the vertical red line. In order to confirm that this repeatable electron diffraction pattern corresponds to the Cu(DCNQI)$_2$ crystal lattice determined in previous experiments by other groups, simulated electron diffraction patterns were calculated.

Electron diffraction simulations are done by Olufemi Olaoye at Stellenbosch University with the "Simulations and Analysis of Electron Diffraction" program [56]. The program is based on the principle of selected area electron diffraction (SAED). SAED implies that the aperture selected sample area is illuminated by a parallel beam of electrons. In the UED setup the magnetic lens is situated about 1 cm – 2 cm in front of the sample, focussing the electron beam onto the detector screen behind the sample, over ∼40 cm. However, the beam area is about four times larger than the sample area during transmission, and the sample is situated at the centre of the electron beam. The electron beam can therefore be assumed to be approximately parallel when passing through the sample. The TEM also operates in SAED mode: The electron beam is collimated (plane wave) at the target and is focused after transmission onto the detector screen. The simulation parameter for SAED therefore corresponds with the experimental conditions. The simulation model also assumes

that the sample scatters the electron beam only weakly and therefore does not change the phase of the electron beam passing through it – known as the "weak phase object approximation". This approximation is valid for very thin crystalline samples as used in our experiments. This also implies that Bragg's law (Equation 2.3) holds for diffraction peaks formed, as outlined in Section 2.2. The intensity of Bragg spots is approximated by the square of the structure factor amplitudes (see Section 2.2). The lattice amplitude, i.e. the macroscopic dimensions of the crystal, is not taken into consideration, implying that a perfect, infinite lattice is used to calculate the diffraction pattern. Referring back to Section 2.2 this means that the reciprocal lattice in the simulation is made up of points, and not rods, implying no relaxation of the Bragg condition due to crystal shape. Simulations are calculated for 30 nm thick crystals of d_6 Cu(DCNQI)$_2$ and an electron energy of 30 keV. Room temperature simulations are based on the atomic lattice positions determined by Sinzger *et al.* via x-ray anlysis [15]. The simulation parameters therefore closely mimic the real UED experimental conditions. The simulation program produces electron diffraction images in which the spot area indicates the peak intensity – no grey scale is used for intensity indication. Figure 4.2 shows the simulated room temperature diffraction image. As before, the horizontal red line marks the zero order line of Bragg peaks. The vertical red line shows the central line of symmetry of the diffraction image. The directions and relative magnitudes of the reciprocal lattice vectors $\mathbf{a}^*$ and $\mathbf{c}^*$ are indicated by the green arrows at the bottom left, where $|\mathbf{a}^*| = \frac{1}{a} = \frac{1}{2.1619 \text{ nm}}$ and $|\mathbf{c}^*| = \frac{1}{c} = \frac{1}{0.3874 \text{ nm}}$ [15]. Rectangular boxes indicate the part of the first, second, and third order lines of diffraction peaks which are used for analysis.

As mentioned before the electron diffraction pattern was simulated in order to compare the diffraction pattern obtained in the UED experimental setup to a theoretical experiment based on a perfect thin crystal (unaltered by sample preparation). Comparing the UED electron diffraction pattern in Figure 4.1 to the simulated one in Figure 4.2 a similar complicated intensity distribution of the Bragg spots is observed. For example, considering the first order lines of diffraction peaks along the c^*-axis, above and below the horizontal red line: The same symmetry described for the UED diffraction image is seen in the simulated pattern with the red horizontal and vertical lines being lines of reflection. This close resemblance of the UED and simulated diffraction patterns indicates that the sample used in the experiment is intact and has the original crystalline structure as reported for the bulk crystal. The sample preparation of gluing, ultramicrotoming, floating on water, and drying therefore did not alter or damage the crystal lattice of the organic molecular salt. Neither did

the vacuum pressure (10^{-6} mbar) nor the electron flux (30 electrons/μm^2) change the sample. In order to confirm this qualitative analysis by a more rigorous, quantitative comparison between the diffraction patterns, the peak intensities were extracted from the images and plotted in Figure 4.3.

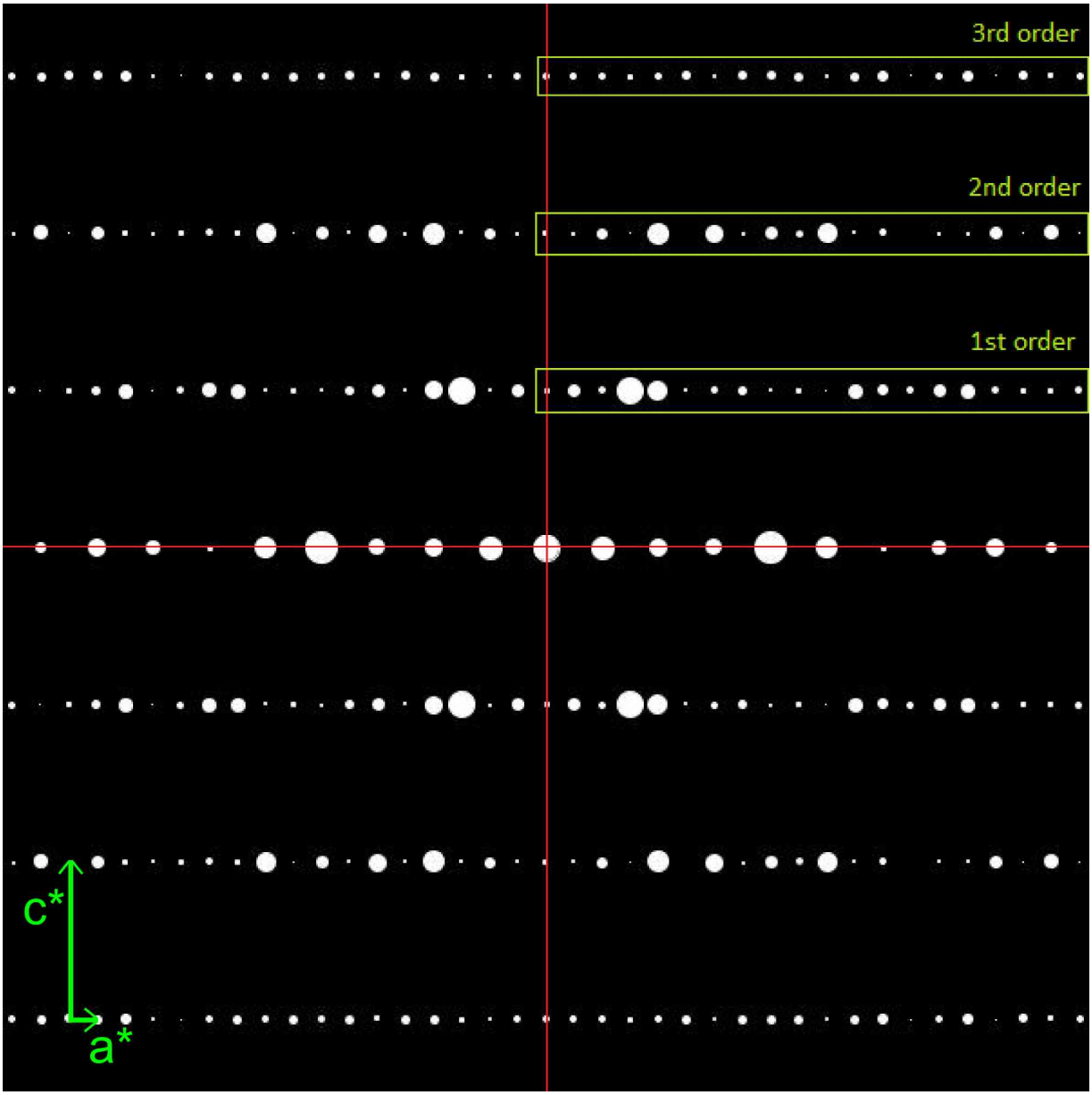

Figure 4.2: Room temperature simulation of the electron diffraction image of 30 nm thick d_6 Cu(DCNQI)$_2$.

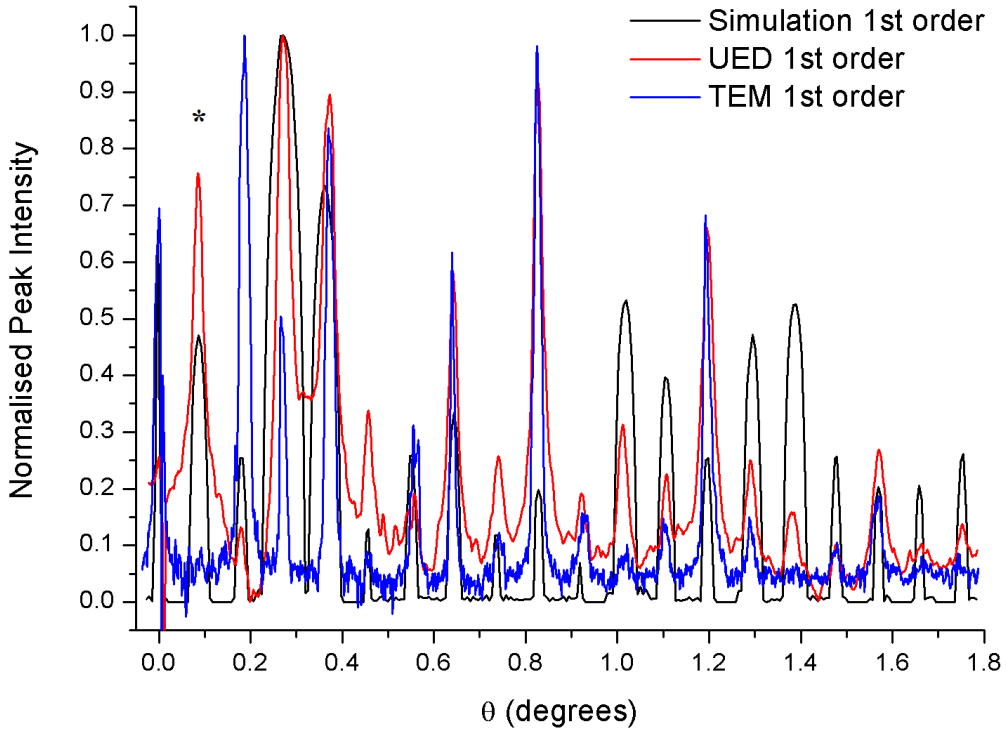

Figure 4.3: Line-outs of the first order line of diffraction peaks of the UED, simulation, and TEM images at room temperature as indicated by the rectangles in Figures 3.14, 4.1, and 4.2. The normalised peak intensity of the curves is plotted as a function of the diffraction angle θ indicated in Figures 2.12, 2.13. The asterisk indicates the first peak to the right of the red vertical symmetry line in the diffraction images.

The aim was to quantitatively compare the Bragg peak intensity distribution of the room temperature UED, TEM and simulated electron diffraction patterns. Therefore the relative peak intensities had to be extracted from the diffraction Figures 3.14, 4.1, and 4.2. As mentioned in the figure captions (Figures 3.14, 4.1), the original TEM and UED diffraction images were rotated to align the diffraction peak lines horizontally (as in the simulation). So called line-outs of the peak intensities of the diffraction peak lines could be extracted using a LabVIEW program written by former UED group member Kerstin Haupt [50]. The diffraction patterns with horizontally aligned diffraction peak lines are imported into the program. A horizontal rectangle is drawn around the peak lines whose intensity is to be plotted. As indicated in Figures 3.14, 4.1, and 4.2 the rectangles are drawn in such a way as to include part of the red vertical central symmetry line. The program integrates the data in vertical columns in this chosen rectangle, yielding a text file containing integrated peak pixel intensities as a function of pixel number. A similar rectangular area is integrated

just below the indicated diffraction peak line which gives the corresponding background curve, and is subtracted from the first set of integrated peak intensities. The resulting data is then imported into the analysis and graphing program OriginPro8 to create the line-outs. This red line segment included in the integration rectangle has a "grey pixel value" and therefore results in a steep, narrow peak in the plotted line-out. This peak served as an "alignment guide" when plotting more than one data set for comparison. These alignment peaks are included in the line-out (Figures 4.3 and 4.5), and are aligned to fall on the origin of the x-axis. The peak directly right – marked with an asterisk – of this first "alignment peak" corresponds to the first diffraction spot right of the red vertical central symmetry line in the diffraction images Figures 3.14, 4.1, and 4.2. The calibration of the x-axis was done by converting the pixel number on the image to the diffraction angle θ as indicated in Figures 2.12 and 2.13. The angle θ was calculated using Equation 2.4 and the known real width of the detector (40 mm): The distance from the sample to the detector in our setup is $L = 35$ cm; R was taken as the distance between the diffraction spot lying on the vertical red line of symmetry in the diffraction order being plotted and the diffraction peaks in that same diffraction order line. For example, from Figure 4.1 in the first order line of diffraction peaks along the c^*-axis, the distance between the vertical red line of symmetry and the first diffraction peak to the right of it was determined to be $R = 1.1$ mm on the real 40 mm wide detector screen. Using Equation 2.4, $\theta = \frac{1}{2}\arctan(\frac{R}{L}) = \frac{1}{2}\arctan(\frac{1.1\text{ mm}}{350\text{ mm}}) = 0.09°$ which is the angle at which the first diffraction peak under the asterisk is plotted in Figure 4.3. Normalisation for the room temperature line-outs was done relative to each data set, i.e. each of the line-out curves compared in Figure 4.3 was normalised with respect to its own maximum peak. The line-outs extracted from the UED, TEM, and simulated electron diffraction patterns therefore allow comparison between their intensity distributions along a particular row of diffraction spots. In Figure 4.3 line-outs of one half of the first order diffraction peak line in the UED, TEM, and simulation images are plotted.

Similar comparative line-out plots were done for the second and third order diffraction peak lines of the UED and simulated diffraction images, but are not presented here. The peak intensities were extracted from line-out plots similar to Figure 4.3. The peak values of the line-out plots are compared in Table 4.1. The peak amplitude in the UED and TEM experimental data (which can be approximated to a Gaussian profile) scales linearly with the diffraction intensity of a Bragg peak. The same linear correspondence was verified for the simulated data. Therefore the different data sets can be compared utilising the peak values. In order to compare the intensity distribution

along a diffraction peak line of one measurement to another the average standard deviation of the Bragg peaks are compared. This was calculated as follows: for example, in order to compare the intensity distribution of the first order diffraction peak line of the UED and simulated data, the peak values of the two line-outs are extracted. Then the standard deviation between each set of corresponding peaks (corresponding to the same relative position in the diffraction pattern) was calculated. (The formula for the standard deviation between the first peak in the UED pattern (U) and the first peak in the simulated pattern (S) would be: $\sqrt{(S - \frac{(S+U)}{2})^2 + (U - \frac{(S+U)}{2})^2}$.) This is done for every set of two peaks. The average standard deviation between the two data sets is then the average of all the standard deviations between corresponding peaks. This gives an indication of how well the intensity distribution along the diffraction peak line corresponds between the two data sets. The lower the average standard deviation between two line-outs, the better the correlation between the peak intensities of each peak position, the more alike the intensity distributions are.

In the three columns on the left in Table 4.1 it is indicated which data sets (and which diffraction peak line orders of each) were compared in the average standard deviation (Avg. Std Dev.) of Bragg Peaks column. From this data one can see that the intensity distribution along first order lines of the TEM and UED electron diffraction images correlate the best. This is remarkable considering that the two systems operate with strongly differing electron energies (UED $\rightarrow$ 30 keV; TEM $\rightarrow$ 200 keV) and electron fluxes (UED $\rightarrow$ 30 electrons/μm^2; TEM $\rightarrow$ 10^8 – 2×10^9 electrons/μm^2). The average standard deviation between the first order peaks in the simulated and UED diffraction images is in the same order (as UED and TEM first order). As outlined earlier the simulation parameters were adapted to closely match the UED experimental conditions. This may indicate that the experimental procedures in the UED setup and in the TEM alter neither the sample nor its diffraction pattern. Both experimental methods therefore provide diffraction patterns of the Cu(DCNQI)$_2$ crystal slice that closely resemble that of the simulation of the perfect thin crystal.

The fact that the average standard deviation between the higher order diffraction peaks differ more than for the first order may be an indication of the effect of the finite dimensions of the real crystal on the intensity distribution – which is not taken into account in the simulation, since only the structure amplitude and not the lattice amplitude are used in the simulation (as discussed earlier in this section). In Section 2.2 the effect of the small thickness of the sample on the reciprocal lattice spots and therefore on the allowed diffraction peaks are mentioned. The Bragg condition

may therefore be more relaxed in the experiment than in the simulation for higher order peaks, explaining the increased average standard deviation. Why the second order intensity distribution differs more between UED and simulation patterns than the third order is not understood at this point.

Table 4.1: Comparison between room temperature Bragg peak intensities of electron diffraction images from the UED setup, the TEM, and simulations.

Simulation	UED	TEM	Avg. Std Dev. of Bragg Peaks
1st order		1st order	20%
	1st order	1st order	12%
1st order	1st order		15%
2nd order	2nd order		29%
3rd order	3rd order		22%

In this section the procedures of obtaining initial room temperature diffraction patterns of the organic molecular salt in the UED setup were outlined. The transverse coherence length of the UED setup was verified, validating that well resolved diffraction patterns of the metallic and insulating phases of $Cu(DCNQI)_2$ are possible with UED. Furthermore the acquired diffraction pattern was analysed and the calculated lattice constants were confirmed to be within 10 % of the literature values. Qualitative and quantitative comparison between the room temperature electron diffraction images obtained in the UED setup, the TEM and from simulations has shown that the intensity distribution of the diffraction peaks is similar. This indicates that the $Cu(DCNQI)_2$ crystal is altered neither by the sample preparation procedures nor by the experimental conditions in the UED setup. Thus the organic molecular salt was successfully prepared and introduced into the ultrafast electron diffraction setup proving that initial metallic state room temperature experiments are possible. The next step is to investigate the low temperature insulating phase of d_6 $Cu(DCNQI)_2$.

4.2 Low temperature simulations

From the reports mentioned in Chapter 2 it is known that $Cu(DCNQI)_2$ salts undergo a trimerisation of the lattice constant c during their metal to insulator phase transition. During this transition

a charge ordering of the copper ions occurs as well as a CDW formation along the DCNQI stacks. X-ray diffraction images of copper salts similar to our sample have clearly displayed this characteristic CDW signature (see Figure 2.7 [6]). This pattern would also be expected in the electron diffraction images of insulating samples of d_6 Cu(DCNQI)$_2$ in the UED setup.

Since we have not yet been able to record this trimerisation, i.e. CDW formation, in our diffraction images (see Appendix A), simulations of the insulating low temperature phase of d_6 Cu(DCNQI)$_2$ crystals were calculated by Olufemi Olaoye. The same program [56] used for the room temperature simulations (as described earlier in this section) was used. Again a sample thickness of 30 nm was simulated and an electron energy of 30 keV. For the low temperature (insulating phase) diffraction simulations, data from two reports are combined: The DCNQI ion positions are based on Reference [15], while copper ion positions are based on Reference [6]. The low temperature was set to 20 K for this simulation of the d_6 Cu(DCNQI)$_2$ crystal structure (as in the reports by Sinzger *et al.* and H. Kobayashi *et al.* in 1993 [6]). Figure 4.4 shows the simulated diffraction pattern at 20 K. As in the room temperature diffraction images, the horizontal red line marks the zero order line of Bragg peaks. The vertical red line shows the central line of symmetry of the diffraction image. The directions and relative magnitudes of the reciprocal lattice vectors $\mathbf{a}^*$ and $\mathbf{c}^*$ are indicated by the green arrows at the bottom left, where $|\mathbf{a}^*| = \frac{1}{a} = \frac{1}{2.1619 \text{ nm}}$ and $|\mathbf{c}^*| = \frac{1}{c} = \frac{1}{0.3874 \text{ nm}}$ [15] . Two lines of CDW peaks can be seen between every two lines of Bragg peaks. Therefore the reciprocal lattice vector for the CDW corresponds to $\frac{\mathbf{c}^*}{3}$. Rectangular boxes indicate the part of the first and second Bragg diffraction peak lines as well as of the first four CDW peak lines which are used for analysis.

In the simulated electron diffraction of the organic molecular salt's insulating phase, two smaller, i.e. less intense, lines of CDW peaks between every two Bragg diffraction spot lines are shown. As mentioned before, this trimerisation was observed in similar samples at 20 K via x-ray diffraction (see Figure 2.7 [6]). This simulation therefore confirms qualitatively what diffraction pattern to expect of the copper salt in its insulating phase.

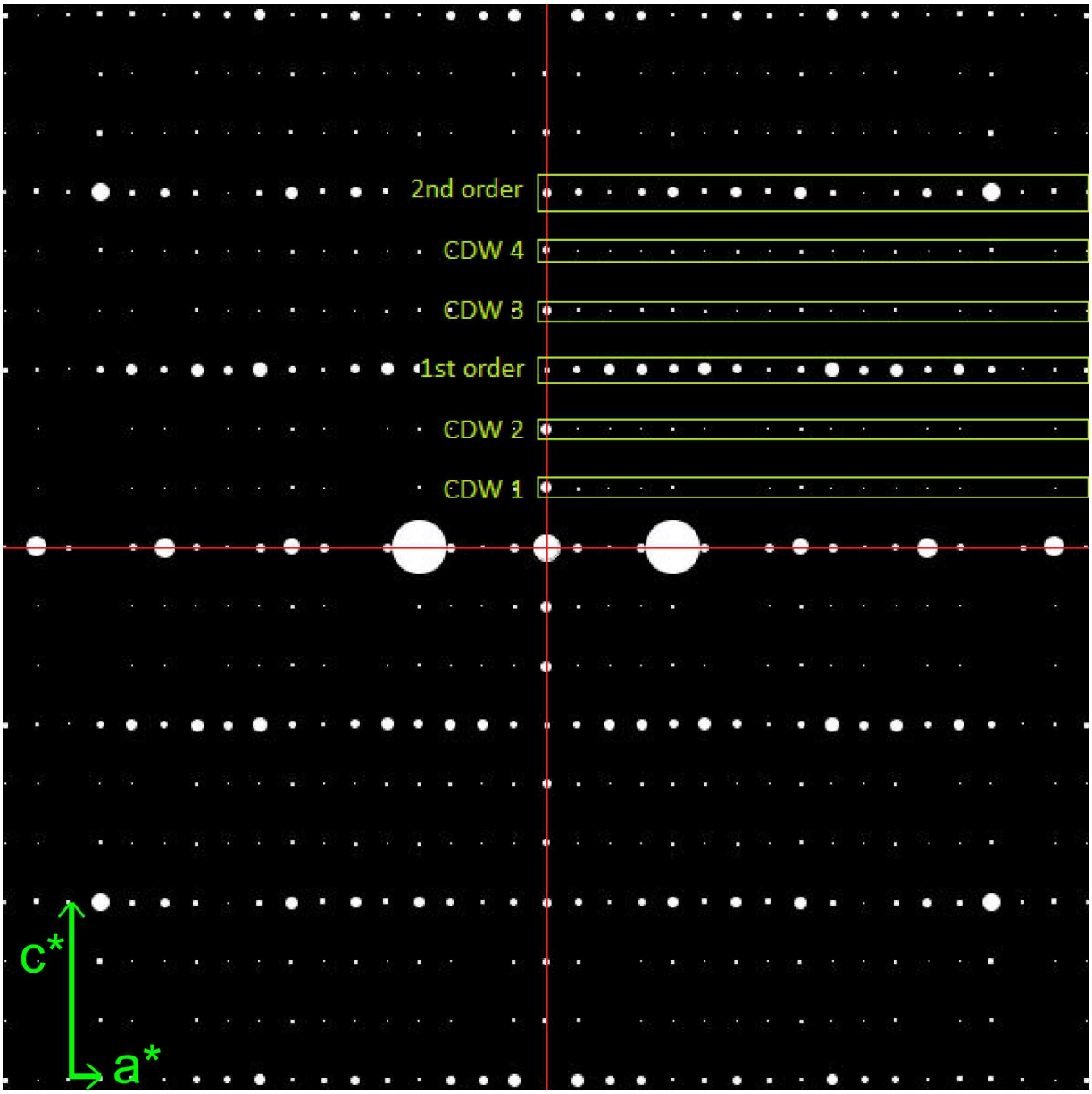

Figure 4.4: Low temperature (20 K) simulated electron diffraction image of a 30 nm thick sample of d_6 $Cu(DCNQI)_2$.

In order to investigate the intensity distribution quantitatively, line-outs were extracted from the simulated low temperature electron diffraction image in Figure 4.4 using the same procedure as outlined for the room temperature analysis. This was done primarily to compare the relative intensity of the CDW peaks to the Bragg peaks. The rectangles in Figure 4.4 indicate for which parts of the

diffraction peak lines line-outs were plotted. Similar steps as outlined for the room temperature line-out plots were followed. However, normalisation was carried out differently, since we are interested in the relative intensities of CDW and Bragg peaks: For a line-out plot comparing one Bragg line-out with two CDW line-outs all three data sets are normalised with respect to the maximum Bragg peak in that plot. Figure 4.5 is an example of one of the line-outs plotted: comparing the first Bragg order line with the first and second CDW peak lines.

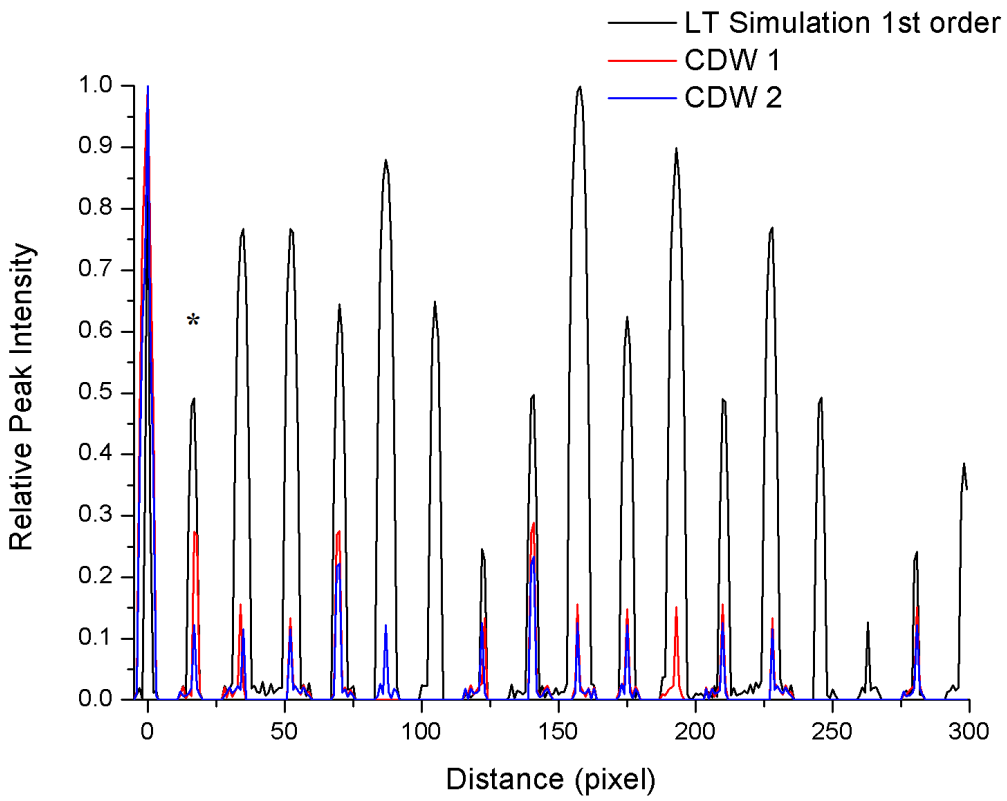

Figure 4.5: Line-outs of the first order Bragg peak line and the first and second CDW peak lines (situated between the zero and first order Bragg lines – as indicated in the low temperature electron diffraction simulation (Figure 4.4)). The relative peak intensities of the curves are plotted as a function of the pixel distance from the centre of the simulated diffraction pattern. The asterisk indicates the first peak to the right of the red vertical symmetry line in the simulated diffraction image.

As was done for the room temperature data, the intensity peaks of the line-outs were compared. The average standard deviation between CDW peaks was calculated in the same way as for the Bragg peaks in Table 4.1. In addition the average CDW to Bragg intensity ratio was calculated.

For this the average intensity of two CDW peaks being compared was calculated and divided by the Bragg peak's intensity they were compared to (corresponding peaks are at the same position on the x-axis in the line-out plot). For example, for a comparison between the first diffraction peak (at the asterisk) in the first order Bragg peak (Bragg_1) and first spot in each of the first two CDW peaks (CDW1_1 and CDW2_1): $\frac{\text{Avg. CDW}_1}{\text{Bragg}_1} = \frac{(\text{CDW1}_1+\text{CDW2}_1)\times 0.5}{\text{Bragg}_1}$. The percentage displayed in the last column of Table 4.2 is the average of all ratios of corresponding peaks. This parameter gives an indication of the relative intensity of the CDW signal compared to the Bragg signal. A summary of the comparison of the peak intensity data extracted from the line-outs is given in Table 4.2.

Table 4.2: Comparison between Bragg and CDW peaks in the low temperature (20 K) simulated diffraction pattern in Figure 4.4. The peak intensities used for analysis were extracted from line-out plots similar to Figure 4.5. The diffraction peak lines which were compared to each other in each set of analysis plots and calculations are marked by an "x".

Bragg Peak	CDW 1	CDW 2	CDW 3	CDW 4	Avg. Std Dev. between CDWs	(Avg. CDW)/(Bragg)
1st order	x	x			3%	22%
1st order			x	x	3%	30%
1st order		x	x		6%	25%
2nd order			x	x	3%	45%

From Table 4.2 the close similarity between the CDW lines' intensity distributions is indicated by the low average standard deviation between them: 3 % between adjacent CDW peak lines and 6 % between CDW 2 and CDW 3 (which are separated by the first order Bragg peak line). The parameter (Avg. CDW)/(Bragg) gives an indication of the relative intensity of the CDW signal compared to the Bragg signal. The greater the (Avg. CDW)/(Bragg) percentage, the stronger the CDW signal is compared to the Bragg signal, the more likely it is to be observed in a diffraction pattern. On average (across all orders analysed) the CDW signal should therefore be about 30 % of the Bragg intensity. The assumption in the simulation is that the entire crystal lattice is in the insulating phase configuration. Therefore the (Avg. CDW)/(Bragg) = 30 % ratio applies to a sample that underwent a 100 % metal to insulator phase transition.

The low temperature electron diffraction simulation of the insulating phase of a perfect, 30 nm thick crystal of d_6 Cu(DCNQI)$_2$ indicates the CDW signature with a $\frac{c^*}{3}$ reciprocal lattice vector length (confirming previous reports by Reference [6]). Quantitative analysis of the intensity distribution revealed that the CDW signal of a fully converted, insulating crystal is in the order of 30 % of the Bragg peak signal. In order to verify whether this strong relative CDW signal should be observable in the UED setup, additional analysis of the recorded UED diffraction images was undertaken.

4.3 UED image quality

The quality of the recorded electron diffraction images was evaluated in terms of coherence length and signal-to-noise ratio. The coherence length of the measurement was estimated from the diffraction image as outlined in Section 2.3 along the $\mathbf{a}^*$ and $\mathbf{c}^*$ directions. The value of $L_\perp \sim$100 Å reported in Reference [53] was confirmed (in both directions). This verifies that well resolved diffraction images can be obtained containing signatures of Cu(DCNQI)$_2$'s molecular stacks at room temperature with a periodicity of $c \sim$4 Å, as well as its CDW formed at low temperatures with $3c \sim$12 Å periodicity, because $L_\perp > 3c > c$ (see Section 2.3).

The signal and read-out noise intensities were measured in pixel intensity counts employing the same LABVIEW program used to produce the peak intensity line-outs. Only a fraction of the 16-bit bit-depth ($2^{16} = 65536$ counts) of the CCD camera is exploited during standard measurements, i.e. 60 s exposure time, 1000 electrons per pulse, 4500 V MCP voltage. Unsaturated diffraction peaks were therefore obtained allowing comparison between peak intensities of different images. The signal-to-noise ratio was calculated by dividing the average peak intensity of first order diffraction peaks, as indicated in Figure 4.1, by the average read-out noise peak height between the zero, first, and second order lines of Bragg peaks. The following parameters were varied in order to compare their effect on the signal-to-noise ratio in the images obtained: exposure time (60 – 120 s), number of images added (1 – 40 images), electron number per pulse (1000 – 10000 electrons/pulse), and sample temperature (30 – 300 K). The experiments were all performed on similar samples of 25 nm thick d_6 Cu(DCNQI)$_2$. No trend in the signal-to-noise ratio was found when changing the exposure time, electron number per pulse, or sample temperature. This indicates that increasing the exposure time or the number of electrons raises both, the peak intensities and the background signal, while leaving the signal-to-noise ratio unaffected. (See Appendix A for a discussion on the sample

temperature.) Overall, an enhancement in the signal-to-noise ratio was measured when increasing the number of images added to form a diffraction pattern. For adding between one to five images a signal-to-noise ratio of about 20 was achieved on average. This ratio was on average more than doubled when adding between 30 and 40 images to create one diffraction image. The worst signal-to-noise ratio obtained for all the varied parameters was about 6 (at 35 K, 1000 electrons/pulse, 60 s exposure time, 8 images added), while the best ratio was about 50 (30 K, 1000 electrons/pulse, 60 s exposure time, 35 images added). Two different samples, prepared in the same way, where used for these experiments. (See Appendix A for further discussion on the effect of cooling.) This analysis gives an indication of the range of signal-to-noise ratios in electron diffraction images of $Cu(DCNQI)_2$ crystals recorded in the UED setup. It also indicates that signal-to-noise ratios are improved by adding more images to obtain an analysable diffraction pattern.

With this UED image quality analysis and the results from the previous Section 4.2 it can now be discussed why CDW peaks should be observable in the UED setup.

4.4 Why the insulating phase of d_6 $Cu(DCNQI)_2$ should be observable in the UED setup if it occurred

In this section findings of the previous Sections (4.1, 4.2, 4.3) as well as results from experiments previously performed in the UED setup will be reviewed in order to discuss why the insulating phase of d_6 $Cu(DCNQI)_2$ should be observable in the UED setup when it does occur.

Firstly the room temperature electron diffraction image analysis and comparison to the simulation (Section 4.1) showed that the crystal lattice of the ultra-thin sample was not detectably altered by sample preparation or experimental conditions in the UED setup at room temperature. The sample was therefore introduced into the setup with the same crystalline lattice structure as the bulk salt (which has been proved to undergo the phase transition by conductivity measurements (see Section 3.2)).

Secondly, the transverse coherence length ($L_\perp$) was found to be at least eight times larger than the periodicity of the CDW ($3c$) formed along the DCNQI stacks. The UED setup is therefore capable of spatially resolving this CDW signal.

Also, the signal-to-noise ratio in electron diffraction images obtained for this organic molecular salt shows no trend with change in temperature, i.e. cooling the sample below its phase transition temperature does not affect the signal-to-noise ratio of the images. Furthermore the ratio could be improved by superimposing more images in order to create an analysable diffraction pattern. Sufficient signal-to-noise ratios are therefore achievable at low temperatures in order to observe the CDW peaks.

Moreover, simulation of the insulating phase showed that the average CDW signal intensity is in the order of 30 % of the Bragg signal (when the entire sample is transformed). This would imply that even for the weakest signal-to-noise ratio of six, measured for this sample, the CDW signal would be almost twice as large as the background signal and therefore observable. For a more realistic signal-to-noise ratio of 20, the average CDW peak would be six times as large as the background signal.

Previously performed ultrafast electron diffraction on other CDW materials in our setup [50, 52] showed clearly visible CDW peaks which had an intensity in the order of 1 % of the Bragg intensity (with similar experimental conditions). Even relatively weak CDW signals are therefore observable in the UED setup.

All of the arguments listed so far, point out that we should be able to observe the insulating phase's CDW signature with our setup parameters if the entire d_6 Cu(DCNQI)$_2$ sample is converted into its insulating phase. However, as mentioned in Section 2.1, References [5, 7, 39] suggest the formation of microdomains during phase transition. That is, not the entire sample changes into the insulating phase at the phase transition temperature, but a growing number of small domains of the crystal undergo the transition as the temperature changes (*). Applying this model to our measurements, this would mean that at least 3 % – 4 % of the crystal has to undergo the phase transition for a visible change in the diffraction images. This is assuming that the CDW to Bragg signal ratio has to be in the order of 1 % to be observable in the UED setup [50], and that the CDW intensity in a completely (100 %) converted sample is about 30 % of the Bragg signal – as demonstrated with the low temperature simulations. This implies that less than 3 % of the sample must have been converted to its insulating phase during measurements performed to date, given that the CDW signal was not observed in our setup yet.

*[Note that the domain formation hypothesis [5, 7, 39] explains the abrupt jump in conductivity across the phase transition temperature, indicating an "all or nothing" conversion in the conductivity behaviour. However, also the comparatively gradual change in length during the transition is possible with the domain-explanation (see Section 2.1). Structural changes during the phase transition therefore seem to occur gradually. As discussed in Section 2.1 structural changes of the crystal lattice are believed to induce CDW formation along the DCNQI stacks and charge ordering of the copper ions [18, 28, 30]. For that reason the CDW signature may also appear gradually in the electron diffraction pattern as insulating domains grow in number and size throughout the crystal. (Reference [52] suggests that CDWs in transition metal dichalcogenides can develop domains. Whether this is possible in copper-DCNQI crystals has to be further investigated.)]

Overall, in terms of image formation ability (transverse coherence length, signal-to-noise ratio) as well as sample quality and characteristics (strength of CDW/Bragg ratio) we are confident that a phase transition of more than 4 % of the sample to its insulating phase is observable in the UED setup. Given that to date no CDW signature has been detected, less than 3 % of the sample must have been converted, or other factors obstructing the observation of the phase transition must be investigated. This will be discussed in the following section.

4.5 Possible reasons why the phase transition was not detected

Possible factors preventing the phase transition of the thin crystal of d_6 Cu(DCNQI)$_2$ will be investigated in this section. Also causes for potential obstruction of the detection of the CDW signal will be outlined.

A possible factor that may prevent the sample from undergoing its structural change during cooling is that the contraction along the c-axis is prevented. As reported in the literature, e.g. [5, 25, 32], the phase transition of this organic molecular salt is extremely sensitive to pressure – external and internal. Reference [5] points out that "mechanical tension may prevent a phase transition as the lattice is expanded". As seen in Figure 3.6 a sample slice on a copper TEM mesh typically spans across a mesh hole, lying on two grid bars along its c-axis. copper's linear thermal expansion coefficient ($\alpha_{Cu} = 16.5\times10^{-6}$ K^{-1} [57]) is a quarter of Cu(DMe-DCNQI)$_2$'s ($\alpha_{Cu-DCNQI} = 70\times10^{-6}$ K^{-1} [58]).

Schmitt *et al.* reported that tension lowers the phase transition temperature of d_6 $Cu(DCNQI)_2$ [5]. Therefore it is possible that, due the difference in contraction between the sample and the copper mesh, the tension exerted along the sample's c-axis lowers the phase transition temperature to below 30 K (making it inaccessible for our setup).

[Note that the low vacuum pressure of 10^{-6} mbar in our electron diffraction setup, which is nine orders of magnitude below ambient pressure (1013.25 mbar), is assumed not to affect the samples structure. This assumption is validated by the fact that this vacuum pressure is evenly exerted on the sample – and not in one particular direction. The sample is therefore not subjected to tension or pressure along a specific crystal axis. Hence the tetragonal coordination around the Cu ion, i.e. the coordination angle (α) which directly influences the phase transition behaviour of the crystal (see Section 2.1) should remain unaffected by the vacuum environment in which the electron diffraction is conducted.]

As mentioned in Appendix A samples seem to degrade during the cooling process (diffraction images at low temperatures and at room temperature after cooling show less defined (more smeared out) diffraction spots). This observation leads to the hypothesis that during cooling the tension exerted by the copper mesh on the contracting crystal slice causes the development of microcracks in the sample. However, the CDW formation is assumed to occur via domain formation (see Section 4.4 [5]). Therefore the question arises whether CDW domains should appear even if the sample is polycrystalline due to microcracks: To our knowledge, experiments exerting tension on the crystal, thus preventing the phase transition, have only investigated the conductivity behaviour of the sample [5]. But conductivity (unlike the structural changes) relies on the connectivity of the microdomains (as discussed in Sections 2.1 and 4.4). Also, the effect of tension on the CDW formation has not been studied via diffraction methods to our knowledge (so far x-ray diffraction has only been applied to pressure studies [6, 31]). From previous studies it is therefore unclear whether CDW domains form in a sample under tension or in polycrystalline samples. Thus far our experiments suggest that this is not the case (or more specifically that less that 4 % of the sample are transformed when under tension, or possibly polycrystalline).

Another possible reason for the less defined diffraction patterns (with blurry, less sharp diffraction spots) observed at low temperatures is condensate formation on the sample (as outlined in

Appendix A). The condensate possibly causes additional scattering of the electrons (before and after diffraction by the sample) thus obscuring the diffraction pattern and consequently preventing the observation of the CDW in the sample. Another aspect to be considered in this regard is the possibility of sample degradation caused by the condensate: During sample preparation (ultramicrotoming) the sample slices were floated on water. This did not alter the crystal (as discussed in Section 4.2). However, the microcracks caused by the tension on the sample, might allow the condensate (presumably water) to aggravate sample degradation. The formation of condensate on the sample may therefore prevent the observation of the CDW pattern, by obscuring the diffraction process and possibly worsen sample degradation.

The tension exerted onto the sample during cooling in the current method of mounting it as well as condensate formation are factors probably preventing the transition to, and possibly the observation of the insulating state of the copper-DCNQI salt. Ways in which our current experimental methods can be improved in order to enable the detection and investigation of the CDW formation thus have to be found.

4.6 Outlook: Improvements

Possible improvements on our current experimental techniques in order to overcome the challenges outlined in the previous section 4.5 will be discussed in this section.

In order to allow the phase transition to occur and to prevent sample degradation due to tension, methods of mounting the crystal slice allowing free contraction have to be found:

A "free standing" sample slice would be ideal for this purpose. Figure 4.6 shows a sample on a TEM mesh which is free on three sides. The slice was captured in this way by chance during sample collection as described in Section 3.3. However, with our current method of collecting the samples off the knife boat's water surface we cannot control the placement on the mesh. The ~30 nm thin crystals are also very delicate and easily break off the grid during further sample preparation (e.g. gluing onto the sample mount), before cooling experiments can be performed. Therefore more sustainable and repeatable methods of mounting the sample have to be found.

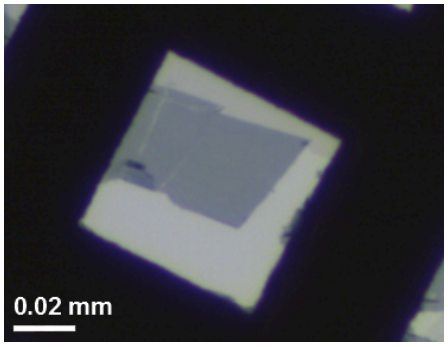

Figure 4.6: A 30 nm thick $Cu(DCNQI)_2$ crystal with only one side lying on the grid of the copper TEM mesh.

Currently the most promising idea to improve on our current sample preparation in order to allow freer contraction of the crystal slices is the use of TEM meshes coated with specialised films. One option are copper meshes coated with "lacey carbon" (catalog number: Plano S166-2). The carbon film has large holes of a 5 μm – 10 μm diameter with <1 μm carbon filaments in between, i.e. a carbon coverage of about 10 % – 20 % per area. The advantage is that a big portion of the sample has no substrate underneath it. This is important since the linear expansion coefficient of graphite, $\alpha_{graphite} = 0.63 \times 10^{-6}$ K^{-1} [59], is an order of magnitude smaller than that of copper, $\alpha_{Cu} = 16.5 \times 10^{-6}$ K^{-1} [57], which would aggravate the difference in linear expansion coefficient between $Cu(DCNQI)_2$, $\alpha_{Cu-DCNQI} = 70 \times 10^{-6}$ K^{-1} [58], and substrate – compared to the ordinary copper meshes. With the lacey carbon coating, though, the sample is almost free standing with the sample area in contact with the carbon being about 10 % – 20 %. Also the diffraction images will only show marginal scattering from the minimal carbon film.

The other set of meshes are Formvar (polyvinyl pormal) coated copper meshes. Formvar has a similar expansion coefficient as polyimides ($\alpha_{polyimide} = 3.2 \times 10^{-5}$ K^{-1} [60]). (Polyimides and Formvar both consist of chains containing aromatic rings, therefore their expansion coefficients are assumed to be of the same order.) The expansion coefficients of Formvar and the organic molecular salt are therefore of the same order. This promises to allow less restricted contraction of the copper salt during the cooling process.

An ultra high vacuum (UHV) chamber is currently being set up by the UED group. Pressures down to $\sim 10^{-9}$ mbar, i.e. three orders of magnitude lower than the current high vacuum chamber, are

anticipated in this chamber. This will decrease water condensation [61], because the boiling point of water in the picobar regime is about 20 K lower than at nanobar pressures [62]. The UHV chamber is also equipped with a load lock system: A small sample loading pre-chamber which can be ventilated separately from the main vacuum chamber. The sample can thus be exchanged without ventilating the entire chamber. This avoids air exposure of the main chamber (and thus prevents water vapour from entering). Therefore fewer water molecules can adsorb onto the chamber's inside surfaces. Hence the probability for condensate formation on the sample at low temperatures is further decreased. Another advantage of implementing the load system is that the main chamber stays at low pressures during sample mounting thus significantly decreasing the time for pumping back down to UHV pressures after sample exchange – from over night to several minutes. The UHV chamber with the load lock system therefore allows for efficient operation.

Performing electron diffraction in the ultra high vacuum chamber on thin slices of partially deuterated copper salts of DCNQI mounted on Formvar or lacey carbon coated TEM meshes promises to allow the detection and study of the insulating state of the sample. This would be a further step toward the end goal of transient ultrafast electron diffraction experiments on this organic molecular salt.

4.7 Further experiments: Suggestions

In this section suggestions for experiments related to those discussed so far are outlined.

The main structural change of the partially deuterated copper salt occurs along its c-axis. Our experiments therefore focused on diffraction off the a-b plane of the crystal (as discussed in Section 3.3). Another interesting investigation would be diffraction off other crystal planes of the $Cu(DCNQI)_2$ samples, e.g. the a-c plane. This is the view of the projection onto the c-axis, as illustrated in Figure 2.2. Due to the quasi one-dimensional structure of the needle-like crystals it is challenging to ultramicrotome the sample perpendicular to the c-axis. The crystal slices have a very small area – about (80×80) μm^2 in contrast to the previous (2000×80) μm^2. TEM meshes with smaller hole diameters (e.g. 600 or even 1000 TEM meshes) have to be used. To date, attempts to collect ultramicrotomed crystals cut in this direction have not been successful. The needles are more brittle along the c-axis, i.e. the slices of the a-b plane tend to break apart. However, first room

and low temperature electron diffraction simulations have been calculated by Olufemi Olaoye the "Simulations and Analysis of Electron Diffraction" program [56]. These are shown in Figures 4.7 (a) and (b) respectively.

Comparing Figures 4.7 (a) and (b), an increase in the number of diffraction spots from the metallic to the insulating state diffraction patterns is observed: More, smaller, and more closely spaced diffraction spots are seen in the low temperature image. This indicates some form of CDW formation in this plane of the crystal. It would be interesting to relate this modulation to structural changes along the c-axis of the crystal.

Different DCNQI could also be investigated. Currently Cu(MeBr-DCNQI)$_2$ salts are grown at the University of Würzburg by Florian Hüwe. These crystals contain R$_1$,R$_2$ = CH$_3$,Br forming Cu(MeBr-DCNQI)$_2$ (instead of what was investigated so far (Cu(2,5-(CD$_3$)$_2$-DCNQI)$_2$). Being a member of the copper-DCNQI salts, Cu(MeBr-DCNQI)$_2$ has similar chemical and physical properties as Cu(2,5-(CD$_3$)$_2$-DCNQI)$_2$ (e.g. the same space group ($I4_1/a$), similar pπ-d orbital mixing between the copper and DCNQI stacks, a metal-insulator phase transition induced by the structural deformation of the tetrahedral structure around the copper ion, CDW formation along the DCNQI stacks) [30]. As discussed in Section 2.1, substituting less bulky side R_1, R_2 groups increases the phase transition temperature of the crystal. Compared to our previous sample (d_6 Cu(DCNQI)$_2$) one of the methyl groups is replaced by a less bulky bromine atom. Therefore the MeBr molecular salt displays a higher phase transition temperature (T$_{MI,MeBr}$ = 156 K [30]) than the partially deuterated dimethyl copper salt (T$_{MI,d_6}$ $\sim$ 70 K [7]). This higher phase transition temperature is advantageous, because the formation of condensate on the sample only becomes visible in the diffraction patterns below $\sim$150 K in the old high vacuum chamber (see Appendix A). The MeBr salt should therefore undergo its metal to insulator phase transition before water condenses on the sample. Hence the factor of condensation could be eliminated from the experiment. In this way it could be investigated whether structural changes in a copper-DCNQI salt are observable in our setup when the issue of condensation is eliminated, but all other experimental factors are kept constant. The high phase transition temperature would also be advantageous in case the sample's phase transition temperature is decreased due to tension exerted by the TEM mesh (as discussed in Section 4.5). In this case cooling below the lowered phase transition temperature might still be possible. Therefore, with its higher phase transition temperature Cu(MeBr-DCNQI)$_2$ would (a)

enable us to eliminate condensation as a possible cause for disguising or preventing the CDW signal, and (b) allow for a larger accessible temperature range below the phase transition temperature, in case tension on the sample lowers the phase transition temperature.

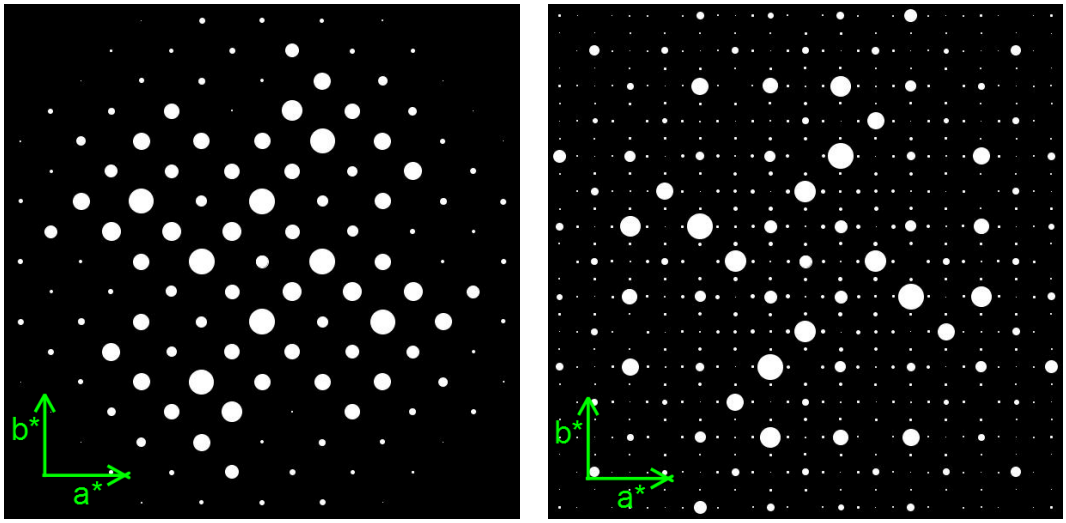

(a) **(b)**

Figure 4.7: Simulated electron diffraction image of the a-b plane of 30 nm thick d_6 Cu(DCNQI)$_2$. **(a)** Shows the calculated metallic phase pattern (at 300 K), and **(b)** the insulating phase pattern (at 20 K). The green arrows indicate the directions of the reciprocal lattice vectors $\mathbf{a}^*$ and $\mathbf{b}^*$ in both images.

An investigation of different crystal orientations of the current sample (d_6 Cu(DCNQI)$_2$) and/or similar copper-DCNQI salts with slightly different phase transition properties would further enhance the understanding of this class of organic molecular crystal salts. Experimental attempts on two other organic molecular salts (Li(DCNQI)$_2$ and TTF-TCNQ) are outlined in Appendix B.

CHAPTER 5
SUMMARY

This thesis addressed the introduction of molecular radical anion salts into our UED setup. With this, the first steps towards the investigation of structural dynamics of the metal to insulator phase transition of these samples in our pump-probe ultrafast electron diffraction setup were taken.

Firstly a broad overview of studies done over the past few decades on the family of DCNQI crystals, and specifically its copper salts, was presented in Chapter 2. Chemical and physical properties underlying the extraordinary conductivity and metal to insulator phase transition behaviour of this subclass of radical anion salts were discussed. This was followed by an outline of light-induced phase transition experiments on $Cu(DCNQI)_2$ crystals performed by other groups previously. Mention was made of reports demonstrating the ability to observe structural differences between the crystal's phases via diffraction methods. Subsequently basic concepts of diffraction theory were explained. The use of electron diffraction was justified by its ability to resolve atomic length-scales of crystalline lattices due to its short de Broglie wavelength. Crystalline structure was then related to the concept of reciprocal space, after which the Ewald sphere construct as a means to predict the Bragg-allowed diffraction pattern was introduced. The basic theory underlying electron diffraction as a crystal structure analysis tool was therefore outlined. Following this, the ultrafast electron diffraction experiment was described as a method to investigate dynamic changes in the crystalline lattice. The experimental techniques utilised to realise this were briefly explained in terms of the pump probe technique, enabling observation of ultrafast structural dynamics, creation and propagation of a pulsed electron beam employing the photoelectric effect, sample requirements posed by the characteristics of the electron and laser beams, temperature control of the sample to regulate its state, and the quality of detectable electron diffraction patterns determining the structural periodicities which are observable in this setup. In this way the efficacy and relevance of the ultrafast electron diffraction technique for the investigation of the structural characteristics of the phase transition in $Cu(DCNQI)_2$ salts was summarised.

Chapter 3 entailed descriptions of the preparation of the sample for the UED experiment. Basic concepts of the sample synthesis were outlined. Conductivity measurements characterised and

confirmed the crystals' temperature dependent phase transition behaviour. Next, the sample preparation techniques employed in order to meet the requirements posed by the UED setup were described: ultrathin, free-standing crystal slices were produced using an ultramicrotome. Subsequent room temperature white light absorption spectroscopy measurements verified the optical penetration depth into the crystal in its metallic state, laying the foundations for optimal UED experiments. Transition electron micrographs were used to gauge the sample quality in order to improve sample preparation techniques. First electron diffraction images were also recorded in the TEM. Subsequently lattice constants were calculated showing good agreement with literature values. The chapter was rounded off by a comparison between the TEM and UED systems, concluding that the former is an ideal diagnostic tool in preparation for experiments in the latter.

The introduction of a partially deuterated $Cu(DCNQI)_2$ salt into the UED setup was described in Chapter 4. First room temperature electron diffraction images of the metallic state of the sample were successfully recorded. Calculation of crystal lattice constants and comparing the detected diffraction peak intensity to simulated data proved that the crystal structure was intact and unaltered by experimental procedures. Thereafter, low temperature electron diffraction simulations confirmed the expected CDW signature of the insulating state of the crystal. It was determined that the CDW-to-Bragg signal ratio of a fully transformed crystal would be in the order of 30 %. Along with the verified quality of images recordable in the UED setup, in terms of diffraction peak resolution power and signal-to-noise ratio, this result validated that the CDW signal of a fully insulating $Cu(DCNQI)_2$ crystal slice could be detected in our UED setup. However, even at temperatures far below the expected phase transition temperature, this insulating phase's signature has to date not been observed. The possibility of partial phase transition, allowed by microdomain formation, as suggested in the literature, was conjectured. Undetectably weak CDW signals would mean that less than four percent of the sample is transformed into its insulating phase in our setup. Consequently possible technical reasons preventing the transition or observation of the CDW peaks were discussed. Tension on the sample, due to the current method of mounting thin crystal slices, may (a) prevent or shift the transition temperature to unattainably low temperatures and (b) cause sample degradation in the form of microcrack formation. The latter is also a possible explanation for the decrease in sharpness of diffraction peaks during cooling cycles. This decrease in diffraction pattern quality is additionally aggravated by condensation of water molecules on the sample surface at low temperatures. The condensate probably obscures electron diffraction and might aggravate

sample degradation. Consequently improvements on sample preparation, e.g. using TEM meshes with specialised coating for mounting sample slices to decrease the tension experienced by the crystal slice during cooling, and the UED setup, e.g. an ultra high vacuum chamber operating at lower pressures thus decreasing the probability of condensate formation, were outlined. In this way chances of detecting the CDW signal of the $Cu(DCNQI)_2$ salt are improved. Finally, suggestions for related experiments were made. These included investigating other crystal orientations of the same sample and similar samples exhibiting a higher phase transition temperature and therefore possibly further increasing the probability of CDW detection.

In conclusion, a thin sample of organic molecular $Cu(DCNQI)_2$ was successfully prepared and introduced into the ultrafast electron diffraction setup resulting in an analysable diffraction pattern of its metallic state. Subsequent studies and analysis have narrowed down the aspects that still make the observation of the insulating phase elusive. Further, improvements suggested in this thesis should make the objective of recording ultrafast dynamics of the metal to insulator phase transition of organic molecular crystals utilising ultrafast electron diffraction a realisable goal in future.

BIBLIOGRAPHY

[1] Y. Yamakita, Y. Furukawa, A. Kobayashi, M. Tasumi, R. Kato, and H. Kobayashi. Vibrational studies on electronic structures in metallic and insulating phases of the Cu complexes of substituted dicyanoquinonediimines (DCNQI). A comparison with the cases of the Li and Ba complexes. *The Journal of Chemical Physics*, 100(4):2449–2457, 1994.

[2] H. Kobayashi, R. Kato, A. Kobayashi, T. Mori, and H. Inokuchi. The first molecular metals with ordered spin structures, R_1R_2-DCNQI$_2$Cu (R_1, R_2= CH_3, CH_3O, Cl, Br) - Jahn-Teller distortion, CDW instability and antiferromagnetic spin ordering. *Solid State Communications*, 65(11):1351–1354, 1988.

[3] F. O. Karutz. *Optisch induzierte transiente elektrische Leitfähigkeit von DCNQI-Radikalionensalzen*. PhD thesis, 3. Physikalisches Institut der Universität Stuttgart, 1997.

[4] R. Kato, H. Kobayashi, and A. Kobayashi. Crystal and electronic structures of conductive anion-radical salts, (2,5-R_1R_2-DCNQI)$_2$Cu (DCNQI = N, N'-dicyanoquinonediimine; R_1, R_2= CH_3, CH_3O, Cl, Br). *Journal of the American Chemical Society*, 111(14):5224–5232, 1989.

[5] H. Schmitt, J.U. von Schütz, H. Wachtel, and H.C. Wolf. Light, pressure, and stress induced phase transitions of deuterated Cu(DCNQI)$_2$ radical ion salts. *Synthetic Metals*, 86:2257–2258, 1997.

[6] H. Kobayashi, A. Miyamoto, R. Kato, F. Sakai, A. Kobayashi, Y. Yamakita, Y. Furukawa, M. Tasumi, and T. Watanabe. Mixed valency of Cu, electron-mass enhancement, and three-dimensional arrangement of magnetic sites in the organic conductors (R_1, R_2-N, N'-dicyanoquinonediimine)$_2$Cu (where R_1, R_2 = CH_3, CH_3O, Cl, Br). *Physical Review B*, 47(7):3500, 1993.

[7] D. Bauer, J. U. von Schütz, H. C. Wolf, S. Huenig, K. Sinzger, and R. K. Kremer. Alloyed deuterated Copper-DCNQI salts: Phase transitions and reentry of conductivity, giant hysteresis effects, and coexistence of metallic and semiconducting modes. *Advanced Materials*, 5(11):829–834, 1993.

[8] R. Kato. Conductive Copper salts of 2,5-disubstituted N,N'-Dicyanobenzoquinonediimines

(DCNQIs): Structural and physical properties. *Bulletin-Chemical Society of Japan*, 73(3):515–534, 2000.

[9] F. O. Karutz, J. U. von Schütz, H. Wachtel, and H. C. Wolf. Optically reversed Peierls transition in crystals of Cu(dicyanoquinonediimine)$_2$. *Physical Review Letters*, 81(1):140–143, 1998.

[10] S. H. Simon. *The Oxford Solid State Basics*. Oxford University Press, 2013.

[11] I. Boshoff. Ultrafast electron diffraction on the charge density wave compound 4H$_b$ -TaSe$_2$. Master's thesis, Stellenbosch University, 2012.

[12] L. Reimer. *Transmission Electron Microscopy: Physics of image formation and microanalysis*. Springer, Berlin, 1984.

[13] F. Hüwe. Growth and characterization of radical anion salt single crystals. Diplomarbeit der Nanostrukturtechnik, Julius-Maximilians-University of Würzburg, Faculty of Physics and Astronomy Experimental Physics VI, 2012.

[14] E. J. Rohwer. *Ultrafast photodynamics of ZnO solar cells sensitized with the organic indoline derivative D149*. PhD thesis, Stellenbosch University, 2014.

[15] K. Sinzger, S. Hünig, M. Jopp, D. Bauer, W. Bietsch, J. U. von Schütz, H. C. Wolf, R. K. Kremer, T. Metzenthin, R. Bau, S. I. Khan, A. Lindbaum, C. L. Lengauer, and E. Tillmanns. The organic metal (Me$_2$-DCNQI)$_2$Cu: Dramatic changes in solid-state properties and crystal structure due to secondary deuterium effects. *J. Am. Chem. Soc.*, 115(17):7696–7705, 1993.

[16] K. Hiraki and K. Kanoda. Comparative study on the magnetism and conductivity of (DI-DCNQI)$_2$M,(M= Li, Cu, Ag). *Synthetic Metals*, 86(1):2103–2104, 1997.

[17] Y. Kashimura, H. Sawa, S. Aonuma, R. Kato, H. Takahashi, and N. Môri. Anomalous pressure-temperature phase diagram of the molecular conductor, (DI-DCNQI)$_2$Cu (DI-DCNQI= 2, 5-DIIODO-n,n'-dicyanoquinonediimine). *Solid State Communications*, 93(8):675–679, 1995.

[18] R. Kato, H. Sawa, S.i Aonuma, M. Tamura, M. Kinoshita, and H. Kobayashi. Preparation and physical properties of an alloyed (DMe-DCNQI)$_2$Cu with fully deuterated DMe-DCNQI (DMe-DCNQI = 2,5-dimethyl-N,N'-dicyanoquinonediimine). *Solid State Communications*, 85(10):831–835, 1993.

[19] S. Aonuma, H. Sawa, Y. Okano, R. Kato, and H. Kobayashi. Synthesis of DMe-DCNQI-d_7 and deuterium-induced metal-insulator transition of (DMe-DCNQI-d_7)$_2$Cu. *Synthetic Metals*, 58(1):29–38, 1993.

[20] S. Hünig and E. Herberth. N, N'-dicyanoquinone diimines (DCNQIs): Versatile acceptors for organic conductors. *Chemical Reviews*, 104(11):5535–5564, 2004.

[21] M. Meneghetti, G. Lunardi, R. Bozio, and C. Pecile. Structural instabilities of molecular conductors studied by optical spectroscopy: phase transitions of (DM-DCNQI)$_2$X (X = Ag, Li, Na, K, Rb). *Synthetic Metals*, 42(1):1775–1780, 1991.

[22] R. Moret. Structural instabilities in molecular conductors: Silver and copper salts of dicyanoquinonediimine, (DCNQI)$_2$X (X= Ag or Cu). *Synthetic Metals*, 27(3):301–307, 1988.

[23] M. Schwoerer and H.C. Wolf. *Organic Molecular Solids*. WILEY-VCH, 2007. Translated from German by Prof. William D. Brewer, Freie Universität Berlin, Germany. Original Title: Organische Molekulare Festkörper— Einführung in die Physik von π-Systemen. 2005 WILEY-VCH Verlag GmbH & Co. KGaA, Weinheim.

[24] R. E. Thorne. Charge-density-wave conductors. *Physics Today*, 49(5):42–48, 1996.

[25] S. Tomić, D. Jérome, A. Aumüller, P. Erk, S. Hünig, and J. U. von Schutz. Pressure-temperature phase diagram of the organic conductor (DM-DCNQI)$_2$Cu. *Synthetic Metals*, 27(3):281–288, 1988.

[26] S. Tomić, D. Jérome, A. Aumüller, P. Erk, S. Hünig, and J. U. Von Schütz. Pressure-induced metal-to-insulator phase transitions in the organic conductor (2, 5 DM-DCNQI)$_2$cu. *EPL (Europhysics Letters)*, 5(6):553, 1988.

[27] T. Vuletić, M. Pinterić, M. Lončarić, S. Tomić, and J. U. von Schütz. Non-ohmic electrical transport in the Peierls-Mott state of deuterated copper-DCNQI systems. *Synthetic Metals*, 120(1-3):1001–1002, 2001.

[28] A. Kobayashi, R. Kato, H. Kobayashi, T. Mori, and H. Inokuchi. The organic π-electron metal system with interaction through mixed-valence metal cation: Electronic and structural properties of radical salts of dicyano-quinodiimine, (DMe-DCNQI)$_2$Cu and (MeCl-DCNQI)$_2$Cu. *Solid State Communications*, 64(1):45–51, 1987.

[29] M. Bässler, R. Fink, C. Heske, J. Müller, P. Väterlein, J. U. Von Schütz, and E. Umbach. NEXAFS investigations of highly-ordered ultrathin films of DMe-DCNQI on Ag (111). *Thin Solid Films*, 284:234–237, 1996.

[30] A. Kobayashi, T. Mori, H. Inokuchi, R. Kato, and H. Kobayashi. The organic π-electron metal system with interaction through mixed-valence metal cation: electronic and structural properties of highly conducting anion radical salts (2,5-R_1,R_2-DCNQI)$_2$Cu (DCNQI=N,N'-dicyanoquinonediimine; R_1,R_2=CH_3, CH_3O, CI, Br). *Synthetic Metals*, 27:B275–B280, 1988.

[31] Y. Nogami, T. Date, K. Oshima, and O. Arimoto. Single crystal x-ray study of pressure-induced metal-insulator transition in (DMeDCNQI)$_2$Cu. *Synthetic Metals*, 86:2073–2074, 1997.

[32] D. Schmeisser, K. Graf, W. Göpel, J. U. Von Schütz, P. Erk, and S. Hünig. The electronic structure of (2-X-5-M-DCNQI)$_2$Cu. *Chemical Physics Letters*, 148(5):423–428, 1988.

[33] I. H. Inoue, A. Kakizaki, A. Kobayashi, R. Kato, H. Kobayashi, H. Namatame, and A. Fujimori. Electronic structure of the organic conductor (DMe-DCNQI)$_2$Cu studied by photoemission spectroscopy. *Physica C: Superconductivity*, 185:2691–2692, 1991.

[34] D. Bauer, B. Maier, D. Schweitzer, and J. U. von Schütz. Thermopower of deuterated and alloyed Cu-DCNQI-crystals — evidences for a "quite normal reentry" of the conductivity. *Synthetic Metals*, 71:1887–1888, 1995.

[35] H. Hoshino, K. Iida, T. Kawamoto, and T. Mori. Structural and magnetic properties of Cu [C (CN)$_3$]$_2$ and Mn [C (CN)$_3$]$_2$. *Inorganic Chemistry*, 38(19):4229–4232, 1999.

[36] T. Mori, H. Inokuchi, A. Kobayashi, R. Kato, and H. Kobayashi. Electrical conductivity, thermoelectric power, and ESR of a new family of molecular conductors, dicyanoquinonediimine-metal [(DCNQI)$_2$ M] compounds. *Physical Review B*, 38(9):5913, 1988.

[37] J. U. von Schütz, M. Bair, H. J. Gross, U. Langohr, H.-P. Werner, H. C. Wolf, D. Schmeißer, K. Graf, W. Göpel, P. Erk, et al. The conducting salts of N, N'-dicyanoquinonediimine (DCNQI). *Synthetic Metals*, 27(3):249–256, 1988.

[38] J. U. von Schütz, D. Bauer, H. Wachtel, and H. C. Wolf. Transient/persistent switching of Cu-DCNQI by light and pressure. *Synthetic Metals*, 71(1):2089–2090, 1995.

[39] J. U. von Schütz, D. Gomez, H. Schmitt, and H. Wachtel. Conductivity without spin-signal, spin signal without conductivity-switchable radical ion salts of deuterated Cu (DCNQI)$_2$. *Synthetic Metals*, 86(1):2095–2096, 1997.

[40] H.-P. Werner, J. U. von Schütz, H. C. Wolf, R. Kremer, M. Gehrke, A. Aumüller, P. Erk, and S. Hünig. Radical anion salts of N, N'-dicyanoquinonediimine (DCNQI): Conductivity and magnetic properties. *Solid State Communications*, 65(8):809–813, 1988.

[41] N. W. Ashcroft and N. D. Mermin. *Solid State Physics*. Saunders College, Philadelphia, 1976.

[42] H. Kobayashi, A. Miyamoto, R. Kato, A. Kobayashi, Y. Nishio, K. Kajita, and W. Sasaki. Reentrant behavior in the pressure-temperature dependence of the resistivity of (DMeO-DCNQI)$_2$ Cu. *Solid State Communications*, 72(1):1–5, 1989.

[43] B. E. P. Beeston, R. W. Horne, and R. Markham. *Electron diffraction and optical diffraction techniques*. American Elsevier, 1973.

[44] A. H. Zewail. Femtochemistry: Atomic-scale dynamics of the chemical bond using ultrafast lasers (nobel lecture). *Angewandte Chemie International Edition*, 39(15):2586–2631, 2000.

[45] H. Enqvist. *A setup for efficient frequency tripling of high-power femtosecond laser pulses*. PhD thesis, Lund, 2004.

[46] N. Erasmus. The development of an electron gun for performing ultrafast electron diffraction experiments. Master's thesis, Stellenbosch University, 2009.

[47] D. R. Lide, editor. *CRC Handbook of Chemistry and Physics*. CRC Press, 2008.

[48] M. J. Berger, J. S. Coursey, M. A. Zucker, and J. Chang. NIST Standard reference database 124: Stopping-power and range tables for electrons. *Protons, and Helium Ions, National Institute of Standards and Technology, Physical Measurement Laboratory*, 2005.

[49] K. Flöttmann. A space charge tracking algorithm (ASTRA).

[50] K. A. Haupt. *Phase Transitions in Transition Metal Dichalcogenides studied by Femtosecond Electron Diffraction*. PhD thesis, Stellenbosch University, 2013.

[51] L. F. Drummy, J. Yang, and D. C. Martin. Low-voltage electron microscopy of polymer and organic molecular thin films. *Ultramicroscopy*, 99(4):247–256, 2004.

[52] K. Haupt, M. Eichberger, N. Erasmus, A. Rohwer, J. Demsar, K. Rossnagel, and H. Schwoerer. Ultrafast metamorphosis of a complex charge-density wave. *submitted*, (January 2014).

[53] N. Erasmus. *Ultrafast structural dynamics in 4H_b-$TaSe_2$ observed by femtosecond electron diffraction*. PhD thesis, Stellenosch University, 2013.

[54] T. R. Kuphaldt. Lessons in electric circuits, volume I–DC. *Design Science*, 2006.

[55] Maximilian Eichberger, Marina Krumova, Helmuth Berger, and Jure Demsar. Sample preparation methods for femtosecond electron diffraction experiments. *Ultramicroscopy*, 127:9–13, 2013.

[56] X. Z. Li. Simulations and analysis of electron diffraction (SAED2.0) program.

[57] D. R. Lide, editor. *CRC Handbook of Chemistry and Physics*. CRC Press, 77 edition, 1996.

[58] R. Burkert, H. W. Helberg, and J. U. von Schütz. Longitudinal and transverse conductivity in (2, 5-Me_2-DCNQI)$_2$Cu fibres. *Synthetic Metals*, 56(1):2519–2524, 1993.

[59] T. M. Yarwood and F. Castle. *Physical and mathematical tables*. Macmillan, 1970.

[60] S. Numata, S. Oohara, K. Fujisaki, J. Imaizumi, and N. Kinjo. Thermal expansion behavior of various aromatic polyimides. *Journal of Applied Polymer Science*, 31(1):101–110, 1986.

[61] J. F. O'Hanlon. *A user's guide to vacuum technology*. John Wiley & Sons, 2005.

[62] H. Bannwarth. *Gas Physics and Vacuum Technology*, pages 1–109. Wiley-VCH Verlag GmbH & Co. KGaA, 2005.

[63] R. Comes, S. M. Shapiro, G. Shirane, A. F. Garito, and A. J. Heeger. Neutron-scattering study of the 38-and 54-K phase transitions in deuterated tetrathiafulvalene-tetracyanoquinodimethane (TTF-TCNQ). *Physical Review Letters*, 35(22):1518, 1975.

APPENDIX A
Cooling d_6 Cu(DCNQI)$_2$ in the UED setup

As described in Chapter 2 our goal is to introduce the organic anion salts of d_6 and h_8/d_6 Cu(DCNQI)$_2$ into the UED setup described in Chapter 3 in order to eventually do transient ultrafast electron diffraction experiments on it and thus to investigate its structural dynamics during a light induced metal-insulator phase transition on ultrafast time scales. The first step towards this end goal is incorporating the sample into the system in such a way that its room temperature state can be observed, investigated and compared to simulated data. This was done successfully as described Chapter 4.

The next step in this process is to cool the sample below its metal to insulator phase transition to study the stationary diffraction images of the sample's insulating phase. The metal to insulating phase transition temperature during cooling is about 70 K for both, the pure d_6 sample as well as the (70:30)-h_8/d_6 alloy, see Table 2.2 [7]. Therefore the closed circuit helium cryostat was incorporated into the UED setup. As mentioned in Chapter 3 a sample mount was designed in order to thermally couple the sample to the cooling finger of the cryostat, while decoupling it from the rest of the chamber. The cryostat's second temperature sensor was fixed to the sample mount within $\sim$3 mm of the TEM mesh with the sample on it. The sample could therefore be cooled in a controlled manner to less than about 30 K. Ideally this makes all phase transitions for d_6 and h_8/d_6 during heating and cooling accessible – even the reentry into the metallic state (as summarised in Table 2.2).

Unfortunately a decrease in sharpness of the diffraction patterns is seen from 150 K downwards during cooling. As mentioned in Section 4.3 the signal-to-noise ratio of the images shows no set trend with change in temperature. However, the diffraction spots became less defined and more smeared out during cooling. The most probable explanation for this observation is the condensation of water on the sample: Water condenses at 173 K at pressures in the order of nanobar [62] (the vacuum chamber reaches $\sim 10^{-6}$ mbar = 1 nbar). Being thermally coupled to the cryostat, but decoupled from the rest of the chamber, the sample is the coldest area in the vacuum chamber. Therefore condensation is most likely to occur on the sample and not on other surfaces. This excludes that condensation would occur on the detector, which would also result in the diffraction patter being

observed to decrease in quality. While heating the sample again after cooling, the diffraction spots become more defined again, indicating that the condensate is the main reason for the deterioration of the observed diffraction pattern quality at low temperatures. After a cooling and heating cycle the diffraction pattern does not recover to its initial sharpness, however. As discussed in Section 4.5, microcracks probably form during the cooling process, because of the tension exerted on the crystal slice by the copper mesh. It is not clear, though, whether the condensate on the sample surface aggravates the sample degradation. The main problem caused by the condensation of water on the sample therefore is the loss of diffraction peak sharpness at low temperatures. Several techniques were thus employed in order to prevent condensate formation on the sample and consequently improve the observable diffraction patterns at low temperatures:

A heater (using electrical resistance) was attached to the sample mount. The idea was to keep the sample at a higher temperature than the rest of the chamber while cooling with the cryostat. In this manner the condensate would form on other surfaces inside the vacuum chamber except the sample: The sticking coefficient of water increases with decreasing surface temperature. E.g. in Reference [61] the residence time (τ) of a water molecule on a stainless steel surface at 22° C is given as $\tau_{22} = 9800$ s, while for 100° C $\tau_{100} = 16$ s. This demonstrates that water molecules reside (stick) longer to cold surfaces than to hotter ones. In order to decrease the probability of water molecules sticking to the sample, it was therefore kept warmer than the rest of the chamber. When reaching about 30 K at the cold finger of the cryostat the heater was switched off and the sample would cool down rapidly to the cryostat finger's temperature. Since the water condensed on other surfaces while the sample was still warm, fewer free water molecules were present to condense on the cold sample. This, however, caused sample damage due to the high cooling rate and no diffraction patterns were observed neither at low temperatures nor after heating the sample back to room temperature. At low temperatures is was therefore not certain whether the diffraction pattern disappeared due to condensation or sample degradation. Therefore heating and subsequent rapid cooling of the sample does not improve diffraction pattern quality. A cooling/heating rate of 1 K per minute was found to yield the best results in terms of sample preservation during the cooling and heating cycles hence also allowing samples to be investigated over several cycles.

A "cold trap" was mounted to the chamber: Liquid nitrogen is filled into an aluminium beaker with tubes at its bottom protruding into the vacuum chamber. In this way a metallic tube inside

the vacuum chamber is cooled to around 80 K before the cryostat is switched on. Again the idea is to attract water molecules to a cold surface away from the sample and utilise the higher sticking coefficient of water on colder surfaces to prevent condensation on the sample. After about an hour of cooling the cold trap the cryostat is switched on. The effect of condensate formation on the sample at low temperatures (<80 K) was slowed down with the implementation of the cold trap. After 1 h – 2 h below 80 K, however, the diffraction peaks became blurry.

Another approach to protect the sample from condensation was shielding it. A U-shaped copper plate was mounted upside down to a perspex rod. This was fixed in such a way that the sample could be moved into the shield during cooling and during intervals when no diffraction images were taken. The idea is to shield the sample from molecules travelling in ballistic motion. Minimising the possible angles of approach for molecules towards the sample surface would decrease the number of molecules landing on the sample. We have observed that diffraction patterns at low temperatures remain sharp for longer times – in the order of hours rather than minutes.

The vacuum chamber has also been baked out at temperatures of about 110° C over several weeks. According to O'Hanlon [61] this procedure decreases the amount of adsorbed molecules on chamber surfaces. However neither the pressure nor the low temperature diffraction images improved significantly after the bake-out.

Condensate formation on the samples was thus decreased or slowed down hence improving diffraction patterns observed at low temperatures by the following methods: a cold trap attracting water molecules on a surface away from the sample, and a sample shield minimising the angles of approach for free water molecules to reach the sample. A cooling rate of 1 K/minute was found to preserve samples for several cooling-heating cycles. As discussed in Section 4.6 performing experiments at vacuum pressures in the order of picobar (instead of nanobar) will decrease the problem of condensation: Firstly there are less gas molecules at lower pressure. And secondly decreasing the pressure by three orders of magnitude decreases the boiling point of water by 20 K. Therefore the experiments at lower temperatures can be performed without condensate forming on the sample.

APPENDIX B
Experiments on other molecular organic crystals

As an alternative to the copper salt of DCNQI, **Li(DCNQI)$_2$** was investigated. The samples were grown and prepared in a similar way as described in Chapter 3 for Cu(DCNQI)$_2$ [13] at the University of Würzburg. The lithium salt has the same space group as the copper salt [15], but its phase transition behaviour differs: At T_{MI} ∼130 K it undergoes a doubling of the unit cell and at T_{MI} ∼70 K four-fold CDW formation was observed in infrared spectroscopy experiments [21]. Choosing a sample with a phase transition temperature of 130 K – which is about 60 K higher than for the partially deuterated copper salt – was done for the same reasons as outlined for the MeBr copper salt (see Section 4.7): Enabling cooling below the expected structural change boundary before condensation on the sample would accumulate, and giving a wider temperature range below the phase transition to cool down to overcome possible lowering of T_{MI} due to tension.

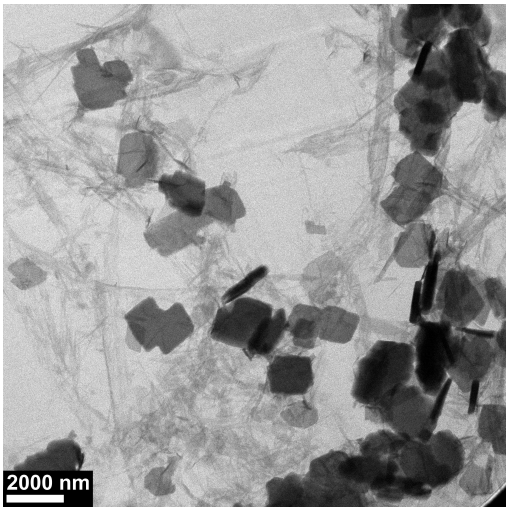

Figure B.1: TEM high magnification image of a crystal of Li(DCNQI)$_2$.

Unfortunately the lithium salt proved to very difficult to prepare with the ultramicrotome. The needles were thinner (∼ 40 nm, i.e. half as thick as crystals of the copper salt) and a lot more brittle than Cu(DCNQI)$_2$. Due to this, ultramicrotoming was unsuccessful so far. During the cutting procedure the sample was grated rather than cleaved. A powder was produced, sinking to the

bottom of the knife's water boat, rather than slices floating on the water surface. The samples that were collected were thus extremely small (∼2 μm) and looked non-uniform under the TEM and light microscope. Figure B.1 shows a high magnification image of the Li(DCNQI)$_2$ salt taken at the TEM. Lighter fragments were identified as resin from the ultramicrotoming process. Darker parts are pieces of the lithium salt which look non-uniform in thickness.

A fully organic molecular salt, **TTF-TCNQ**, was also investigated. The crystals were synthesised at the University of Würzburg. They were ultramicrotomed and prepared similar to the Cu(DCNQI)$_2$ salts. Samples were analysed at the TEM and subsequently introduced into the UED setup. This sample has a dimerising phase transition (T_{MI} ∼54 K) and a tetramerising phase transition (T_{MI} ∼38 K) [63]. The fully organic material is less brittle and is thus easier to ultramicrotome than either the copper or the lithium salts. On average bigger crystal slices – ∼200 μm in diameter, as seen in Figure B.2 – were collected on the TEM meshes and stayed intact during drying. Therefore a bigger area – about four times the size of the copper crystal slices which were in the order of 100 μm in diameter – would contribute to the diffraction signal. Since TTF-TCNQ is a fully organic molecule, constituted of C, N, and H atoms, with no additional larger metal ions. The intensity of the diffraction spots of the scattered electrons depends on the structure amplitude of the scattering atom. This structure amplitude in turn, increases as a function of the atomic number of the atom. Therefore less intense electron diffraction peaks are expected from materials made up of lighter atoms. [12] (see Section 2.2). Under the light microscope the samples looks smooth and single crystalline (as seen in Figure B.2).

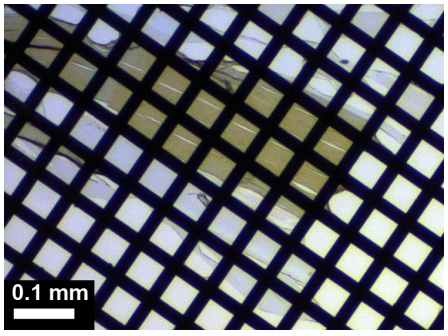

Figure B.2: TTF-TCNQ sample (∼50 nm thick) on a TEM mesh after ultramicrotoming. This image was taken under a conventional light microscope. The uniform colouration of the crystal indicates the single crystallinity of the sample.

However, smeared out diffraction spots were observed in the UED setup (Figure B.3). A possible explanation for this observation is that the thin sample's surface is not flat, but might be wavy. Due to the large area the electron beam diffracts off, smeared out diffraction peaks occur, averaging over an angular spread of directions due to the wavy surface. Therefore no analysis on the room temperature diffraction patterns could be done. Low temperature phase transition data could neither be collected.

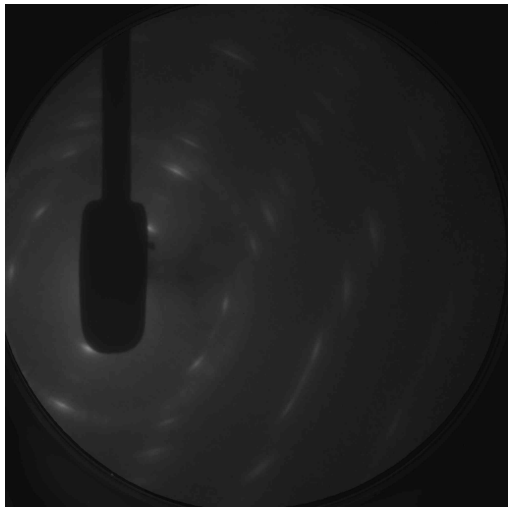

Figure B.3: Room temperature diffraction image of a TTF-TCNQ crystal taken in the UED setup. The poorly defined, smeared out diffraction spots may indicate a wavy surface, causing diffraction off different angles of the molecular structure.